



Libraries and Learning Services

University of Auckland Research Repository, ResearchSpace

Copyright Statement

The digital copy of this thesis is protected by the Copyright Act 1994 (New Zealand).

This thesis may be consulted by you, provided you comply with the provisions of the Act and the following conditions of use:

- Any use you make of these documents or images must be for research or private study purposes only, and you may not make them available to any other person.
- Authors control the copyright of their thesis. You will recognize the author's right to be identified as the author of this thesis, and due acknowledgement will be made to the author where appropriate.
- You will obtain the author's permission before publishing any material from their thesis.

General copyright and disclaimer

In addition to the above conditions, authors give their consent for the digital copy of their work to be used subject to the conditions specified on the [Library Thesis Consent Form](#) and [Deposit Licence](#).

VIBROACOUSTIC ANALYSIS OF PANELS USING A WAVE AND FINITE ELEMENT METHOD

Yi Yang

*A thesis submitted in fulfillment of the requirements for the degree
of Doctor of Philosophy in Mechanical Engineering, The
University of Auckland, 2018.*

Abstract

This thesis concerns extending a wave and finite element (WFE) method to predict the vibroacoustic characteristics of structures, including wave propagation characteristics, sound transmission loss and sound radiation, of flat infinite and finite panels and infinite cylinders.

In this method, a coupled fluid/structure system is considered. A segment of the structure is modelled using a conventional finite element (FE) method. The fluid spaces are modelled analytically. The fluid pressures on the surfaces of the segment exert external nodal forces on the FE model of the structure. Periodicity theory and equilibrium conditions are then used to postprocess the mass and stiffness matrices of the periodic cell together with the nodal forces. The spectral dynamic stiffnesses of the fluids and structure are developed and assembled into the total spectral dynamic stiffness matrix of the coupled system. This is then used to calculate the structural response to excitation. The excitations can be acoustic pressures or general structural excitation. Once the structural displacements are found, the acoustic pressures can be calculated analytically. The WFE method is also used to develop homogenised models of honeycomb cored panels, with the model size being reduced by Guyan reduction.

This method is applied to infinite panels, finite panels and cylindrical shells. For simple structures analytical methods are available. The WFE predictions show excellent agreement with analytical solutions. For complicated structures (e.g., laminated panels, honeycomb-cored panels, and composite cylindrical shells), analytical solutions are difficult. Due to the use of the FE method, the geometry of arbitrarily complex structures can be captured straightforwardly. The full power of commercial FE packages and element libraries can be utilised. It is straightforward and efficient to use the WFE method, which provides accurate predictions at low computational cost.

Acknowledgement

I would like to appreciate Prof. B. R. Mace for guiding me patiently and rigorously throughout this thesis. His positive attitude and encouraging suggestions make me enchanted in each stage of my research. It is a great pleasure to work with him.

I would like to express my appreciations to Dr M. J. Kingan for providing all the possible assistances during the thesis.

I wish to thank Dr Neil Ferguson for many interesting and useful discussions during the visiting research at ISVR.

Also, I want to thank those who helped me overcome various difficulties involved in this period of overseas study.

I would like to express my gratitude to China Scholarship Council (CSC) for financial support.

Finally, I would like to present a unique thanksgiving for my parents who made lots of support, care, and sacrifices for me.

Table of Contents

Abstract	i
Acknowledgement	ii
Table of Contents	iii
1. Introduction	1
1.1 Introduction	1
1.1.1 Background.....	1
1.1.2 Motivation for this Research.....	3
1.2 Literature Review	7
1.2.1 Analytical Methods.....	7
1.2.2 Numerical Methods.....	15
1.3 Wave and Finite Element Method	17
1.4 Outline of the Thesis	21
1.5 Contributions of this Thesis	24
2. Sound Transmission through, and Radiation from Infinite Panels	26
2.1 Introduction	26
2.2 Theory and Formulation	27
2.2.1 Fluid Space.....	28
2.2.2 Solid Structure.....	30
2.2.3 Fluid-Structure Interaction.....	31
2.2.4 Acoustic/Force Excitation.....	33
2.2.5 Spectral Dynamic Stiffness Matrix and Response.....	35
2.2.6 Sound Transmission Loss and Diffuse Incident Field.....	37
2.2.7 Sound Radiation.....	38
2.3 Illustrative Examples	40

2.3.1 One-Dimensional Isotropic Panel	40
2.3.2 Two-Dimensional Isotropic Panel	41
2.4 Application Examples.....	42
2.4.1 Symmetric Sandwich Panel with Orthotropic Core.....	42
2.4.2 Anti-Symmetric Sandwich Panel with Isotropic Core.....	43
2.5 Conclusions.....	45
Figures.....	47
3. Sound Transmission through Multi-layer Finite Panels	55
3.1 Introduction.....	55
3.2 Theory and Formulation	57
3.2.1 Fluid-Structure Interaction.....	57
3.2.2 Spectral Dynamic Stiffness Matrices of the Fluid Layers	58
3.2.3 Spectral Dynamic Stiffness Matrices of the Solid Layers	59
3.2.4 Assembly of the Spectral Dynamic Stiffness Matrices.....	61
3.2.5 Sound Transmission Loss and Diffuse Incident Field	64
3.2.6 Windowing for Finite Size Panels	64
3.2.7 Summary	66
3.3 Illustrative Examples	66
3.3.1 Single Layer Panel	66
3.3.2 Three Layer Isotropic Panels	67
3.4 Application Examples.....	69
3.4.1 Three Layer Orthotropic Panel	69
3.4.2 Complicated Multi-layered Panel	70
3.5 Conclusions.....	71
Figures.....	73

4. Sound Transmission through Composite Honeycomb Panels	79
4.1 Introduction.....	79
4.2 Theory and Formulation	81
4.2.1 Fluid-Structure Interaction.....	82
4.2.2 FE Model of a Periodic Cell	82
4.2.3 Reduction of the FE Model.....	84
4.2.4 Acoustic Excitation.....	87
4.2.5 The WFE Model and Sound Transmission.....	88
4.2.6 Modal Density and Group Velocity.....	89
4.3 Numerical Examples.....	90
4.3.1 Honeycomb Panels with Hexagonal Core and Isotropic Skins	91
4.3.2 Honeycomb Panels with Composite Faces and Square Core	95
4.4 Conclusions.....	96
Figures.....	98
5. Sound Transmission through Two Dimensional Cylindrical Shells	110
5.1 Introduction.....	110
5.2 Theory and Formulation	111
5.2.1 Fluid Spaces	112
5.2.2 Fluid-Structure Interaction.....	114
5.2.3 Analytical Model and Responses.....	118
5.2.4 The WFE Model and Responses.....	120
5.3 Illustrative examples.....	124
5.4 Conclusions.....	124
Figures.....	126
6. Sound Transmission through Three Dimensional Cylindrical Shells.....	128

6.1 Introduction.....	128
6.2 Theory and Formulation	129
6.2.1 Fluid Spaces	130
6.2.2 Solid Structure	133
6.2.3 Fluid-Structural Interaction.....	137
6.2.4 Spectral Dynamic Stiffness Matrix and Responses	138
6.2.5 Acoustic Potential Energy.....	139
6.3 Illustrative Examples	139
6.3.1 Spherical Wave Interacting with a Cylindrical Shell.....	140
6.3.2 Sound Radiation from a Pipe Excited by a Point Force.....	141
6.3.3 Sound Transmission through an Orthotropic Cylinder.....	143
6.4 Application Examples.....	144
6.4.1 Laminated Sandwich Cylinder.....	144
6.4.2 Orthotropic Cylinder.....	145
6.5 Conclusions.....	146
Figures.....	147
Concluding Remarks	155
7.1 Summary of Present Work	155
7.2 Conclusions.....	158
7.3 Suggestions for Further Work	158
Publication List	160
References.....	161

Chapter 1

INTRODUCTION

This thesis concerns the prediction of the noise and vibration behaviour, especially sound transmission and radiation, in plane and cylindrical structures using a wave and finite element (WFE) method. In this chapter the subject is introduced, relevant literature and the WFE method reviewed and the rest of the thesis overviewed.

1.1 Introduction

In this section, the background of this research is introduced. Then, the research motivation follows.

1.1.1 Background

The vibration and noise produced by mechanical devices influence not only their performance but also the comfort of customers. For example, automobiles, ships and aircraft are subjected to various dynamic loadings. The structural members of these products are often made from materials and constructions which are stiff yet low mass. Examples include laminated structures (commonly used in automobiles), honeycomb-cored structures with carbon fibre reinforced laminate face sheets (commonly used in aircraft) and corrugated core structures (used in the floor of a train). Such structures typically have excellent mechanical performance (e.g., safety, durability, high stiffness). However, the low density makes these components

suffer from poor noise and vibration performance during operation. When the fatigue limits of structures are reached, the repeated stresses can cause their failures (e.g., a crack is formed), and hence reduce the life of these products. Also, due to the low mass, lightweight components can radiate noise efficiently. A noisy environment reduces comfort for passengers. Hence, effective measures should be made to control noise pollution. Noise control, for example, is often made by adding mass, but that has a negative effect (e.g., increasing energy consumption). More approaches can be found in reference [1].

Another example is the construction of lightweight buildings due to the disadvantages of conventional buildings (e.g., having thick walls and heavy floors, made from unrecyclable materials such as bricks and plaster). Many lightweight building systems are made from individual, prefabricated and lightweight structural components (e.g., laminates, carbon fiber reinforced polymer (CFRP), etc.). There is widespread use of such components. An example of a such a laminate is cross-laminated timber (CLT) which is made from gluing layers of lumber beams together, with the layers oriented such that the beams are perpendicular to those in the adjacent layer. This configuration provides high stiffness in more than one direction. The advantages (e.g., design flexibility, eco-friendly, thermal insulation) of CLT make it very popular in building constructions (e.g., walls, roofs and ceilings) but its noise performance is poorly understood. The limited use of materials contributes to the reductions of emission and building waste. Some structural components (e.g., steel, plaster and glass wool) are fully recyclable, not to mention their ease of assembly and the flexibility for repair. However, lightweight structures are prone to poor acoustic performance. For example, reference [2] shows that a composite honeycomb-cored panel has a lower sound reduction index than that of a solid panel having the same mass per unit area.

Therefore, for safety and meeting the increasing demands for comfort, it is valuable to develop mathematical models that can accurately predict the transmission of noise and vibrations.

1.1.2 Motivation for this Research

In this section, the classic theories for representing the dynamics of structures such as flat panels and cylindrical shells are briefly introduced. They can be readily used for predicting the vibration and acoustic level of simple structures. However, for complex structures, it is difficult to develop analytical models for predicting the vibroacoustics characteristics. It will be demonstrated throughout this thesis that the WFE method is an attractive alternative being simple to implement, computationally efficient and applicable to even very complex structures.

The classic theories are primarily based on the stress-strain relationships of the solid material under consideration. For a simple beam, for example, Euler-Bernoulli theory can be used. The beam's equation of motion can be derived using the principle of virtual work which involves calculating kinetic energy per unit volume, and potential energy per unit volume due to internal forces and the virtual work of external forces. Note that the cross-sections of Euler-Bernoulli beams are assumed to be perpendicular to the neutral axis, and internal shear forces are neglected.

The Kirchhoff-Love plate [3, 4] is an example of a flat panel. The equations governing the motion of the Kirchhoff-Love plate are an extended form of the Euler-Bernoulli beam theory using similar assumptions e.g., the plate thickness remains constant during its deformation, infinitesimal strains and rotations, the straight lines perpendicular to the mid-surface remains straight and perpendicular to the mid-surface, shear deformation and rotary inertia are neglected. The three-dimensional elasticity is consequently reduced to a two-dimensional plate model.

As an extension to Kirchhoff-Love theory, Mindlin and Maxwell developed the Mindlin-Reissner theory [5] for isotropic, homogenous, thick plates. The transverse shear strains through the thickness are modelled using first-order shear theory (constant shear stress). After deformation, the straight line normal to the mid-surface of the structure is not necessarily perpendicular to the mid-surface. A shear correction factor is introduced to account for the effect of the parabolic variation of the shear stresses across the thickness. Again, the plane-stress assumption is made, and the principle of the virtual work used to establish the equations of motion.

The classic theories for thin circular shells are represented using eighth-order partial differential equations which have various forms depending on assumptions underpinning them. Leissa [6] gives a review of many such models. For a thin, homogeneous, isotropic shell, for example, the Kirchhoff-Love shell theory may be used, but note that this model neglects the effects of the transverse shear stresses and rotational inertia. An accurate model is a modified Donnell-Mushtari shell theory (e.g., Flugge-Byrne-Lurye theory), which can include the effects of membrane and transverse shear stresses, inertia and bending. For laminated structures, a combination of Mindlin-Reissner theory and Flugge-Byrne-Lurye theory can be used for establishing the equations of motion, where a plane-stress assumption is made for each layer. Note that the internal stress normal to the mid-surface is neglected. The derivation of these equations of motion involves lengthy algebraic calculations and various assumptions.

For more complicated structures (e.g., laminates, CFRP, honeycomb-cored panels, corrugated core panel, stiffened panels), it is difficult or even impossible to develop partial differential equations for estimating their vibroacoustic performance. Therefore, numerical methods become valuable. The finite element (FE) method is a commonly used numerical method. The entire structure is discretised using finite elements. However, the model size can be very large at high frequencies due to the fine discretisation required to model the structural

waves with small wavelengths which propagate at these frequencies. Thirdly, a statistical energy analysis (SEA) method may be used for predicting the average response at high frequencies, which requires the calculation of modal densities, group velocities, and coupling loss factors.

An alternative method is the wave and finite element (WFE) method. This method is a wave-based approach which describes the vibrations in terms of wave propagation through a structure. Using this method, only a small segment of a continuous structure is modelled. The structure is assumed to be homogenous or piecewise-homogenous in the directions of wave propagation, but the properties of the cross-sections can vary in an arbitrary manner. A conventional FE method (typically using a commercial FE package) is used to model the segment. Assuming spatial and time-harmonic motion, the mass and stiffness matrices of the segment are postprocessed using periodicity conditions to form the eigenproblems whose solutions yield the dispersion relationships. The characteristics of wave propagation can be found, e.g. wavenumber, group velocity, etc. This method can overcome the difficulties of solving analytical equations (e.g., transcendental or high-order dispersion equations) for predicting the characteristics of wave propagation. Besides, the full power of existing FE packages and their extensive element libraries can be used. The model size is small and does not increase with frequency.

Due to these advantages, the present work is dedicated to extending the WFE method to predict the vibroacoustic response of fluid/structure coupled systems. In particular, an infinite structure is modelled using a WFE method. Only a small segment of the structure is needed to be modelled using a conventional FE method. The fluid spaces are modelled analytically. During the FE discretisation, the pressures caused by the fluid surrounding the structure are modelled as equivalent nodal forces. By postprocessing the mass and stiffness matrices of the segment together with the nodal forces using periodicity and equilibrium conditions, the

structural dynamic stiffness matrix is coupled to the spectral dynamic stiffnesses of the fluids to form a total spectral dynamic stiffness matrix. Once the displacement responses are found, the acoustic pressures can be calculated analytically. The analysis of wave propagation and forced response using the WFE method is well-established. This thesis extends the method to include sound-structure interaction.

The original contributions presented in this thesis include the extension and validation of the WFE method for vibroacoustics problems and the application of the method to predicting sound transmission through, and radiation from, complicated structures (e.g., various infinite and finite laminated panels, circular shells with various configurations).

First, simple structures are considered, including an infinite Euler-Bernoulli beam, an infinite isotropic, homogeneous thin plate, an infinite homogeneous and an isotropic cylindrical shell. For these structures, analytical methods are readily obtained [7]. The WFE predictions are compared with those of the analytical methods. The excellent agreement between the predictions illustrates the validity of the extended WFE method. Then, this method is applied to complicated structures, for example, sound transmission through laminated panels, and honeycomb-cored panels. The effect of the finite size of the structure is taken into account using a spatial windowing approach. The characteristics of wave propagation in these structures are also predicted and used to illustrate the structural-fluid interactions (e.g., to explain observed coincidence effects in a sound transmission loss spectrum). The sound transmission loss characteristics of cylindrical structures with the laminated shell are investigated as well. The cylindrical structure can have fluids or a vacuum at the exterior or interior to the structure. Examples considered are relevant to sound transmission through an aeroplane fuselage and noise radiation from internal sources within pipes.

In the next section, the analytical and numerical methods are reviewed in detail. Section 1.3 contains a review of the WFE method. The main contents and original contributions of this thesis are described in section 1.4 and section 1.5 respectively.

1.2 Literature Review

In this section, current techniques for analysing the vibroacoustic characteristics of structures are reviewed, including analytical methods, numerical methods and wave and the finite element method.

1.2.1 Analytical Methods

Sound transmission through an infinite Euler-Bernoulli beam was studied using analytical methods in reference [8]. The characteristics of sound transmission through simple panels was investigated in chapter 5 of reference [7]. The sound radiation from submerged plates was investigated in chapter 8 of reference [9]. The structures were modelled using classic theories (e.g., Mindlin-Reissner theory) while the fluid spaces were modelled using the acoustic wave equation (see chapter 5 in reference [10] and chapter 1 of reference [11]). The acoustic performance of laminated panels was studied early by Kurtze and Watters [12] using an electrical circuit analogy. Their research found that the laminate structure could have better sound insulation performance than that of a single solid panel with the same mass per unit area due to low shear stiffness and high bending stiffness by using a soft core. The antisymmetric mode of vibration may lead to high sound transmission due to coincidence. However, the core considered in their model was assumed to be incompressible such that only the effect of the antisymmetric wave mode on sound transmission was studied. Ford *et al.* [13] analytically predicted the vibroacoustic characteristics of a laminate panel by considering a compressible core using the Rayleigh-Ritz minimum energy principle. Note that the rotational kinetic energy was neglected in the analytical model. The dilatational symmetric mode of vibration was found to be another vibration mode responsible for causing poor acoustic performance. The

dilatational resonance frequency mainly depends on the core shear stiffness and the mass of the skins.

Moore et al. [14, 15] developed an analytical model for predicting sound transmission through laminate panels with isotropic cores and orthotropic cores, modelling the structural displacements as a combination of a symmetric (dilatational) wave mode and an antisymmetric flexural wave mode. The through-thickness shear deformation was assumed to be linear. Their research showed that a proper configuration of the core shear stiffness could shift the thickness resonance to low frequencies while the coincidence frequency could be tuned to high frequencies. Note that the analytical model was developed using a Lagrange's method, which involves the calculation of the kinetic and potential energies based on the structural stress-strain relationship. For linear materials, it can be expressed as

$$\boldsymbol{\varepsilon} = \mathbf{C}\boldsymbol{\sigma} \quad (1.1)$$

where $\boldsymbol{\varepsilon}$ is a strain vector, $\boldsymbol{\sigma}$ a stress vector and \mathbf{C} is the compliance matrix. The strain and stress vectors can be expressed as

$$\begin{aligned} \boldsymbol{\varepsilon} &= \left[\varepsilon_x \quad \varepsilon_y \quad \varepsilon_z \quad \varepsilon_{xy} \quad \varepsilon_{yz} \quad \varepsilon_{xz} \right]^T, \\ \boldsymbol{\sigma} &= \left[\sigma_x \quad \sigma_y \quad \sigma_z \quad \sigma_{xy} \quad \sigma_{yz} \quad \sigma_{xz} \right]^T \end{aligned} \quad (1.2)$$

whilst the compliance matrix has components

$$\mathbf{C} = \begin{bmatrix} 1/E_x & -\nu_{xy}/E_x & -\nu_{xz}/E_x & 0 & 0 & 0 \\ -\nu_{yx}/E_y & 1/E_y & -\nu_{yz}/E_y & 0 & 0 & 0 \\ -\nu_{zx}/E_z & -\nu_{zy}/E_z & 1/E_z & 0 & 0 & 0 \\ 0 & 0 & 0 & 1/G_{xy} & 0 & 0 \\ 0 & 0 & 0 & 0 & 1/G_{yz} & 0 \\ 0 & 0 & 0 & 0 & 0 & 1/G_{xz} \end{bmatrix}, \quad (1.3)$$

where “T” denotes the transpose and E_x, E_y, E_z are Young’s moduli in the x, y and z directions respectively. The shear moduli in the x - y, y - $z,$ and x - z planes are G_{xy}, G_{yz}, G_{xz} , respectively. The corresponding Poisson’s ratios are denoted by $\nu_{xy}, \nu_{yz}, \nu_{xz}$.

Dym and Lang [16] investigated the influence of structural loss factors on the sound transmission loss of asymmetric laminate panels. Again Lagrange’s method was used for establishing the equation of motion. Their research showed that, compared to the damping of the skins, damping of the core has larger influences on the sound transmission loss (STL) at high frequencies. The core, having lower shear and compressional stiffnesses, performs better in reducing the sound transmission [17]. Makris *et al.* [18] proposed an optimisation method for redesigning the core of a laminate panel for increasing the sound transmission loss. Smolenski and Krokosky [19] studied the influence of the physical properties of the core on the dilatational mode of vibration of laminate panels. Compared to antisymmetric vibration, the dilatational wave mode was more sensitive to the core’s compression stiffness and thickness. Thamburajand and Sun [20] considered the optimisation of sound transmission through laminated beams with anisotropic materials, where both the material and geometrical parameters were used as design variables. Their research found that a laminated structure with anisotropic materials has better sound insulation performance compared to that of isotropic materials.

Bolton *et al.* [21] made a theoretical and experimental study of the sound transmission through double panels lined with elastic porous media. Partial differential equations of motion were developed for studying wave propagation through structures using porous material theory. Kim and Bolton [2] developed an analytical model for predicting the sound transmission through honeycomb-cored panels, modelling the structure using a transversely isotropic model. The honeycomb core was homogenised into a solid layer with nine equivalent stiffness

constants. The Young's moduli were determined using measurements while the shear moduli were calculated approximately using the analytical equations presented in reference [22]. Note that the transversely isotropic model involves reducing the stress-strain relationships of equation (1.1) by setting $E_x = E_y, \nu_{yz} = \nu_{xz}$ and $G_{yz} = G_{xz}$.

Some researchers used homogenised models to model the dynamics of honeycomb-cored panels. In reference [23], for example, Clarkson and Ranky developed an isotropic solid plate model for estimating the modal density, where the bending stiffness of the skins was assumed to be negligible. Renji et al. [24] modelled composite honeycomb-cored panels as orthotropic solid plates which were used for calculating the modal density and group velocity. The material parameters of these models were estimated using equations in chapter 1 of reference [25]. Nilsson and Nilsson [26] developed a fourth-order differential equation of motion for a symmetric, laminated beam using Hamilton's principle. The dispersion characteristics of wave propagation were investigated using the analytical model. Zergoune et al. [27] introduced frequency-dependent bending stiffnesses into the analytical model developed by Renji et al. [24] for predicting sound transmission through honeycomb-cored panels. All these studies model the honeycomb-cored panel as an equivalent solid panel using various assumptions and approximations. Based on the differential equations, Tie et al. [28] developed FE models of the periodic cells for predicting the characteristics of wave propagation through honeycomb-cored panels.

There can be a large number of elements used in FE modelling for accounting for the complexity of a periodic cell. For reducing the model size, the Craig-Bampton method [29] has been widely used for condensing the internal DOFs (e.g., references [30, 31]). A static condensation was proposed by Guyan [32] to reduce the size of large systems. Chen et al. [33] used a truncated Taylor series expansion for improving the accuracy of Guyan reduction. Downs [34] proposed qualitative guidelines for the selection of master DOFs, e.g. the

translational DOFs must be prioritised for retention in comparison to rotational DOFs. An analytical method was described in reference [35] for the proper selection of master DOFs. A linearised dynamic condensation was proposed by Bouhaddi and Fillod [36] to reduce the errors of Guyan reduction. For optimising the selection of some internal DOFs as master DOFs, a numerical method was proposed in reference [37].

Periodic structures have attracted much attention due to the existence of wave propagation and attenuation bands [38]. In the latter, the vibration level of the structure can be substantially reduced. A large amount of research has been undertaken investigating free and forced wave propagation in continuous periodic structures. Phani *et al.* [39], for example, studied the characteristics of wave propagation in various two-dimensional periodic lattices. Mead [40] categorised common methods for analysing such structures into several types including the receptance method, the transfer matrix method, the space-harmonic method, and the energy method.

In references [41, 42], the receptance method was proposed for studying the relationships between the bounding frequencies of wave propagation bands and the natural frequencies of a periodic cell. Mead [43] derived the kinetic and potential energy expressions for propagating waves in one-dimensional periodic systems with multiple couplings. The loss factors of damped waves were found using the energy method. The forced response of one-dimensional multi-coupled periodic structures was studied in reference [44] using a wave basis found from the eigenvectors.

The space-harmonic method is widely used for estimating sound transmission through, and radiation from periodic structures. In this method, the structural response to a convected harmonic pressure is assumed to be composed of a sum of harmonic components. For example, the characteristics of wave propagation in an infinite, periodically supported beam were studied by Mead [45], who showed that the structural wave motion consists of a sum of space

harmonics with different wavelengths, phase velocities and directions of propagation. It was shown that a forced wave with subsonic velocity can excite structural bending waves with supersonic velocities which can radiate sound efficiently [45]. The forced response of a simply supported beam subjected to convected random loading was studied using this method [46]. Mead [47] used the energy method for predicting the characteristics of free waves propagating through two-dimensional periodic panels. Mead [48] studied the sound radiation from a plate stiffened in one direction or two orthogonal directions, where the effect of fluid loading was neglected. The natural frequencies of finite periodic panels could be found from the free wave analysis. All of these are based on the assumption of space-harmonics. This assumption was proved later by Mace [49] using Fourier transforms. In reference [50], Mace also used this method for the forced response of periodically stiffened plates to a convected harmonic pressure. An explicit expression was derived for the structural displacement response without considering the effect of fluid loading. Mace [51] proposed a numerical integration method for accounting for the fluid loading.

Legault and Atalla [52] used the space-harmonic approach for studying the sound transmission through lightweight double panels with structural links, modelling the connectors as beams and spring-masses respectively. In reference [53], sound transmission through a double panel stiffened by a periodic array of studs was studied, where the studs were modelled as uniform springs. Lee and Kim [54] combined the space-harmonic method and the virtual energy method for calculating the sound transmission through one-dimensional periodically stiffened panels. Xin and Lu [55] applied the space-harmonic method and the virtual work principle to predicting the sound transmission through rib-stiffened panels.

Recently, an acoustic metamaterial based periodic structure was studied by Yong *et al.* [56-58] who introduced resonant microstructures (spring-mass resonators) into a host structure

for widening the wave attenuation band. Zouari *et al.* [59] proposed a method for detecting the band of propagating waves of a finite, thin plate with a periodic array of mass-screw resonators.

Shells may be viewed as a generalisation of flat plates. The three-dimensional geometry of a cylindrical shell can be reduced to the motion of the mid-surface for vibroacoustic analysis. There are various theories (e.g. Love's theory, Donnell's theory and Mushtari's theory [6]) depending on what assumptions are appropriate for modelling the structure of interest. The dynamics of composite shells are detailed in reference [60], where the plane-stress assumption was made for each layer. Smith [61], for example, modelled sound transmission through a thin cylindrical shell. Koval [62, 63] extended the work of Smith [61] and analysed the sound transmission through a laminated composite cylindrical shell using a shell theory presented by Bert *et al.* [64]. Various assumptions (e.g. plane stress) and approximations (e.g. the rotational inertia was neglected) were made for the analytical model. Blaise and Lesueur [65] established an analytical model for sound transmission through two-dimensional orthotropic composite shells using Hamilton's principle. Again, the plane-stress assumption was made. The effects of various layers were represented in terms of the first layer using the continuity conditions of plane stresses and displacements. In reference [66], they extended the expression to calculating the diffuse-field sound transmission loss.

Later, they considered three-dimensional orthotropic shells [67, 68]. Based on the stress-strain relationship, they used Hamilton's principle to establish the equations of motion for layers with force excitations. The bending, membrane, shear, longitudinal and rotational inertia effects were all considered. The dynamic stiffness matrices of layers were assembled using the stress (normal stress and shear stress) and displacement continuities. Lee and Kim [54, 69] used Love's theory to establish the analytical models for predicting sound transmission through a thin, cylindrical shell, and a double-walled cylindrical shell. Ghinet *et al.* [17, 70, 71] combined Midilin's plane stress theory with Flugge's theory to predict the sound transmission loss

characteristics of laminated shells. The modelling of the transverse shear forces through the thickness was improved using a shear correction factor [72]. Note that FE models use the energy-based transverse shear stresses [73, 74]. These references all assume that the fluid inside the cavity of the cylindrical shell is non-resonant. Fuller [75] predicted the sound radiation from an infinitely long cylindrical shell excited by a monopole source using a Fourier transform method. The internal resonance effect in the cylindrical cavity was modelled. The acoustic field generated by an open rotor was studied analytically in reference [76].

An alternative approach is a transfer matrix method (TMM). It is used by some authors [77-80] for predicting the sound transmission through laminated panels. Using this method, a wave solution is assumed for solving the partial differential equations for finding the relationships between the state variables (strain, stress) on any two consecutive interfaces of a layered structure. For example, for a single layer lying in the x - y plane, the state variables may be related by

$$\begin{Bmatrix} \sigma_{z,1} \\ \tau_{xz,1} \\ v_{x,1} \\ v_{z,1} \end{Bmatrix} = \mathbf{T} \begin{Bmatrix} \sigma_{z,2} \\ \tau_{xz,2} \\ v_{x,2} \\ v_{z,2} \end{Bmatrix}, \quad (1.4)$$

where “ \mathbf{T} ” is the transfer matrix, subscripts “1”, “2” denote the top and bottom surfaces respectively, the velocity components are represented by $v_{x,1}, v_{x,2}, v_{z,1}, v_{z,2}$, and stress components are $\sigma_{z,1}, \sigma_{z,2}, \tau_{xz,1}, \tau_{xz,2}$. The total transfer matrix of the system can be found by assembling those of individual layers using continuity of velocities and equilibrium of stresses at each interface. The infinite fluid spaces are modelled analytically and coupled to the structure using the continuity condition of normal particle velocities on the fluid-structure interfaces.

Mulholland [81] compared various analytical models used for predicting sound transmission through infinite double panels. An STL dip was found at low frequencies due to

the mass-spring-mass resonance. Villot [82] developed a spatial windowing technique for predicting the STL of simply supported rectangular panels. The STL of infinite panels were found using the transfer matrix method. The diffuse-field STL can be found by numerically integrating the power transmission loss coefficient over all possible polar and azimuthal angles of incidence [83]. Kang *et al.* [84] assumed a Gaussian distribution for modelling the non-perfect diffuse field. The windowing technique introduced a geometrical correction coefficient which is formulated as a double integral. For reducing the computational cost of solving the double integral, a reduced-order formulation was derived in reference [85] for isotropic, finite panels. Vigran [86] proposed a simplified spatial windowing technique for estimating sound transmission through isotropic, simply supported panels. In reference [87], Dijckmans *et al.* developed a room-plate coupled model for calculating the STL of finite panels using a transfer matrix method, where the finite size was modelled by expanding the field variables into a series of sin and cos functions. Brunskog [88] studied the influence of the finite cavity on the sound transmission loss of double panels using analytical methods.

1.2.2 Numerical Methods

For simple structures (e.g., thin plates), the classic theories (e.g., Euler-Bernoulli theory, Kirchhoff-Love theory and Mindlin-Reissner theory) can be used straightforwardly. However, for complicated structures, this is difficult. In this section, numerical approaches are reviewed.

Finite Element Method

The finite element (FE) method is widely used for modelling the vibroacoustics of complex structures [89-93]. The mass and stiffness matrices of elements depend on the shape functions which are used. For studying sound transmission, an entire fluid/structure coupled system is often discretised using finite elements. The structure is modelled using solid/plate/beam elements while the fluid spaces are modelled using fluid elements. For

complicated models or analysis at high frequencies (where fine discretisation is required), the FE model has a large number of degrees of freedom. Sometimes a hybrid finite element/boundary element method is used [94, 95]. The structure is fully modelled using FE to find the structural responses (e.g., normal velocities) whilst the boundary element method is used to calculate the radiated pressure.

Spectral Finite Element Method

For spectral finite element method, the assumptions of linear elastodynamics are used to establish the governing partial differential equations. Time and space harmonic motion is assumed along one coordinate axis. The mass and stiffness matrices of a segment of the structure are derived analytically using lengthy, complicated algebraic manipulations [96]. The infinite fluid spaces are modelled analytically. The fluid and structural impedances are found in the wavenumber domain for an incident plane wave and used to calculate the sound transmission loss [96]. However, the use of spectral finite element method involves the derivation of mass and stiffness matrices on a case-by-case situation, which is time-consuming.

Statistical Energy Analysis Method

Statistical energy analysis (SEA) starts with representing a complex vibroacoustic system as a collection of subsystems [97]. The wave propagation characteristics of the subsystems lead to parameters (e.g., modal density, group velocity) for SEA analysis. These subsystems can receive, store, dissipate and transmit energy. The energy transmission between the subsystems is characterised by using a coupling loss factor depending on the junction. For example, Cotoni *et al.* [98] used a statistical energy analysis method to predict the vibroacoustic characteristics of complex panels (e.g., honeycomb-cored panel, stiffened panels). The modal density was found by using a wave and finite element method. Chronopoulos *et al.* [99] developed an SEA model for predicting the vibroacoustic performance of composite cylindrical shells. The wave

characteristics were calculated using a WFE method and used for calculating the modal density and the radiation efficiency. Sound transmission through a finite shell was calculated using the SEA method in reference [100].

In some references [101-104], a hybrid FE/SEA method is used for predicting the structural response to acoustic excitations. The boundary conditions of finite structures are modelled using FE. The entire system is divided into subsystems (e.g., a room-plate-room model). The structure is fully modelled using FE while other subsystems (e.g. acoustic spaces) are represented using the SEA method. Each statistical component is assumed to carry a diffuse wave field. The dynamic stiffness matrix of the deterministic component is coupled to those of the statistical components using diffuse field reciprocity relationships [105]. Langley *et al.* [104] used a hybrid deterministic-statistical method to estimate the vibroacoustic of complex systems with domain coupling. Reynders *et al.* [106] used a hybrid finite-statistical energy analysis method to estimate sound transmission through structures. The hybrid model can take the randomness (e.g. the uncertainty of local mass and stiffness variation) of the acoustic spaces into account. Note that the full FE discretisation of a subsystem can lead to a high computational cost at high frequencies. Decraene *et al.* [107] combined the transfer matrix method with the SEA method to predict the sound transmission through various panels. However, as mentioned before, the derivation of the transfer matrix involves lengthy algebraic manipulation. For complicated structures (e.g., honeycomb-cored panels), deriving the transfer matrix is difficult.

1.3 Wave and Finite Element Method

The early studies (e.g., references [108-110]) of the characteristics of wave propagating through periodic structures using finite elements set the foundation for the emergence of the WFE method. In reference [111], Mace *et al.* proposed the WFE method for predicting the wavenumbers of one-dimensional waveguides, e.g. Euler- Bernoulli beams, simply supported

plate strips and viscoelastic laminates. The formulations for calculating the group velocity, energy, power, etc. were developed. Using this method, only a small segment of the waveguide was modelled using a conventional FE method. The mass and stiffness matrices of the segment were obtained. The periodicity was used to postprocess these matrices to form the eigenproblem whose solution gives the eigenvalues (wave propagation constants) and eigenvectors (representing wave mode shapes). Note that the size of the segment should not be too large or too small. When the segment is too small, round-off errors occur at low frequencies. For a large segment with a coarse mesh, FE discretisation errors would be pronounced. As a rule of thumb, there should be at least six elements per wavelength, but this also depends on the order of the element's shape functions. A detailed discussion about the segment size can be found in ref. [112].

Mace *et al.* [113] extended this method to predict the dispersion relations of two-dimensional homogeneous structures, e.g. a thin plate, an asymmetric laminated plate and a laminated foam-cored sandwich panel. Various forms of eigenproblem depending on the nature of the solution sought were discussed, e.g., linear, quadratic, polynomial and transcendental eigenvalue problems.

In reference [114, 115], Manconi and Mace extended this method to the prediction of wave propagation characteristics of cylindrical and curved panels. Examples of isotropic, orthotropic and laminated curved shells were presented. The eigenproblems established for such structures have the similar forms to those of plane structures. The eigensolution of the eigenproblems yields the dispersion relations (wavenumber, group velocity, etc.). The dispersion curves of fluid-filled elastic pipes were calculated by Maess *et al.* [116] using this method, where a small one-dimensional segment of the structure was modelled using solid (for structure) and fluid (for interior fluid) elements. Note that for cylindrical geometries, the circumferential order of free waves can be specified.

Mace [117] discussed the wave motion and dispersion phenomenon in general terms, i.e., veering, locking and strong coupling effects. In reference [118], Waki applied the WFE method to predict the characteristics of wave propagation in a ring, where a small circumferential segment of the ring was modelled using beam elements. For modelling the curvature, the nodal coordinates of beam elements were rotated by a small angle subtended by the segment. In addition, three methods for calculating the group velocity were described, e.g., using power and energy relation, finite difference method and differentiation of the eigenvalue problem. Finnveden [119] used a finite element method (FEM), the waveguide-FEM, to predict the characteristics of wave propagation (e.g. wavenumber, group velocity, the waveform) of thin-walled structures. The group velocity was calculated using FE formulations.

Renno and Mace [120] proposed a hybrid finite element/ wave and finite element method for calculating the wave transmission and reflection coefficients of joints, where the joint, having arbitrary complex geometry, was modelled using FE while the waveguide was modelled using the WFE method. A similar approach was used by Mitrou *et al.* [121] to model the wave transmission and reflection characteristics of joined two-dimensional structures. Fan *et al.* [122] predict the energy flow in built-up structures using the hybrid method as well.

Waki *et al.* [112, 123] investigated the numerical difficulties concerning the use of the WFE method for predicting the free and forced responses of one-dimensional waveguides. Different approaches (e.g., the transfer matrix, Zhong's method [124]) of formulating the eigenvalue problem were described for calculating wave propagation characteristics. Their research showed that FE discretisation errors occur when the segment is too large while round-off errors occur for the use of very small segments. The latter could be reduced using a super-segment formed from the concatenation of the original small segments. In reference [125], Ichchou *et al.* studied the numerical sensitivity concerning the use of the WFE method for

calculating the energy and group velocities. Again, Zhong's method [124] was used for obtaining a well-conditioned eigenproblem.

Duhamel *et al.* [126] combined the wave approach with finite element method to calculate the forced response of continuous and periodic waveguides. The transfer matrix was used to calculate the eigenvalue and eigenvectors. The eigenvectors form a set of wave basis functions which were used for representing the state variables (stress and displacements) in the wave domain. The orthogonality of left and right eigenvectors was used to overcome the numerical difficulties of inverting spectral matrices. A global dynamic stiffness matrix was found using a subset of the wave basis for calculating the structural response. Waki *et al.* [127] applied this method to calculate the free and forced responses of a tyre. Both finite area and point excitations were considered. Dispersion phenomena of curve veering, non-zero cut-off, etc. were analysed for wave propagation. Again, a reduced wave basis was used to transform the state variables from the physical domain to the wave domain.

In references [128, 129], Renno and Mace extended the WFE method to predict the forced response of one-dimensional [128] and two-dimensional [129] homogenous structures, e.g., finite isotropic and orthotropic laminated panels. The wave characteristics (wavenumbers, eigenvectors) were found from the solution of the eigenproblem and used to calculate the structural response to a convected harmonic pressure. Then the response to a general excitation was calculated by solving the inverse of the Fourier transforms semi-analytically using contour integration and residue theory.

The forced response of axially homogenous circular cylinders (e.g., thick and anisotropic cylinders) was investigated in reference [130]. The cylinders can be arbitrarily complex through the thickness. A small curved segment of the structure was modelled using small flat

elements. Note that the nodal coordinates of the elements were rotated by a small angle for modelling the curvature. Similar modelling approach were presented in references [115, 118].

In reference [131], Mencik proposed a norm-wise error analysis method for reducing the size of the wave basis used for solving the forced response of elastic waveguides. Mencik [132] applied this method to calculate the harmonic forced response of one-dimensional periodic structures with complicated substructures. The large number of internal DOFs of the periodic cell were condensed using component mode synthesis (CMS). This reduction method was also used by Zhou *et al.* [133, 134] and Silva *et al.* [135] to reduce the size of the WFE model for calculating the wave propagation characteristics of periodic structures. Droz *et al.* [136] used this method to study the dispersion characteristics of honeycomb-cored panels with different core geometry. Maurin *et al.* [137, 138] extended the WFE method to predict the dispersion relations of glide, screw and rotational symmetric structures.

Recently, this method was extended to predict sound transmission through, and radiation from various plane and curved structures [139, 140].

1.4 Outline of the Thesis

The goal of this thesis is to extend the wave and finite element (WFE) method to predict the vibroacoustic performances of structures. These structures include various laminated flat panels and cylindrical shells. Formulations for sound transmission through, and radiation from, such structures are developed. The WFE model developed in each chapter is first illustrated by considering a simple structure for which analytical methods are available. In order to validate the WFE model, the WFE predictions are compared with those of the analytical methods. The WFE method is then applied to complicated structures for which finding analytical solutions is difficult or impossible. The predictions made by using a WFE model are also compared to experimental results taken from the literature. Throughout this thesis, ANSYS 13.0 was used

to find the mass and stiffness matrices of a small segment of an entire structure. ANSYS SOLID185 elements were used for discretising solid volumes and ANSYS SHELL181 elements for shells. The calculations involved in post-processing the matrices were performed in MATLAB R2017b. The contents of each chapter are as follows:

Chapter 1 contains an introduction. The current techniques for vibroacoustic analysis are reviewed.

In chapter 2, infinite, continuous, homogeneous and flat panels are considered. The structures are coupled to infinite fluid spaces. The fluid spaces are modelled analytically. The structures are modelled using a WFE method. Formulations are derived for the fluid/structural coupled model for calculating the structural responses. Both acoustic and structural excitations are considered. For an oblique plane wave, the transmission loss coefficient is obtained. The diffuse-field transmission loss is found by a double numerical integration. Sound radiation from structures subjected to general excitation is also considered by using a Fourier transform method. The extended WFE method is first applied to simple panels (e.g. an Euler Bernoulli beam and an isotropic, thin plate) for which analytical solutions are readily obtained and results compared with analytical results. Then this method is applied to complicated structures for which establishing the analytical equations of motion is difficult. These structures include symmetric, laminated panels with an isotropic core and asymmetric panels with an orthotropic core. In the numerical examples, the dispersion curves are also predicted for the structures using a WFE method. The wavenumber characteristics are used for illustrating the underlying physics of high sound transmission which occurs at coincidence.

In chapter 3, sound transmission through finite panels is studied. The panels considered can consist of various layers (e.g. solid and fluid layers) with different physical properties (e.g. material properties, damping loss factors). A segment of a multi-layered system with fluid

layers is considered. For reducing the computational cost, the fluid layers are modelled analytically using a wave model. A spectral dynamic stiffness matrix is found for a general fluid layer. The fluid matrix order does not increase with the layer thickness. The extended WFE method in chapter 1 is used to model an infinite solid layer. Formulations for assembling the spectral dynamic stiffness matrices of the various layers are developed.

A spatial windowing technique is applied to take the effect of the finite size of the structure into account. A geometrical correction factor depending on the structural dimensions is introduced for calculating the sound transmission loss of finite panels. The results are then used to predict sound transmission loss. The formulations are first validated by comparison with simple finite panels and then applied to a range of complicated panels, including double glazing, double steel panels, etc.

In chapter 4, application of the method developed in chapter 2 to a periodic honeycomb-cored panel is investigated. An assumption that structural and acoustic wavelengths are much larger than the dimensions of the periodic cell is made. Again the infinite fluid spaces are modelled analytically, similar to chapter 2. A multi-scale modelling technique is proposed to model the complex geometry of a periodic cell using an FE method. The complex geometry of the periodic cell leads to a large number of DOFs. Guyan reduction (static condensation) is used to reduce the model size to reduce computational cost. Formulations are derived for a reduced WFE model for predicting the sound transmission loss. Various numerical examples are presented to illustrate the homogenised model, which has the advantage of capturing the geometry of any arbitrary complex core. The characteristics of wave propagation through the structures are also analysed. The free wavenumbers predicted by the WFE model are compared with those of equivalent models [22-24, 26]. The predicted sound transmission loss is compared with experimental results.

In chapter 5, sound transmission through circular structures in two dimensions is investigated. An infinitely long cylindrical shell is excited by a parallel line volume source. The fluid spaces are modelled analytically using a Fourier transform method. The sound pressures generated by a volume source are derived. The cross-section of the circular shell is modelled using the WFE method. The acoustic excitations are represented as a sum of harmonic wave components in the circumferential direction. For each acoustic wave component, the WFE formulations can be applied independently. The total response is found by summing those of individual components. A spectral dynamic stiffness matrix is also derived for an isotropic, thin, and cylindrical shell using an analytical method. The WFE predictions are compared with those of the analytical method.

In chapter 6, the WFE formulations developed in chapter 5 are extended to three-dimensional, infinitely long cylindrical shells. A small curved segment of a cylindrical shell is modelled using a conventional FE method. The expressions for the sound pressures generated by a point source exterior to or inside the cavity of the shell are derived analytically. A time-harmonic point force is also considered for structural excitation. A spectral dynamic stiffness matrix is derived for the segment and the structural and acoustic responses are predicted. Various numerical examples are presented to illustrate this method, including an isotropic, thin cylindrical shell and various laminated shells. The predicted sound transmission loss using the WFE model is compared with those of the analytical models. Sound radiation from a fluid-filled pipe excited by a harmonic point force is also considered.

In chapter 7, conclusions are made, and possible future work is proposed.

1.5 Contributions of this Thesis

The original contributions of this thesis include:

1. A wave and finite element method is developed for fluid/structure coupled analysis.

2. Sound transmission through, and radiation from, infinite plane structures are studied using the WFE method.
3. A combination of the WFE method and a spatial windowing technique is used for investigating the characteristics of sound transmission through finite panels.
4. The WFE method is extended for predicting sound transmission through cylindrical shells in two dimensions with internal/external fluids.
5. Sound transmission through cylindrical shells excited by a point source, and radiation from fluid-filled pipes due to structural excitation are studied using the WFE method.

Chapter 2

SOUND TRANSMISSION THROUGH, AND RADIATION FROM, INFINITE PANELS

This chapter concerns sound transmission through infinite, flat, uniform panels, and sound radiation from structural excitation. Analytical solutions are available for simple cases. Here, a WFE method is developed for arbitrary construction through the thickness.

2.1 Introduction

The acoustic performance of panels is of great importance in many applications (e.g. architectural, automotive and aeronautical). Over the years, there has been a concerted effort to develop methods for estimating the sound transmission loss (STL) characteristics of various panels. For simple structures such as beams and thin isotropic plates, it is straightforward to calculate the sound transmission analytically [7]. For complicated structures such as sandwich panels, laminated fibre-reinforced composites and honeycomb-cored panels, analytical methods become difficult and involve various assumptions and approximations. For example, the assumption of the incompressibility of the core was made by Kurtze and Watters [12] to predict the TL characteristics of sandwich beams, which leads to the disappearance of symmetric wave propagation in the structure. The assumption of linear displacement fields through the thickness of panels was made by Lord *et al.* [13] and Moore and Lyon [14] to study the characteristics of sound transmission through various sandwich panels. These assumptions generally become less accurate as frequency increases. Establishing the equations of motion for similar or even more complex structures becomes a formidable task.

Alternatively, numerical solutions to structural/acoustic coupled problems (e.g. references [92, 95]) can be found using finite element (FE) and/or boundary element methods. However, such models have drawbacks as they become large at higher frequencies, resulting in high computational costs. Some authors use a statistical energy analysis (SEA) method [98] or a hybrid method (FE-SEA) [104] to predict the sound insulation performances of panels. The finite panels are modelled deterministically using the FE method for the hybrid model. An alternative method, developed here, is the wave and finite element (WFE) method. In essence, the WFE method involves meshing just a small segment of the structure using any FE software, with the resulting mass and stiffness matrices being post-processed and periodicity conditions applied to yield the wave characteristics of the whole structure. The WFE method, reviewed in reference [141] has been applied to predict the characteristics of wave propagation in structures.

In this chapter, previous work is extended to predict sound transmission through infinite, plane structures using the WFE method. A single segment of the panel is meshed through the thickness using a conventional FE approach using an in-house or commercial code. The dynamic stiffness matrix of this segment is then post-processed and assembled with the dynamic stiffnesses of the fluids to determine the structural and acoustic responses. Sound radiation caused by excitation of the structure by forces is also considered, with the emphasis being placed on the far-field radiation from a point force excitation.

2.2 Theory and Formulation

The theory and formulation concerning the extension of the WFE method to predict the STL of infinite panels are presented in this section. The infinite fluid spaces are modelled using an analytical method in section 2.2.1. The infinite solid structure is modelled using the WFE method in section 2.2.2. The interaction between the fluid and the structure is illustrated in section 2.2.3. Various excitations are introduced in section 2.2.4 including acoustic plane waves, and general forces (e.g., a time-harmonic point force) applied to the structure. The total

spectral dynamic stiffness matrix of the infinite system is derived in section 2.2.5 and the acoustic and structural responses calculated. The diffuse-field STL, and sound radiation in the far-field are considered in sections 2.2.6 and 2.2.7 respectively. Sections 2.3 and 2.4 present examples.

2.2.1 Fluid Space

In this section, an infinite fluid space is modelled analytically. The expression of the sound pressure for acoustic plane waves is derived.

Assume the fluid is homogeneous, inviscid, compressible, the continuity (conservation of mass) equation can be written as (see chapter 5 in reference [10])

$$\frac{\partial \rho}{\partial t} + \nabla \cdot (\rho \mathbf{u}) = 0 \quad (2.1)$$

where $\mathbf{u} = u\mathbf{i} + v\mathbf{j} + w\mathbf{k}$ represents the particle velocity vector (u, v, w are the moduli amplitudes of the particle velocity components, and $\mathbf{i}, \mathbf{j}, \mathbf{k}$ are unit vectors in the $x, y,$ and z directions respectively; ρ is the density; $\nabla \cdot ()$ is the divergence operator. Let $\rho = \rho_0(1 + s)$ where s is the condensation which is assumed to very small, and ρ_0 is the mean density being independent of time. Neglecting second-order terms results in a linearised continuity equation

$$\rho_0 \frac{\partial s}{\partial t} + \nabla \cdot (\rho_0 \mathbf{u}) = 0. \quad (2.2)$$

According to the linearised momentum equations (see equation 1.5 in reference [7]), the acoustic pressure can be related to the particle velocities by

$$\frac{\partial p}{\partial x} + \rho_0 \frac{\partial u}{\partial t} = 0, \quad (2.3)$$

$$\frac{\partial p}{\partial y} + \rho_0 \frac{\partial v}{\partial t} = 0, \quad (2.4)$$

$$\frac{\partial p}{\partial z} + \rho_0 \frac{\partial w}{\partial t} = 0, \quad (2.5)$$

where p denotes the instantaneous acoustic pressure. Taking the derivatives of Eqs. (2.3-2.5) with respect to variables x, y, z respectively leads to

$$\nabla \cdot \left(\rho_0 \frac{\partial \mathbf{u}}{\partial t} \right) = -\nabla^2 p. \quad (2.6)$$

Substituting Eq. (2.6) into the partial derivative of Eq. (2.2) with respect to time t leads to

$$\nabla^2 p = \rho_0 \frac{\partial^2 s}{\partial t^2}. \quad (2.7)$$

The adiabatic bulk modulus \wp can be written in terms of pressure p , and condensation s as [10]

$$\wp = p/s. \quad (2.8)$$

Note that [10]

$$\gamma P_0 = \wp, \quad (2.9)$$

where γ is the ratio of specific heat and P_0 is the mean fluid pressure.

Inserting Eq. (2.9) into Eq. (2.8) yields

$$s = p/\gamma P_0. \quad (2.10)$$

Again, inserting Eq. (2.10) into Eq. (2.7) gives

$$\frac{\partial^2 p}{\partial x^2} + \frac{\partial^2 p}{\partial y^2} + \frac{\partial^2 p}{\partial z^2} = \frac{1}{c^2} \frac{\partial^2 p}{\partial t^2} \quad (2.11)$$

where $c = \sqrt{\gamma P_0 / \rho_0}$ is the frequency-independent speed of sound. Assuming time-harmonic motion of the form $\exp(i\omega t)$, one solution to Eq. (2.11) can be written in the separable form (see chapter 1 in reference [7]) as

$$p(x, y, z) = \tilde{p} \exp(i\omega t - ik_x x - ik_y y - ik_z z), \quad (2.12)$$

where \tilde{p} denotes the complex pressure amplitude of a plane wave which has constant amplitude and phase on any plane perpendicular to the direction of propagation and k_x, k_y, k_z are the wavenumber components in the x , y , and z directions respectively.

2.2.2 Solid Structure

In this section, an infinite, continuous, flat structure is modelled. In practical applications, the structure is typically of complicated, layered construction so that while an analytical/numerical solution might be able to be developed, it is simpler to develop an FE model. The WFE method involves modelling a small segment of the structure using the FE method. From the FE model, the mass and stiffness matrices of the segment are determined. Note that the FE analysis can be done using any software package. The mesh might include any number of elements through the thickness of the structure. This makes the approach particularly suitable for modelling laminates, sandwich panels etc. The advantage of this method is that users do not need to develop analytical models for the core deformation through the thickness.

In the WFE model shown in figure 2.1, no edge or internal DOFs are assumed but they can be included straightforwardly [113]. The governing equation of the segment, assuming time-harmonic behaviour and neglecting damping, is

$$[\mathbf{K} - \omega^2 \mathbf{M}] \mathbf{q} = \mathbf{f} + \mathbf{e}, \quad (2.13)$$

where \mathbf{q} , \mathbf{f} , and \mathbf{e} are $(4n \times 1)$ vectors of nodal DOFs, internal and external nodal forces respectively; \mathbf{M} and \mathbf{K} are the mass and stiffness matrices of the segment and n represents the number of degrees of freedom (DOFs) throughout the cross-section at each corner. Damping can be included by a viscous damping matrix \mathbf{C} or by \mathbf{K} being complex.

For time and space harmonic excitation, the nodal displacements are related by periodicity conditions, and the internal nodal forces must satisfy equilibrium equations. The governing equation can then be reduced (see section 2 in reference [113]). If there are internal nodes, they can be eliminated via dynamic condensation. The discretisation must not be too coarse, e.g. the element size should not be too large compared to the shortest wavelength of structural or acoustic motion. Otherwise, the discretised model will not accurately describe the motion of the structure. Details concerning numerical issues of applying the WFE method can be found in reference [112].

2.2.3 Fluid-Structure Interaction

Consider the situation in figure 2.2. An incident plane wave excites a structure of thickness h whose motion, in turn, excites reflected and transmitted waves in the fluids adjacent to the top and bottom surfaces of the structure respectively. The structure lies parallel to the x - y plane. The regions $z > 0$ and $z < -h$ are occupied by acoustic fluids 1 and 2 with wave speeds c_1 and c_2 respectively. An acoustic plane wave

$$\tilde{p}_i \exp\left[i(-k_x x - k_y y + k_{z,1} z)\right] \quad (2.14)$$

is incident in fluid 1 from $z > 0$ at an angle θ to the normal, giving rise to reflected and transmitted waves

$$\tilde{p}_r \exp\left[i(-k_x x - k_y y - k_{z,1} z)\right], \quad \tilde{p}_t \exp\left[i(-k_x x - k_y y + k_{z,2} z)\right], \quad (2.15)$$

where the time-harmonic dependence $\exp(i\omega t)$ has been suppressed; The wave amplitudes are denoted by \tilde{p}_i , \tilde{p}_r , and \tilde{p}_t respectively. Inserting Eq. (2.15) into Eq. (2.11) yields

$$k_{z,1}^2 + k_x^2 + k_y^2 = k_1^2, \quad k_{z,2}^2 + k_x^2 + k_y^2 = k_2^2, \quad k_{1,2} = \omega / c_{1,2}, \quad (2.16)$$

where

$$k_x = k_1 \sin \theta \cos \phi, \quad k_y = k_1 \sin \theta \sin \phi \quad (2.17)$$

are the trace wavenumber components of the incident wave, ϕ denotes the propagation direction of an acoustic trace wave. Note that the trace wavenumber components are the same for all three waves. Therefore, the pressures applied on the upper ($z_1 = 0$) and lower ($z_2 = -h$) surfaces by the acoustic waves can be written as

$$p_1 = -(\tilde{p}_i + \tilde{p}_r) \exp(-ik_x x - ik_y y + ik_{z,1} z_1) \quad (2.18)$$

and

$$p_2 = \tilde{p}_t \exp(-ik_x x - ik_y y + ik_{z,2} z_2) \quad (2.19)$$

respectively.

Then, from the continuity of the fluid and structural displacements, inserting Eq. (2.18) and Eq. (2.19) into Eq. (2.5) respectively gives,

$$\tilde{p}_i - \tilde{p}_r = D_{f,1} w_1, \quad \tilde{p}_t = D_{f,2} w_2, \quad (2.20)$$

where w_1 and w_2 are the displacements of the upper and lower surfaces respectively, and

$$D_{f,1} = \frac{-i\rho_1 \omega^2}{k_{z,1}}, \quad D_{f,2} = \frac{-i\rho_2 \omega^2}{k_{z,2}} \quad (2.21)$$

are the dynamic stiffnesses of the fluids.

2.2.4 Acoustic/Force Excitation

For acoustic excitation, the pressures applied on the structure are described by Eq. (2.18) and Eq. (2.19). In an FE discretisation, this results in external nodal forces on those DOFs that correspond to displacements in the z -direction of the upper and lower surfaces, e.g. w_1 and w_2 . Coupling vectors \mathbf{u}_1 and \mathbf{u}_2 are defined, whose elements are all zero apart from that which corresponds to w_1 and w_2 respectively, which equals 1. Therefore

$$w_{j,1} = \mathbf{u}_1^T \mathbf{q}_j, \quad w_{j,2} = \mathbf{u}_2^T \mathbf{q}_j, \quad (2.22)$$

where j represents the j -th corner of the segment in figure 2.1(b) and \mathbf{q}_j are vectors of degrees of freedoms of the j -th hyper-node, which is the concatenation of all the nodes at the corner of the segment.

The distributed external excitation could merely be lumped at the nodes. Preferably, consistent nodal forces can be calculated as follows. For example, \mathbf{e}_j can be written as

$$\mathbf{e}_j = (p_i + p_r) \alpha_j \mathbf{u}_1 - p_i \beta_j \mathbf{u}_2, \quad (2.23)$$

where

$$\alpha_j = \iint e^{-ik_x x - ik_y y + ik_{z,1} z} N_{j,1}(x, y) dx dy, \quad (2.24)$$

$$\beta_j = \iint e^{-ik_x x - ik_y y - ik_{z,2} z} N_{j,2}(x, y) dx dy, \quad (2.25)$$

where $N_{j,1}(x, y, z)$ and $N_{j,2}(x, y, z)$ are the shape functions associated with the w -displacements of the upper and lower surfaces respectively. Typically, Eqs. (2.24, 2.25) are solved by numerical integration (e.g. using a Gauss–Legendre quadrature method [83]). If there are internal nodes, consistent nodal forces can be calculated for each and combined via dynamic

condensation to yield \mathbf{e}_j at the corners of the segment. Eq. (2.23) explicitly separates the excitation into two components, one on each of the surfaces of the structure.

For a general, external force loading, the loading can be applied to the structure in any direction [128-130]. Time-harmonic excitation $P(x, y, z)$ per unit volume is assumed to act on in the z -direction of the structure. This loading is resolved into consistent nodal forces. Here only a loading $P(x, y, z)$ in one direction is considered. If there are additional loading components (e.g. acting in the x - or y -directions), their contributions can be simply added to the consistent nodal forces. The only restriction is that each component of a general excitation force is separable and can be written in the form $P(x, y, z) = P_{xy}(x, y)P_z(z)e^{i\omega t}$. Suppressing the time dependence, it is useful to define the following Fourier transform pair,

$$P(x, y, z) = P_z(z) \int_{-\infty}^{+\infty} \int_{-\infty}^{+\infty} \tilde{P}(k_x, k_y) e^{-ik_x x} e^{-ik_y y} dk_x dk_y, \quad (2.26)$$

where

$$\tilde{P}(k_x, k_y) = \frac{1}{4\pi^2} \int_{-\infty}^{+\infty} \int_{-\infty}^{+\infty} P_{xy}(x, y) e^{ik_x x} e^{ik_y y} dx dy. \quad (2.27)$$

They enable any external loading $P(x, y, z)$ to be expressed as the superposition of space harmonics. For each pair of wavenumbers (k_x, k_y) , consistent nodal forces can be written as

$$\mathbf{e}_j = \iiint \tilde{P}(k_x, k_y) e^{-ik_x x} e^{-ik_y y} P_z(z) N_j(x, y, z) dx dy dz \mathbf{u}_{1,2} \quad (2.28)$$

where the subscript of \mathbf{e} is j , the subscript of \mathbf{u} is “1” or “2” and $N_j(x, y, z)$ are the element shape functions, If a point force is applied on the upper or lower surface, then the shape functions $N_j(x, y, z)$ become $N_{j,1}(x, y)$ and $N_{j,2}(x, y)$ respectively. These nodal forces can be included in Eq. (2.13) to calculate the response and acoustic radiation.

Consider, for example, the case where a point force of strength F acts on the surface at $z=0$. This force leads to a pressure $P(x, y, z) = F\delta(x-x_0)\delta(y-y_0)$ acting on the surface of the plate. Taking the Fourier transform yields

$$\tilde{P}(k_x, k_y) = \frac{1}{4\pi^2} \int_{-\infty}^{+\infty} \int_{-\infty}^{+\infty} F\delta(x-x_0)\delta(y-y_0)e^{ik_x x} e^{ik_y y} dx dy = \frac{1}{4\pi^2} F e^{ik_x x_0} e^{ik_y y_0}. \quad (2.29)$$

The consistent nodal forces of the point force can be obtained by Eq. (2.29) straightforwardly.

2.2.5 Spectral Dynamic Stiffness Matrix and Response

In this section, the FE model of the periodic cell is post-processed using periodic structure theory and equilibrium conditions. The boundary DOFs of the FE model are further condensed. A spectral equation of motion is derived for the system.

The most straightforward solution method, and that which is most useful if fluid loading is significant, is to apply the periodicity condition [38]

$$\mathbf{q}_2 = \lambda_x \mathbf{q}_1, \quad \mathbf{q}_3 = \lambda_y \mathbf{q}_1, \quad \mathbf{q}_4 = \lambda_x \lambda_y \mathbf{q}_1, \quad (2.30)$$

where λ_x and λ_y are wave propagation constants, and can be expressed as

$$\lambda_x = e^{-ik_x L_x}, \quad \lambda_y = e^{-ik_y L_y}. \quad (2.31)$$

Equation (2.30) can be rewritten as

$$\mathbf{q} = \mathbf{\Lambda}_R \mathbf{q}_1, \quad \mathbf{\Lambda}_R = \begin{bmatrix} \mathbf{I} \\ \lambda_x \mathbf{I} \\ \lambda_y \mathbf{I} \\ \lambda_x \lambda_y \mathbf{I} \end{bmatrix}, \quad (2.32)$$

while equilibrium at hyper-node 1 gives

$$\Lambda_L \begin{bmatrix} \mathbf{f}_1 \\ \mathbf{f}_2 \\ \mathbf{f}_3 \\ \mathbf{f}_4 \end{bmatrix} = \mathbf{0}, \quad \Lambda_L = \begin{bmatrix} \mathbf{I} & \lambda_x^{-1} \mathbf{I} & \lambda_y^{-1} \mathbf{I} & \lambda_x^{-1} \lambda_y^{-1} \mathbf{I} \end{bmatrix}. \quad (2.33)$$

Substituting Eq. (2.32) into Eq. (2.13) and premultiplying by Λ_L results in

$$\mathbf{D}_s \mathbf{q}_1 = (\mathbf{e}_1 + e^{ik_x L_x} \mathbf{e}_2 + e^{ik_y L_y} \mathbf{e}_3 + e^{ik_x L_x} e^{ik_y L_y} \mathbf{e}_4), \quad (2.34)$$

where

$$\mathbf{D}_s = \Lambda_L [\mathbf{K} - \omega^2 \mathbf{M}] \Lambda_R \quad (2.35)$$

is the reduced dynamic stiffness matrix of the structure. Noting the dynamic stiffnesses of the fluids in Eq. (2.20) and the expressions for the excitation in Eq. (2.23) and Eq. (2.34) reduces to

$$\mathbf{D} \mathbf{q}_1 = 2 \tilde{p}_i \varepsilon_1 \mathbf{u}_1, \quad (2.36)$$

where

$$\mathbf{D} = \mathbf{D}_s + \varepsilon_1 D_{f,1} \mathbf{u}_1 \mathbf{u}_1^T + \varepsilon_2 D_{f,2} \mathbf{u}_2 \mathbf{u}_2^T, \quad (2.37)$$

$$\varepsilon_1 = \alpha_1 + e^{ik_x L_x} \alpha_2 + e^{ik_y L_y} \alpha_3 + e^{ik_x L_x} e^{ik_y L_y} \alpha_4, \quad (2.38)$$

$$\varepsilon_2 = \beta_1 + e^{ik_x L_x} \beta_2 + e^{ik_y L_y} \beta_3 + e^{ik_x L_x} e^{ik_y L_y} \beta_4, \quad (2.39)$$

where

$$\begin{aligned} \alpha_j &= \iint e^{-ik_x x - ik_y y} N_{j,1}(x, y, z) dx dy, \\ \beta_j &= \iint e^{-ik_x x - ik_y y - ik_z h} N_{j,2}(x, y, z) dx dy. \end{aligned} \quad (2.40)$$

In equation (2.40), the shape functions $N_{j,1}(x, y, z)$ and $N_{j,2}(x, y, z)$ are associated with the w -displacements of the upper and lower surfaces, respectively. Note that the dynamic stiffnesses of the fluids contribute to the relevant diagonal elements of \mathbf{D} . Eq. (2.36) can be solved for the response vector \mathbf{q}_1 . The reflected and transmitted pressures at the surfaces of the structure then follow from Eq. (2.20) as

$$\tilde{p}_r = \tilde{p}_i - D_{f,1} \mathbf{u}_1^T \mathbf{q}_1, \quad \tilde{p}_t = D_{f,2} \mathbf{u}_2^T \mathbf{q}_1. \quad (2.41)$$

An alternative solution method is to decompose the structural response into free wave components excited by the incident pressure. This approach can be used to find the response to arbitrary structural excitation [128-130]. If fluid loading effects are negligible, then peaks in the response or sound transmission loss can be related to strong excitation of free waves in the structure, assisting in the interpretation of the behaviour.

2.2.6 Sound Transmission Loss and Diffuse Incident Field

The sound transmission loss for a wave incident at a pair of angles (θ, ϕ) is defined as

$$TL = -10 \log [\tau(\theta, \phi)], \quad (2.42)$$

where the power transmission coefficient $\tau(\theta, \phi)$ is the ratio of the transmitted and incident powers, i.e.

$$\tau(\theta, \phi) = \frac{\operatorname{Re} \left\{ (k_{z,2} / \rho_2) |p_t|^2 \right\}}{(k_{z,1} / \rho_1) |p_i|^2}. \quad (2.43)$$

Note that in equation (2.43) the numerator can be complex value given different fluids (say air to water) in the half-spaces. For a diffuse incident field the sound transmission loss, found by integrating over all possible incident angles θ to the normal direction and heading angles ϕ of wave propagation over the structure, is

$$\tau_d = \frac{1}{\pi} \int_0^{2\pi} \int_0^{\pi/2} \tau(\theta, \phi) \sin \theta \cos \theta d\theta d\phi. \quad (2.44)$$

This integral would typically need to be evaluated numerically.

There are various integration functions available in MATLAB, but note that some of them have very low accuracy for calculating the integral of equation (2.43). The function QUAD, for example, approximates the integral using recursive adaptive Lobatto quadrature using only an absolute error of 1×10^{-6} . Care must be taken when using such numerical integration routines to evaluate the double integral defined by eq. (2.43) as the integrand typically contains sharp peaks and troughs which can be missed if the resolution of the method is not sufficiently high. In order to achieve good accuracy at reasonable numerical expense, it is preferable to divide the whole integral domain into smaller subdomains without internal singularities/peaks. Then applying numerical integration schemes to each subdomain and summing the results together. Also, note that in some cases the upper limit of the integration of θ is suggested to be truncated at some angle (the angle 78° is suggested in [7] to allow for non-diffuseness of the incident field).

2.2.7 Sound Radiation

The far-field sound pressure is considered in this section.

In figure 2.3, for example, assume the half-space $z > 0$ above the panel is occupied by fluid with density ρ_1 and sound velocity c_1 while the fluid with density ρ_2 and sound velocity c_2 occupies the other half-space $z \leq -h$. The sound pressure in fluid 1 is governed by the wave equation,

$$\frac{\partial^2 p_{\text{rad}}}{\partial x^2} + \frac{\partial^2 p_{\text{rad}}}{\partial y^2} + \frac{\partial^2 p_{\text{rad}}}{\partial z^2} = \frac{1}{c_1^2} \frac{\partial^2 p_{\text{rad}}}{\partial t^2}. \quad (2.45)$$

where the subscript “rad” denotes the radiated sound pressure. Applying the Fourier transform to Eq. (2.45) gives, for time-harmonic excitation,

$$\left(k_1^2 - k_x^2 - k_y^2 + \frac{\partial^2}{\partial z^2} \right) \tilde{p}_{\text{rad}}(k_x, k_y, z) = 0. \quad (2.46)$$

The solution to Eq. (2.46) is given by

$$\tilde{p}_{\text{rad}}(k_x, k_y, z) = A \exp(-ik_{z,1}z), \quad (2.47)$$

where

$$k_{z,1} = \begin{cases} \sqrt{k_1^2 - k_x^2 - k_y^2} & k_1^2 > k_x^2 + k_y^2 \\ -i\sqrt{k_x^2 + k_y^2 - k_1^2} & k_1^2 \leq k_x^2 + k_y^2 \end{cases}, \quad (2.48)$$

and A is determined by requiring that the fluid particle displacement in the z -direction at $z = 0$ is equal to the surface displacement w_1 . This requirement gives

$$A = \frac{-i\omega^2 \rho \tilde{w}_1(k_x, k_y)}{k_{z,1}}. \quad (2.49)$$

The radiated sound pressure is thus given by

$$p_{\text{rad}} = \frac{1}{4\pi^2} \int_{-\infty}^{+\infty} \int_{-\infty}^{+\infty} \frac{-i\omega^2 \rho \tilde{w}_1(k_x, k_y)}{\sqrt{k_1^2 - k_x^2 - k_y^2}} e^{-ik_x x} e^{-ik_y y} e^{-ik_z z} dk_x dk_y. \quad (2.50)$$

For observation points in the acoustic far-field, the double integral can be evaluated asymptotically using the method of stationary phase which gives the approximate expression (see section 8.7 in reference [9])

$$p_{\text{rad}}(R, \theta, \phi) \approx -\omega^2 \rho \tilde{w}_1(\bar{k}_x, \bar{k}_y) \frac{e^{-ikR}}{2\pi R}, \quad (2.51)$$

where the stationary phase wavenumbers are

$$\bar{k}_x = k_1 \sin \theta \cos \phi, \quad \bar{k}_y = k_1 \sin \theta \sin \phi, \quad (2.52)$$

and correspond to wavenumber components in the x and y directions of a plane-wave propagating towards the observer from the origin of the coordinate system. The sound pressure in fluid 2 follows in a similar manner.

2.3 Illustrative Examples

A series of numerical examples demonstrating the WFE method are presented in this subsection. These examples include sound transmission through, and radiation from, one-dimensional (1D), and two-dimensional (2D) thin, homogenous, and isotropic panels. For these cases, analytical methods are available for predicting the acoustic response and thus the results obtained using the WFE method are compared with results obtained from the analytical models (see equations 5.27-5.36) in reference [7]).

2.3.1 One-Dimensional Isotropic Panel

First, consider an infinite, thin, and isotropic beam. The material properties are: elastic modulus $E = 2 \times 10^{11} \text{ Pa}$, density $\rho = 7800 \text{ kg/m}^3$, and thickness $h = 3 \text{ mm}$. A small segment of length 10mm is taken and modelled using one ANSYS BEAM 181 element having two nodes. Each node has two DOFs, flexural displacement and rotation about the z -axis. The STL is predicted using the WFE method. Figure 2.4 shows the predictions (solid black curve), together with the analytical (dotted red curve) results (using equation 5.38(a) in reference [7]). It can be seen that the agreement is excellent. For the oblique STL, a dip can be observed at 7.28 kHz due to coincidence: at this frequency the trace wavenumber of the incident acoustic wave equals the wavenumber of the bending wave of the structure. For the diffuse field, the coincidence frequency is seen to be at 4.33 kHz.

2.3.2 Two-Dimensional Isotropic Panel

Another example is a 2D isotropic, thin plate. The thickness of the plate is 3mm. A small segment of the plate is meshed using a single rectangular, 4-noded element of sides $L_x = L_y = 3mm$. There are three DOFs at each node, transverse displacement and the two rotations θ_x and θ_y . The mass and stiffness matrices of the thin plate element with cubic shape functions can be found in reference [93] (although note typographical errors).

Assume the plate is submerged in air. The material properties are listed in table 2.1. Figure 2.5(a) shows the STL, predicted from equation 5.38(a) in reference [7], and from the WFE solution, for an angle of incidence $\theta = 60^\circ$. The agreement can be seen to be very good. There is a notch in the STL curve at 5500 Hz due to coincidence. For this choice of structure and fluid, the fluid loading effects are generally weak, although it should be noted that they are significant at and around the coincidence frequency. Figure 2.5(b) shows the diffuse field STL, calculated by numerical integration. Again the agreement is very good.

Consider the case where fluid 1 in the half-space $z > 0$ is air, and fluid 2 is vacuum. Figure 2.6(a) shows the far-field sound pressure radiated from the point-excited plate at 8 kHz. The agreement between the analytical results and the WFE predictions is very good. A peak in the sound pressure can be seen, at a radiation angle of $\theta = 45.6^\circ$, when the trace wave speed equals that of the propagating bending wave.

For the case where the half-space $z > 0$ is occupied by water, figure 2.6(b) shows the radiated pressure for an excitation frequency $f=40$ kHz. The WFE solution shows a good agreement with the analytical solution again. The excitation frequency is below the coincidence frequency.

2.4 Application Examples

In this subsection, the extended WFE method is used to calculate sound transmission through an antisymmetric, cross-ply sandwich panel for which developing an analytical solution is difficult. A complex symmetric sandwich panel with an orthotropic core is also considered. The characteristics of wave propagation in these structures are also studied. The wave dispersion curves are used to interpret the underlying physical mechanism for the transmission loss characteristics.

2.4.1 Symmetric Sandwich Panel with Orthotropic Core

The configuration of the panel considered in this section is a symmetric panel with an orthotropic core. The material properties are shown in table 2.1. It consists of three layers. The thicknesses of the core and each skin are 6.35mm and 0.5mm respectively. The face sheets of the segment are meshed by using two ANSYS SOLID185 elements. Six elements of the same thickness and sides $L_x=L_y=1\text{mm}$ are used for the core. Relevant material properties are shown in table 1. Structural damping is neglected.

1. Sound Transmission Loss

Figure 2.7(a) shows the real-valued dispersion curves for structural waves with the propagation angle $\phi=0^\circ$ to the positive x -direction. Complicated behaviour is observed, with cut-off frequencies at around 5 kHz and 35 kHz respectively. The detailed wavenumber behaviour around the first cut-off frequency is shown in figure 2.7(b). There are three wave branches below approximately 5 kHz, the bending wave (branch a), shear wave (branch b) and extensional wave (branch c), which resemble the dispersion behaviour of an isotropic plate at low frequencies. The shear wave branch starts veering at about 35 kHz.

The sound transmission loss for acoustic plane waves incident at $\theta=20^\circ$ and $\theta=50^\circ$ is shown in figure 2.8(a). For the acoustic plane-wave incident at $\theta=50^\circ$, acoustic coincidence is

associated with the antisymmetric bending-like mode of propagation in the panel. The corresponding acoustic coincidence frequency can be seen in figure 2.8(b). In comparison, the trace wave speed of the plane wave incident at $\theta = 20^\circ$ is faster than the flexural wave speed of the panel during the whole frequency range so that coincidence does not occur. Also, it is worthwhile to note that the symmetric wave mode does not propagate in the frequency band shown. The configuration of this sandwich panel shifts the dilatational mode to higher frequencies. The diffuse field STL of the symmetric sandwich panel is shown in figure 2.9.

2. Sound Radiation

For the case of air occupying the upper half space, figure 2.10(a) shows the normalised sound pressure radiated from the point-excited panel at 20 kHz. The point force is applied at the origin of the coordinates in figure 2.3. Since the excitation frequency is above coincidence and the core is orthotropic, peaks can be seen for various combinations of angles θ and ϕ . For the case where water occupies the space $z > 0$, the normalised pressure in the far field is shown in figure 2.10(b). The excitation frequency is far below the lowest coincidence frequency so that no peak exists in the radiated pressure.

2.4.2 Anti-Symmetric Sandwich Panel with Isotropic Core

In this section, sound transmission through an asymmetric, angle-ply, laminated sandwich panel is considered. The two outer skins comprise four sheets of 0.25mm graphite-epoxy material. The stacking sequences of the bottom and the top skins are $[45/-45/-45/45]$ and $[-45/45/45/-45]$ respectively. The core is a 5-mm thick foam. Four ANSYS SOLID185 elements of sides $L_x = L_y = 1\text{mm}$ are used to mesh each skin of a segment taken from the panel while five ANSYS SOLID185 elements are used for the core. Material properties for the skins and the core are shown in table 2.1. The structural damping is neglected here for simplicity

since the propagating wavenumbers are pure-real but could be included by using a complex Young's modulus.

1. Sound transmission loss

The pure real dispersion curves are shown in figure 2.11(a). There are three wave types below approximately 22 kHz, which are the flexural wave (branch *a*), shear wave (branch *c*) and extensional wave (branch *b*) respectively. With the increase of frequency, two additional waves (branch *d* and branch *e*) cut on at around 22 kHz involving out-of-phase motion of the skins of the panel. At around 39.2 kHz, wave branch *b* cuts off with non-zero real wavenumber while branch *f* appears above the cut-on frequency of approximately 39.8 kHz.

The complexity of the high order wave types is such that the veering part of the extensional wave (branch *b*) spans a comparatively broader frequency range while the veering part of branch *f* exists over a fairly narrow frequency region. The detailed wavenumber behaviour around 39 kHz is shown in figure 2.11(b).

For acoustic plane-waves incident on the panel, the STL is a function of frequency, the angle of incidence θ with respect to the normal to the panel and the direction of wave propagation ϕ over the surface of the panel. When the trace wavenumber of the incident wave equals that of the symmetric or antisymmetric wave mode at a given frequency, coincidence leads to a notch in the STL. The acoustic coincidence frequencies in figure 2.12(a), for instance, correspond to the frequencies in figure 2.12(b) where the minimum STL occurs.

As can be seen from figure 2.12(a), both the symmetric propagating wave (the veering part of branch *b*) and the antisymmetric bending wave (branch *a*) propagate in the frequency range shown. Both modes contribute to the occurrence of coincidence. Compared to the isotropic plate, the dispersion curves of the laminated panel are more complex, and the

behaviour of higher order waves is significant in affecting the acoustic performance. For the diffuse incident field, the STL is shown in figure 2.13.

2. Sound radiation

Consider the case where air occupies the space $z > 0$ and the half space $z < -h$ is a vacuum. Figure 2.14(a) shows the radiated sound pressure normalized to that of $\theta = 0^\circ$ for an excitation frequency $f = 10$ kHz. Again acoustic coincidence leads to the maximum radiated pressure at the coincidence angle. Figure 2.14(b) shows the sound pressure for the same excitation frequency where $z > 0$ is occupied by water, the excitation frequency being smaller than the coincidence frequency.

2.5 Conclusions

This chapter described an approach for the prediction of sound transmission through infinite structures coupling two-dimensional and three-dimensional acoustic spaces. It involves a finite element analysis of a small segment of the structure to determine the mass and stiffness matrices, coupled to analytical models of the acoustic spaces, which are then post-processed in a straightforward manner to yield the structural and acoustic responses. The prediction of sound radiation from structures excited by a time-harmonic point force was also considered.

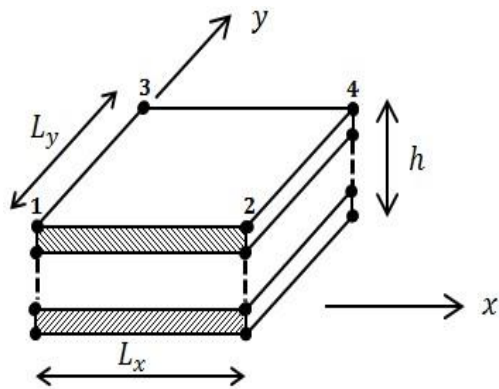
Various numerical examples were presented to validate and illustrate the method. This approach was first demonstrated by one-dimensional and two-dimensional thin, isotropic beams and plates, for which analytical solutions are well-known. Numerical predictions using the WFE model agree very well with the analytical results. Then two, more complicated, examples, namely antisymmetric and symmetric laminate sandwich panels, were considered.

The method uses FE matrices developed using any in-house or commercial code and provides predictions at very small computational cost. There are various possible numerical

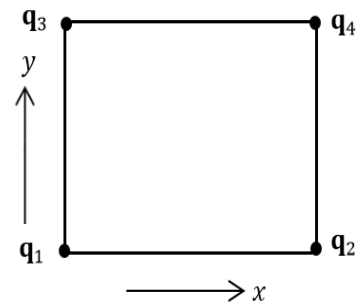
issues. In addition to those described in the reference [112], the segment size must be small compared to the acoustic wavelength for proper resolution of the acoustic loads.

Due to the assumption of the infinite size, however, significant discrepancies can be observed between the predicted STL and the measurements for finite panels [82]. In the next chapter, the finite size of the structure will be considered for improving the agreement with the measurements.

Figures



(a)



(b)

Figure 2.1: WFE model; (a) FE mesh of a segment of the structure. The mesh can contain any number of elements through the thickness of the structure and along the length of the segment; (b) FE mesh with hypernodes at each corner of the segment. The vectors of nodal DOFs are the concatenation of the individual nodal quantities in figure 2.1(a).

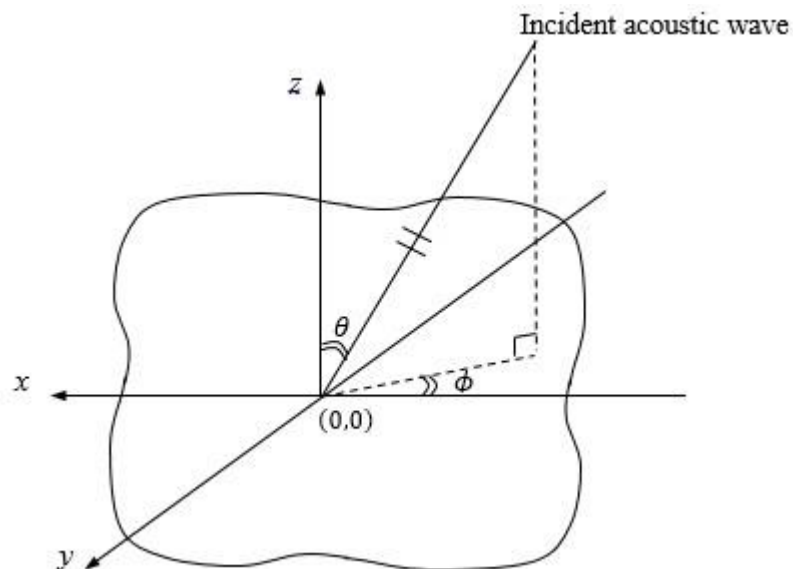


Figure 2.2: Structure lying in the x - y plane.

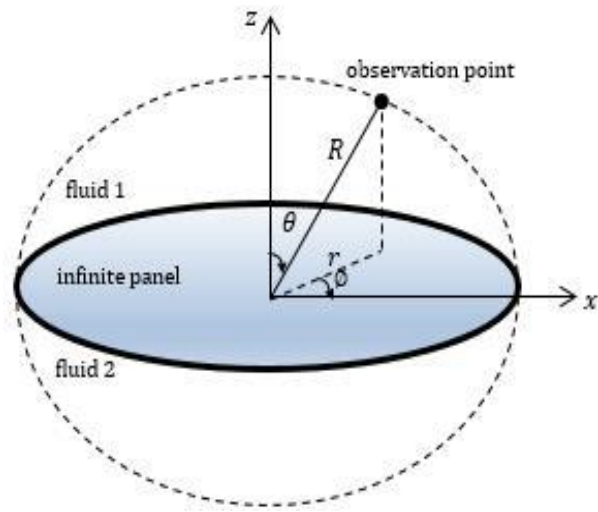


Figure 2.3: Geometry of the structure and coordinates defining the observation point.

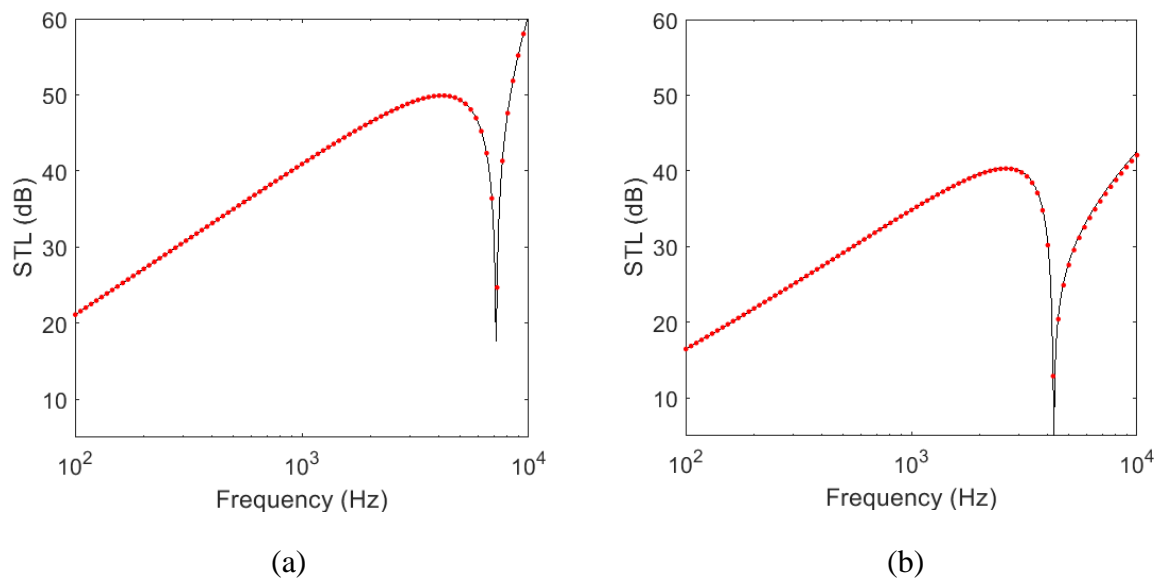


Figure 2.4: Sound transmission loss for a thin beam, air-to-air, dotted red: analytical [7]; solid black: numerical (WFE), (a) angle of incidence $\theta = 50^\circ$; (b) diffuse incident field.

TABLE 2.1: Material property of panels and fluids

Case1: isotropic panel (steel)	
$E = 2 \times 10^{11} \text{ Pa}$, $\rho = 7800 \text{ kg/m}^3$, $h = 3 \text{ mm}$, $\nu = 0.2$, $\eta = 0$	
Case 2: antisymmetric panel (isotropic core)	
graphite-epoxy skins:	foam core:
$E_x = 1.19 \times 10^9 \text{ Pa}$, $E_y = 8.67 \times 10^9 \text{ Pa}$, $E_z = 8.67 \times 10^9 \text{ Pa}$,	$E_x = 1.8 \times 10^8 \text{ Pa}$,
$G_{yz} = 3.9 \times 10^9 \text{ Pa}$, $G_{xy} = 5.8 \times 10^9 \text{ Pa}$, $G_{xz} = 5.18 \times 10^9 \text{ Pa}$,	$\nu = 0.286$
$\nu_{xy} = 0.3$, $\nu_{yz} = 0.02$, $\nu_{xz} = 0.31$, $\rho = 1389 \text{ kg/m}^3$, $\eta = 0.01$	$\rho = 110 \text{ kg/m}^3$, $\eta = 0.03$
Case 3: symmetric panel (orthotropic core)	
styrofoam core:	face sheets
$E_x = 8.3 \times 10^9 \text{ Pa}$, $E_y = 8.3 \times 10^9 \text{ Pa}$, $E_z = 8.3 \times 10^9 \text{ Pa}$,	$E_x = 4.9 \times 10^9 \text{ Pa}$,
$G_{yz} = 3.1 \times 10^9 \text{ Pa}$, $G_{xy} = 3.1 \times 10^9 \text{ Pa}$, $G_{xz} = 3.1 \times 10^9 \text{ Pa}$,	$\nu = 0.15$
$\nu_{xy} = 0.34$, $\nu_{yz} = 0$, $\nu_{xz} = 0.34$, $\rho = 160 \text{ kg/m}^3$, $\eta = 0.03$	$\rho = 1600 \text{ kg/m}^3$, $\eta = 0.01$
air:	water:
$\rho = 1.21 \text{ kg/m}^3$	$\rho = 1000 \text{ kg/m}^3$
$\nu = 340 \text{ m/s}$	$\nu = 1500 \text{ m/s}$

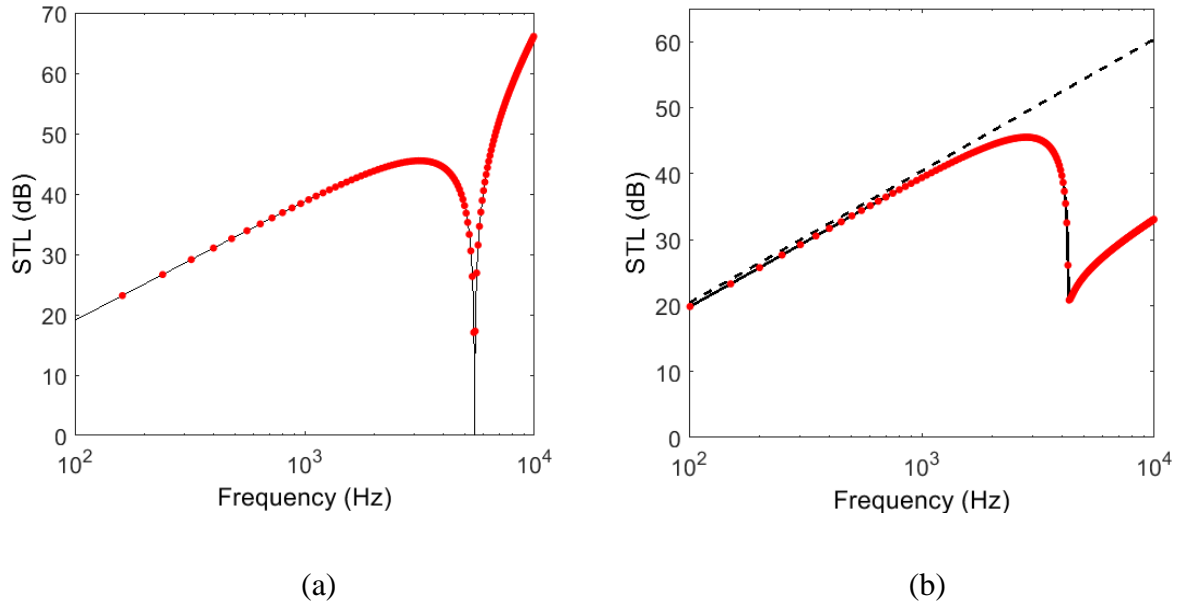


Figure 2.5: Sound transmission loss for the isotropic plate, air to air; (a) angle of incidence $\theta = 60^\circ$; (b) diffuse incident field, dot: analytical solution, solid line: WFE results, dash line: mass law.

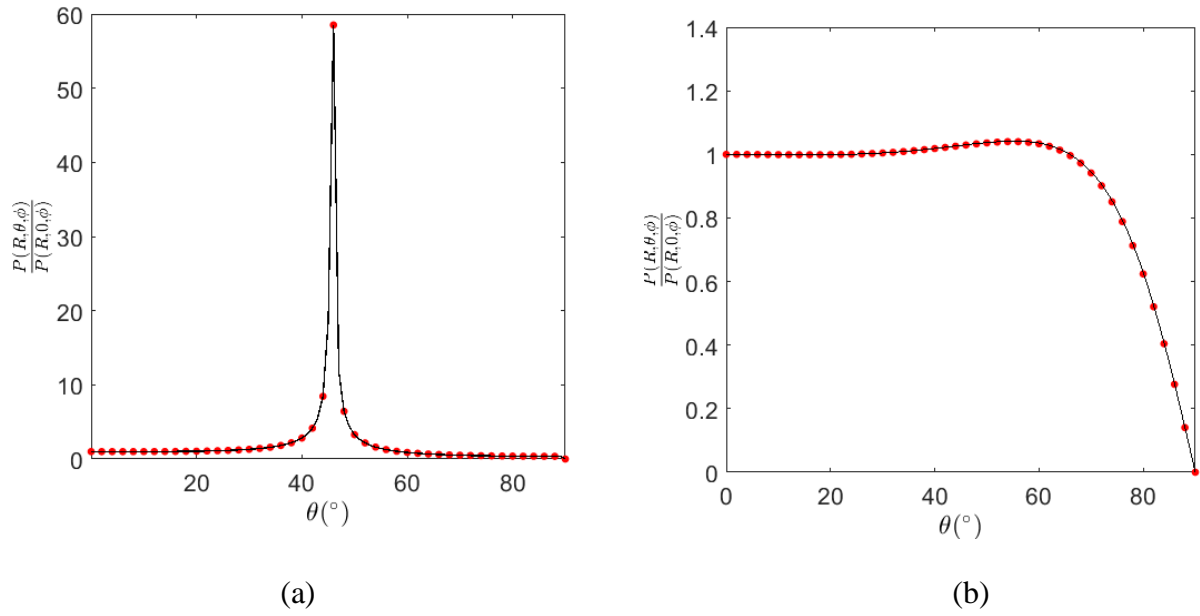


Figure 2.6: Radiated sound pressure in the far field; (a) air occupies the space $z > 0$, 8kHz; (b) water occupies the space $z > 0$, 40 kHz, dot: analytical solution, Solid line: WFE result.

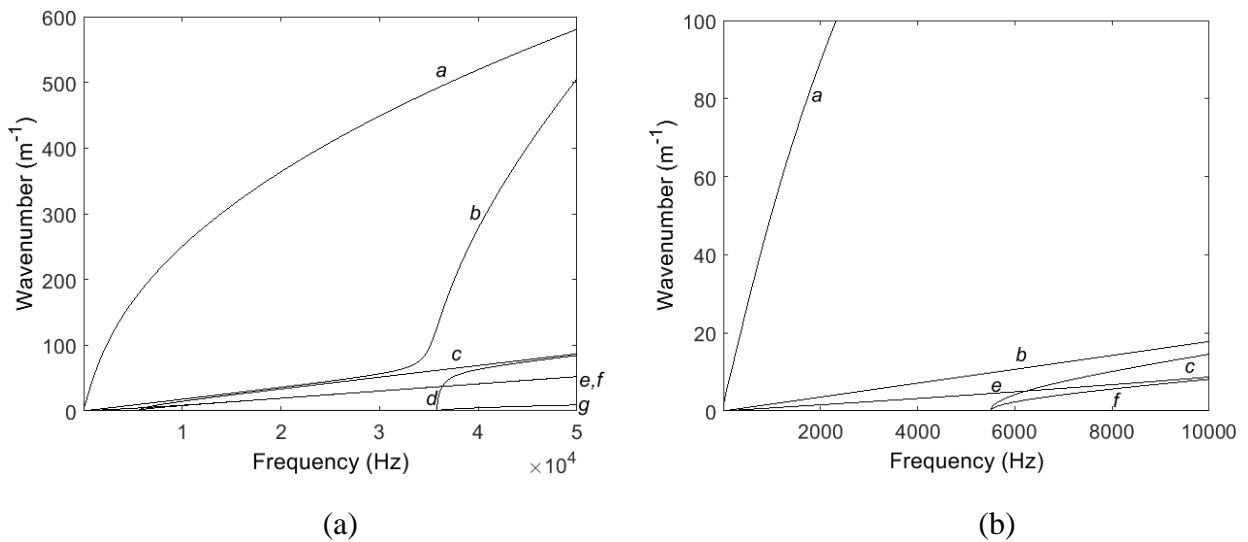


Figure 2.7: Dispersion curves of the sandwich panel: (a) real-valued wavenumbers; (b) the detailed wavenumber behavior around the first cut-off frequency.

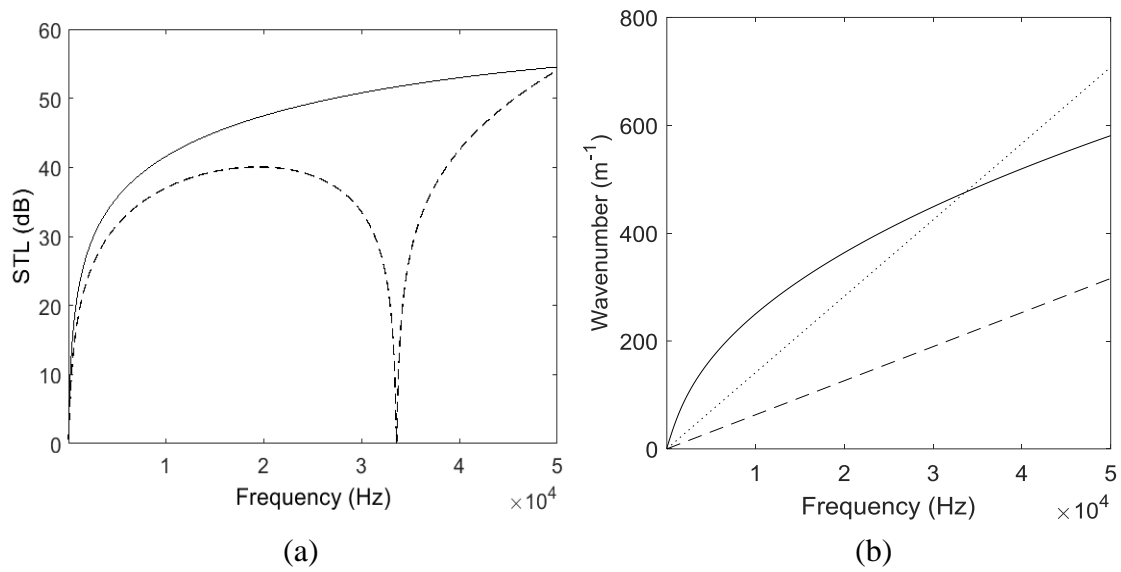


Figure 2.8: (a) sound transmission loss, air to air: — angle of incidence $\theta = 20^\circ$; - - - - angle of incidence $\theta = 50^\circ$; (b) wavenumbers: trace wavenumber component of acoustic plane wave ($\theta = 50^\circ$); - - - - trace wavenumber component of acoustic plane wave ($\theta = 20^\circ$); — structural bending wavenumber.

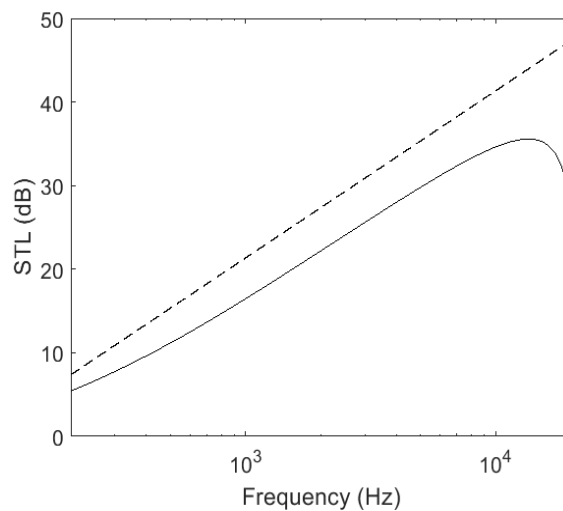


Figure 2.9: Sound transmission loss for diffuse incident field, air to air: - - - - - mass law; — using the WFE method.

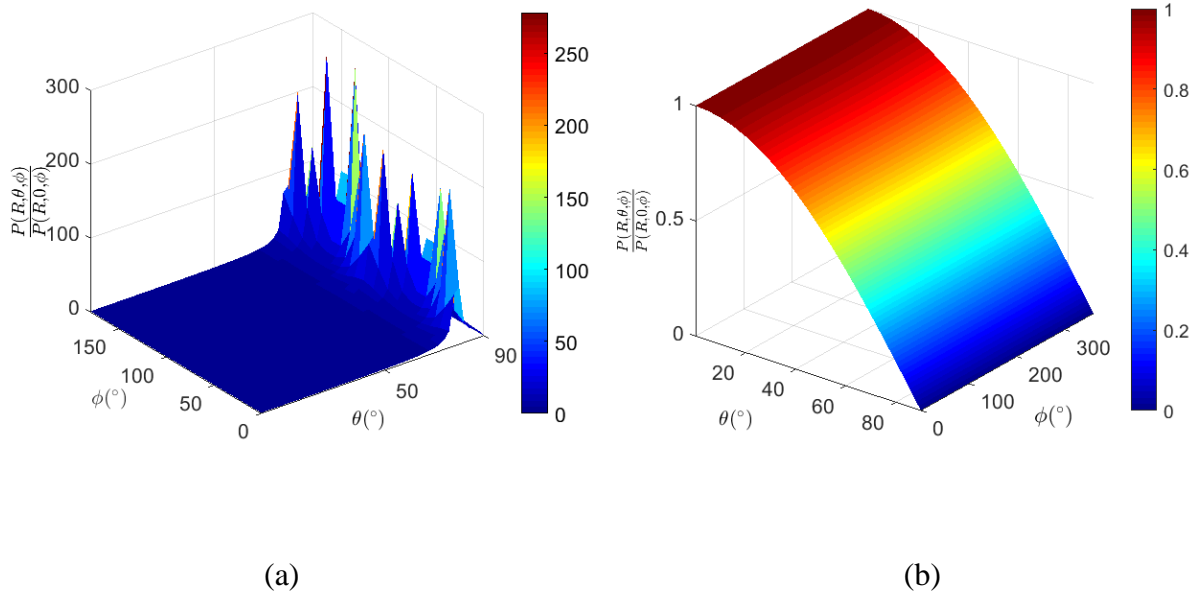


Figure 2.10: Radiated sound pressure from the sandwich panel; (a) air occupies the space $z \geq 0$; (b) water occupies the space $z \geq 0$.

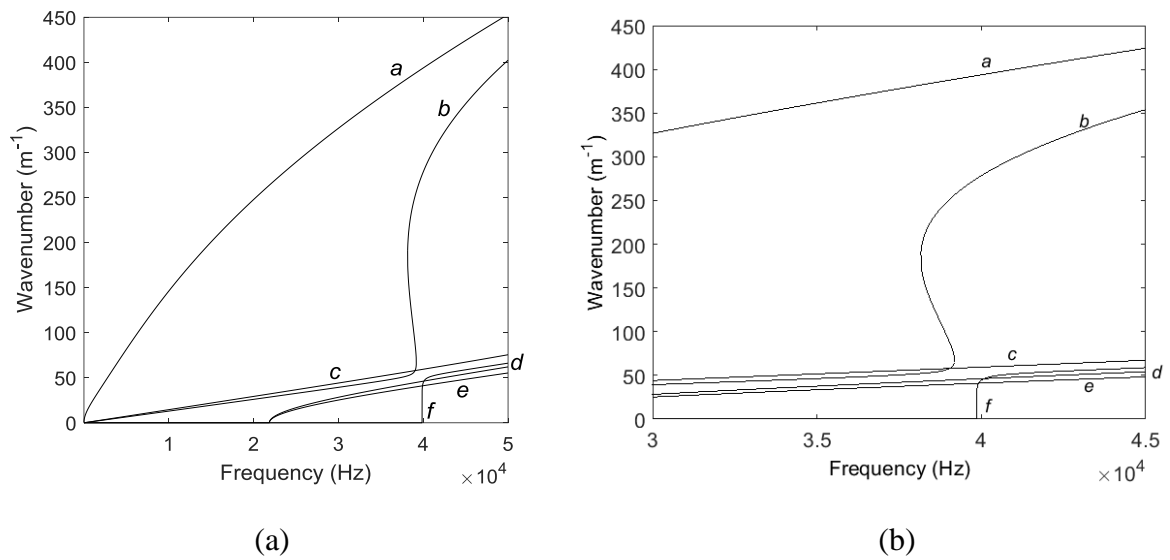


Figure 2.11: Dispersion curves of the sandwich panel; (a) propagating waves; (b) the detailed behaviour of high order waves at around 3.9 kHz.

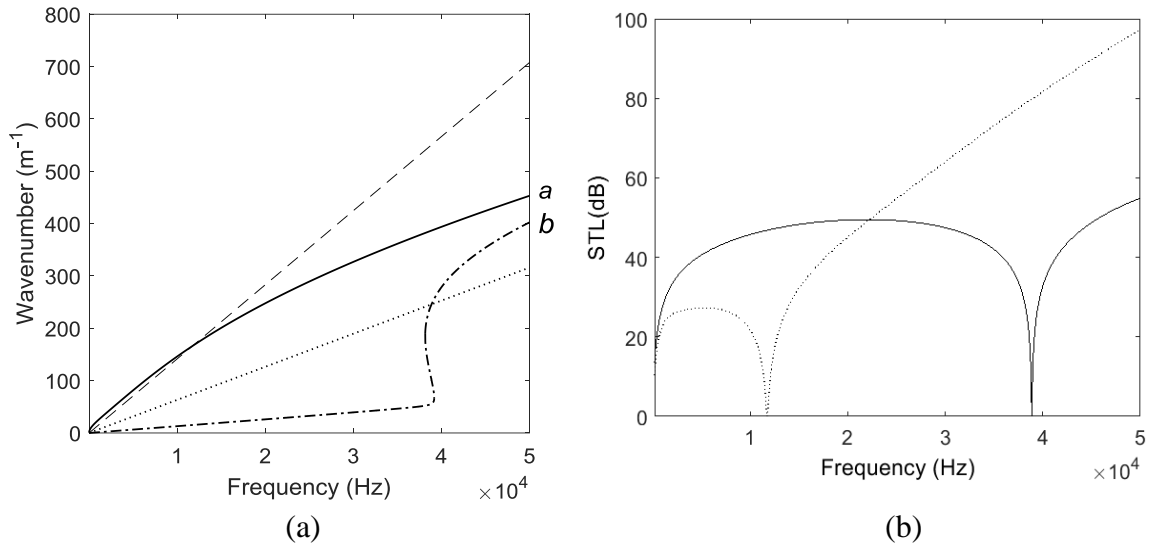


Figure 2.12: (a) Wavenumber: ----- trace wavenumber component of acoustic plane wave ($\theta = 50^\circ$); trace wavenumber component of acoustic plane wave ($\theta = 20^\circ$); _____ and _____ structural wavenumbers. (b) Transmission loss, air to air: angle of incidence $\theta = 50^\circ$; _____ angle of incidence $\theta = 20^\circ$.

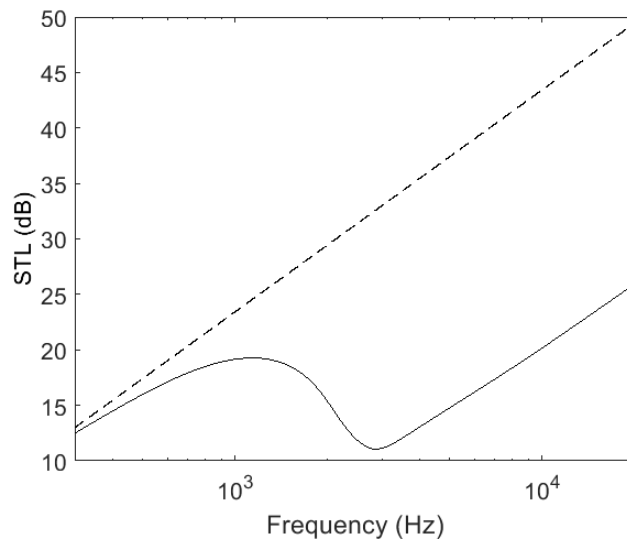
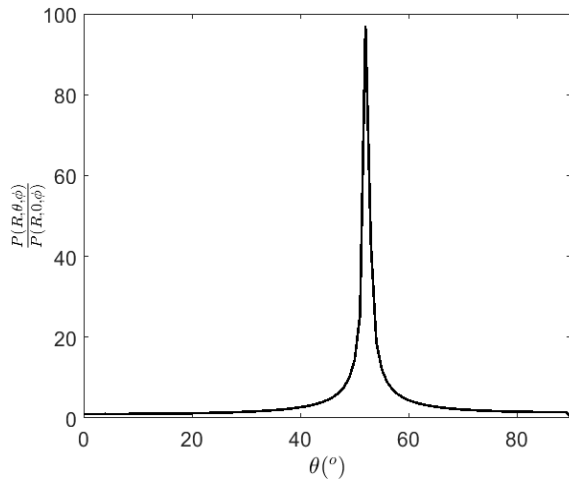
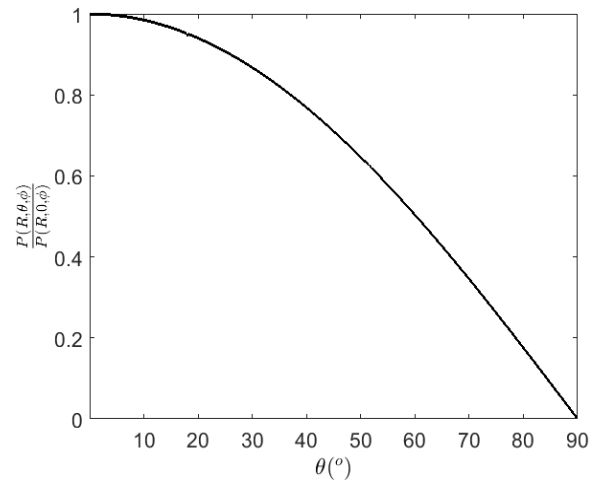


Figure 2.13: Sound transmission loss: air to air, diffuse incident field: ----- mass law.



(a)



(b)

Figure 2.14: Sound pressure radiated from the sandwich panel: (a) air occupies the space $z \geq 0$; (b) water occupies the space $z \geq 0$.

Chapter 3

SOUND TRANSMISSION THROUGH MULTI-LAYER FINITE PANELS

This chapter concerns sound transmission through finite, multi-layered panels such as double glazing, laminated panels. The method extends that described in section 2 for infinite panels in two ways: first, the structure consists of various fluid and solid layers which are modelled, assembled and the internal DOFs condensed. Secondly, the finite extent is taken into account by using a spatial windowing technique. Various simply-supported rectangular panels are considered. The predicted results are compared with measurements.

3.1 Introduction

Multi-layered, lightweight panels (double gypsum board walls, double glazing, etc.) are widely used in various engineering applications, e.g. architectural acoustics, automotive, aircraft, buildings, etc. However, due to the low mass, such structures typically have poor acoustic performance. Much research has been conducted to predict and improve the sound transmission loss (STL).

Various analytical models (e.g., a room-plate-air cavity coupled model) have been developed for calculating the STL as reviewed in chapter 1 (e.g., references [14, 15, 81, 87, 96]). Other techniques include a transfer matrix method (TMM) (e.g., references [77-79, 82, 86, 87]), based on a wave approach, finite element (FE) and/or boundary element methods [90, 91], spectral finite element method [96] and statistical energy analysis (SEA) [98]. In most

cases, the transfer matrix method is used to calculate sound transmission through a partition. Due to the assumption of infinite size, however, significant discrepancies can be observed at lower frequencies [82, 86].

Much effort has been made to reduce these discrepancies (e.g., limiting the maximum angle of incidence of the acoustic field incident on the structure [81] to account for the non-diffuseness of the incident field, and introducing various geometrical corrections [71, 79, 80, 82, 85, 86]). Structural resonances at lower frequencies are, however, commonly neglected. The geometrical correction is made by applying a spatial window to the incident and transmitted plane waves.

Although the transfer matrix method has proven to be an efficient tool for estimating acoustic properties (e.g., radiation efficiency, STL and sound absorption coefficient), deriving the transfer matrices from analytical equations involves lengthy algebraic manipulations for other than thin, isotropic elastic layers (e.g., CFRP, orthotropic layers, honeycombs, etc.). Therefore numerical methods become valuable, e.g. using the SEA. An alternative approach for such complicated constructions is the wave and finite element (WFE) method [111, 113, 141].

In this chapter, the method developed in Chapter 2 is extended to study the characteristics of sound transmission through finite panels. The finite structure can be made up of various layers with different materials (e.g., air, foam, steel, glass, etc.). For each solid layer, the WFE method is used to obtain the spectral dynamic stiffness matrix (DSM) following the lines described in Chapter 2. Fluid layers are modelled using wave methods. The infinite fluid half-spaces are modelled as in section 2.2.3 of Chapter 2. The analytical modelling approach for a finite fluid layer makes the model size independent of the layer thickness, which contributes to reducing the size of the WFE model of the assembled system. By assembling the structural

dynamic stiffness matrices with those of fluid layers, which are derived analytically, a total spectral DSM is found and used to calculate the response to incident acoustic waves. To take into account the effect of the finite size of a structure, a spatial windowing technique (reviewed in section 1.2.1) is applied. Various numerical examples are presented to validate this method. For simple finite structures, analytical methods are available for comparison. For complicated structures, using analytical methods is difficult, and the proposed method becomes valuable. Results are compared with measurements.

3.2 Theory and Formulation

In section 3.2.1, an infinite multi-layered structure coupled to fluids is considered. The spectral dynamic stiffness matrices of the fluid layers are derived in section 3.2.2 while the spectral dynamic stiffness matrices of the solid layers are derived in section 3.2.3. Then these matrices are assembled in section 3.2.4 to form the total spectral dynamic stiffness matrix of the system for calculating the response to acoustic excitation. The STL for directional or diffuse incident fields is defined in section 3.2.5. To account for the finite dimensions of the structure in practice, the spatial windowing technique [82] for rectangular panels is introduced in section 3.2.6.

3.2.1 Fluid-Structure Interaction

Consider an infinite, multi-layered structure with solid and fluid layers whose cross-section is shown in figure 3.1. The structure is made up of n layers lying parallel to the x - y plane which separates the space into two half-spaces. The upper semi-infinite half-space is occupied by a fluid layer and is denoted by layer number $j=0$. The lower half-space is occupied by another semi-infinite fluid (layer number $j=n+1$). Each solid layer is homogeneous in both x and y directions, but the properties may vary through the thickness in the z -direction in an arbitrary manner. The z -coordinate of the faces of layer j is denoted by z_j .

Assume that a time-harmonic oblique plane wave (similar to equation (2.14)) in the 0-th fluid layer, i.e. the upper half-space, is incident at an angle θ to the normal of the structure. The wavenumber components $(k_x, k_y, k_{z,0})$ of the incident wave meet the same relationships as described in equation (2.16). The structural motion excites reflected waves (see equation (2.15)) in the upper half-space. If layer j is a fluid layer, then waves

$$P_+^j e^{-ik_x x - ik_y y + ik_{z,j} z}, \quad P_-^j e^{-ik_x x - ik_y y - ik_{z,j} z}, \quad (3.1)$$

are excited, where P_+^j and P_-^j are the amplitudes of acoustic waves propagating in the negative and positive z -directions respectively; $k_{z,j}$ is defined in a similar manner to $k_{z,0}$ (see equation (2.17)). These in turn excite the n th solid layer which radiates sound waves (see equation 2.15) into the lower half-space.

3.2.2 Spectral Dynamic Stiffness Matrices of the Fluid Layers

Assume layer j is a fluid layer. The spectral dynamic stiffness matrix is derived analytically in this section.

The total acoustic pressures at the surfaces of the j -th layer can be written as

$$\begin{aligned} p_1^j &= P_+^j e^{ik_{z,j} z_j} + P_-^j e^{-ik_{z,j} z_j} \\ p_2^j &= P_+^j e^{ik_{z,j} z_{j+1}} + P_-^j e^{-ik_{z,j} z_{j+1}}, \end{aligned} \quad 1 \leq j \leq n, \quad (3.2)$$

where subscripts “1” and “2” relate to the upper and lower surfaces. The spatial dependence $\exp(-ik_x x - ik_y y)$ has been suppressed for simplicity. The normal velocity of the fluid in the z -direction at the fluid-solid interface is such that

$$\frac{\partial p_{1,2}^j(z_j)}{\partial z} = \rho_j \omega^2 w_{1,2}^j(z_j), \quad (3.3)$$

where the upper and lower normal displacements of the j -th layer are represented by w_1^j and w_2^j respectively. Inserting Eq. (3.2) into Eq. (3.3) yields,

$$\begin{aligned} P_+^j e^{ik_{z,j}z_j} - P_-^j e^{-ik_{z,j}z_j} &= D_{f,j} w_1^j, \\ P_+^j e^{ik_{z,j}(z_j-d)} - P_-^j e^{-ik_{z,j}(z_j-d)} &= D_{f,j} w_2^j, \end{aligned} \quad (3.4)$$

where $d = |z_j - z_{j+1}|$ and

$$D_{f,j} = -\frac{i\rho_j \omega^2}{k_{z,j}} \quad (3.5)$$

is the spectral dynamic stiffness of the j -th fluid layer. Combining Eq. (3.4) and Eq. (3.2) gives

$$\begin{bmatrix} P_1^j \\ P_2^j \end{bmatrix} = \bar{\mathbf{D}}^j(\omega, k_x, k_y) \begin{bmatrix} w_1^j \\ w_2^j \end{bmatrix}, \quad (3.6)$$

where

$$\bar{\mathbf{D}}^j(\omega, k_x, k_y) = \frac{iD_{f,j}}{\sin(k_{z,j}d)} \begin{bmatrix} -\cos(k_{z,j}d) & 1 \\ -1 & \cos(k_{z,j}d) \end{bmatrix} \quad (3.7)$$

is the spectral dynamic stiffness matrix of the j -th fluid layer of thickness d . For a given frequency and fluid properties, this matrix is only dependent on the thickness of the fluid layer.

The matrix size does not increase with the layer thickness d .

3.2.3 Spectral Dynamic Stiffness Matrices of the Solid Layers

Now suppose that layer j is a solid layer. The spectral dynamic stiffness matrix is found in this section from a wave and finite element analysis. A small rectangular segment of sides $L_x \times L_y$ of the j -th solid layer is taken as shown in figure 2.1(a). As mentioned in section 1.4, ANSYS SOLID185 elements were used to mesh the segment. Figure 2.1(b) indicates the vertical view of the FE mesh of the segment. For convenience, only one ANSYS SOLID185 element is used

in the x - and y - directions, but there can be any number of edge and internal nodes in the FE model of the segment. As is normal in FE analysis, the element size should not be too small or too large compared to the shortest structural and acoustic wavelengths. Otherwise, the discretised model will not accurately describe the structural motion.

According to equation (2.22) and equation (2.23), the vector of the external nodal forces for the j -th solid layer can be written as

$$\mathbf{e}^j = \left[\left(\mathbf{e}_1^j \right)^T \quad \left(\mathbf{e}_2^j \right)^T \quad \left(\mathbf{e}_3^j \right)^T \quad \left(\mathbf{e}_4^j \right)^T \right]^T, \quad (3.8)$$

where the superscript j represents the j -th layer, and

$$\mathbf{e}_s^j = p_1^j \alpha_s^j \mathbf{u}_1^j - p_2^j \alpha_s^j \mathbf{u}_2^j, \quad (3.9)$$

where the coefficient α_s^j can be calculated by equation (2.24), the subscript s denotes the s -th corner of the segment, and the definition of $\mathbf{u}_{1,2}^j$ is same as $\mathbf{u}_{1,2}$ in equation (2.22). Similar to equation (2.34), the discrete equation of motion for the j -th solid layer can be written as

$$\mathbf{D}^j \mathbf{q}_1^j = \mathbf{e}_1^j + \lambda_x^{-1} \mathbf{e}_2^j + \lambda_y^{-1} \mathbf{e}_3^j + \lambda_x^{-1} \lambda_y^{-1} \mathbf{e}_4^j, \quad (3.10)$$

where λ_x^j and λ_y^j are wave propagation constants, and can be found from equation (2.31), \mathbf{D}^j is the dynamic stiffness matrix of the j -th layer, and can be expressed as

$$\mathbf{D}^j = \Lambda_L^j \left[\mathbf{K}^j - \omega^2 \mathbf{M}^j \right] \Lambda_R^j, \quad (3.11)$$

where \mathbf{D}^j , Λ_L^j and Λ_R^j can be found from equation (2.13), equation (2.32) and equation (2.33) respectively. Substituting Eq. (3.9) into Eq. (3.10) leads to

$$\mathbf{D}^j \mathbf{q}_1^j = \varepsilon^j \left(p_1^j \mathbf{u}_1^j - p_2^j \mathbf{u}_2^j \right), \quad (3.12)$$

where ε^j can be calculated by equation (2.38).

All the DOFs of layer j apart from the normal displacements at the surfaces are now condensed. Substituting Eq. (3.12) into Eq. (2.22) gives

$$\begin{bmatrix} p_1^j \\ p_2^j \end{bmatrix} = \bar{\mathbf{D}}^j(\omega, k_x, k_y) \begin{bmatrix} w_1^j \\ w_2^j \end{bmatrix}, \quad (3.13)$$

where

$$\bar{\mathbf{D}}^j(\omega, k_x, k_y) = \begin{bmatrix} \boldsymbol{\varepsilon}^j(\mathbf{u}_1^j)^\top (\mathbf{D}^j)^{-1} \mathbf{u}_1^j & -\boldsymbol{\varepsilon}^j(\mathbf{u}_1^j)^\top (\mathbf{D}^j)^{-1} \mathbf{u}_2^j \\ \boldsymbol{\varepsilon}^j(\mathbf{u}_2^j)^\top (\mathbf{D}^j)^{-1} \mathbf{u}_1^j & -\boldsymbol{\varepsilon}^j(\mathbf{u}_2^j)^\top (\mathbf{D}^j)^{-1} \mathbf{u}_2^j \end{bmatrix}^{-1} \quad (3.14)$$

is the reduced spectral dynamic stiffness matrix of the j -th solid layer, relating the pressures and displacements of the surfaces of the layer.

3.2.4 Assembly of the Spectral Dynamic Stiffness Matrices

The spectral dynamic stiffness matrices of the solid and fluid layers are assembled in this section using the continuity and equilibrium conditions between the layers.

The equation of motion of the multi-layered system can be written in terms of the surface displacements and pressures as

$$\mathbf{D}(\omega, k_x, k_y) \mathbf{q} = \mathbf{p}, \quad (3.15)$$

where the displacement and pressure vectors are defined as

$$\begin{aligned} \mathbf{q} &= \begin{bmatrix} w_1^1 & w_2^1 & \cdots & w_1^j & w_2^j & \cdots & w_1^n & w_2^n \end{bmatrix}^\top, \\ \mathbf{p} &= \begin{bmatrix} p_1^1 & p_2^1 & \cdots & p_1^j & p_2^j & \cdots & p_1^n & p_2^n \end{bmatrix}^\top, \end{aligned} \quad (3.16)$$

and the assembled dynamic stiffness matrix is

$$\mathbf{D}(\omega, k_x, k_y) = \begin{bmatrix} \bar{\mathbf{D}}_1 & \mathbf{0} & \mathbf{0} & \mathbf{0} & \mathbf{0} \\ \mathbf{0} & \ddots & \mathbf{0} & \mathbf{0} & \mathbf{0} \\ \mathbf{0} & \mathbf{0} & \bar{\mathbf{D}}_j & \mathbf{0} & \mathbf{0} \\ \mathbf{0} & \mathbf{0} & \mathbf{0} & \ddots & \mathbf{0} \\ \mathbf{0} & \mathbf{0} & \mathbf{0} & \mathbf{0} & \bar{\mathbf{D}}_n \end{bmatrix}, \quad (3.17)$$

where $\bar{\mathbf{D}}_j$ represents the spectral dynamic stiffness matrix of the j -th layer.

Now the internal surface displacements are condensed. At the interfaces between the various layers, displacement continuity and equilibrium lead to

$$w_2^{(j)} = w_1^{(j+1)}, \quad p_2^{(j)} + p_1^{(j+1)} = 0. \quad (3.18)$$

Therefore

$$\mathbf{q} = \mathbf{\Phi} \begin{bmatrix} \mathbf{q}_b \\ \mathbf{q}_i \end{bmatrix}, \quad \mathbf{\Phi} = \begin{bmatrix} 1 & 0 & 0 & 0 & 0 & \dots & 0 \\ 0 & 0 & 1 & 0 & 0 & \dots & 0 \\ 0 & 0 & 1 & 0 & 0 & \dots & 0 \\ 0 & 0 & 0 & 1 & 0 & \dots & 0 \\ \vdots & \vdots & \vdots & \vdots & \vdots & \dots & 0 \\ 0 & 1 & 0 & 0 & 0 & \dots & 0 \end{bmatrix}, \quad (3.19)$$

where $\mathbf{\Phi}$ is a reorganising matrix for the elements of \mathbf{q} , \mathbf{q}_b denotes the outer (or boundary) surface displacements, and \mathbf{q}_i represents the internal surface displacements and can be eliminated by dynamic condensation. They are defined as

$$\mathbf{q}_b = [w_1^1 \quad w_2^n]^T, \quad \mathbf{q}_i = [w_1^2 \quad w_1^3 \quad \dots \quad w_1^n]^T. \quad (3.20)$$

Equilibrium implies that

$$\mathbf{\Phi}^T \mathbf{p} = \begin{bmatrix} \mathbf{p}_b \\ \mathbf{0} \end{bmatrix}. \quad (3.21)$$

Substituting Eq. (3.19) into Eq. (3.15) and pre-multiplying by $\mathbf{\Phi}$ yields

$$\tilde{\mathbf{D}} \begin{bmatrix} \mathbf{q}_b \\ \mathbf{q}_i \end{bmatrix} = \begin{bmatrix} \mathbf{p}_b \\ \mathbf{0} \end{bmatrix}, \quad \tilde{\mathbf{D}} = \Phi^T \mathbf{D} \Phi = \begin{bmatrix} \tilde{\mathbf{D}}_{bb} & \tilde{\mathbf{D}}_{bi} \\ \tilde{\mathbf{D}}_{ib} & \tilde{\mathbf{D}}_{ii} \end{bmatrix}, \quad (3.22)$$

where $\tilde{\mathbf{D}}$ is the dynamic stiffness matrix of the assembled layers and

$$\mathbf{p}_b = \begin{bmatrix} p_1^1 & p_2^n \end{bmatrix}^T. \quad (3.23)$$

By dynamic condensation, Eq. (3.22) can finally be reduced to

$$\mathbf{D}_r \begin{bmatrix} w_1^1 \\ w_2^n \end{bmatrix} = \begin{bmatrix} p_1^1 \\ p_2^n \end{bmatrix}, \quad \mathbf{D}_r = \tilde{\mathbf{D}}_{bb} - \tilde{\mathbf{D}}_{bi} \tilde{\mathbf{D}}_{ii}^{-1} \tilde{\mathbf{D}}_{ib}. \quad (3.24)$$

Now, the multi-layered system has been reduced to an equivalent panel with 2 surface DOFs.

In equation (3.24), \mathbf{D}_r is the reduced spectral dynamic stiffness matrix of the structure.

The dynamic stiffnesses of the external fluids are now included by referring to Eqs. (2.20-2.21).

The following expressions can be found,

$$p_1^1 = 2P_0 - D_{f,0} w_1^1, \quad p_2^n = -D_{f,n+1} w_2^n \quad (3.25)$$

where P_0 is the complex amplitude of the incident plane wave, $D_{f,0}$ and $D_{f,n+1}$ are the dynamic stiffness of the semi-infinite fluid layers and are given in Eq.(3.5) . Substituting Eq. (3.25) into Eq. (3.24) gives

$$(\mathbf{D}_r + \mathbf{D}_\infty) \begin{bmatrix} w_1^1 \\ w_2^n \end{bmatrix} = \begin{bmatrix} 2P_0 \\ 0 \end{bmatrix}, \quad \mathbf{D}_\infty = \begin{bmatrix} D_{f,0} & 0 \\ 0 & D_{f,n+1} \end{bmatrix}. \quad (3.26)$$

Once the displacements of the outer surfaces of the structure are calculated from Eq. (3.26), the acoustic pressures follow from Eq. (3.25). Similarly, the internal layer surface displacements and pressures can be found from Eq. (3.22) and Eq. (3.6) if they are required.

In the above, the analytical models for the fluid layers were coupled to the FE models of the solid layers. An alternative method might be to mesh an entire segment of the structure by

FE, i.e., ANSYS FLUID30 elements are used to model the fluid layer. The analysis would then proceed along the lines described in Chapter 2. Note that the mass and stiffness matrices of the solid and fluid layers need to be assembled and this is not necessarily straightforward (e.g., solid and fluid layers are often displacement and potential (or pressure) formulations and assembly requires a coupling matrix). Furthermore, a number of elements might be needed for a fluid layer so that the size of the model and the computational cost increase. Hence, there are benefits in modelling the fluid layer analytically. A comparison of the two methods is presented in the examples below for a small FE model of a three-layer structure.

3.2.5 Sound Transmission Loss and Diffuse Incident Field

For an oblique sound wave incident on an infinite panel at a pair of angles (θ, ϕ) , the STL of the infinite single layer is defined in equation (2.42). For the infinite multilayer structure, the transmission coefficient τ_∞ is

$$\tau_\infty(\theta, \phi) = \frac{\operatorname{Re}\left\{\left(k_{z,n+1}/\rho_{n+1}\right)\left|P_t^2\right|\right\}}{\left(k_{z,0}/\rho_0\right)\left|P_i^2\right|}. \quad (3.27)$$

For a diffuse incident field, the transmission coefficient can be calculated using equation (2.43).

3.2.6 Windowing for Finite Size Panels

The diffuse-field transmission loss of an infinite panel differs significantly from that of a finite panel in a rigid baffle, especially at lower frequencies. There are two principal reasons: (i) the existence of structural resonances; (ii) diffraction by the aperture in the rigid baffle that contains the structure. To account for the second effect, the diffraction due to the finite size can be allowed for by applying a spatial windowing technique [82] to an infinite structure, assuming that the finite panel is rectangular. This method starts by calculating the radiated power Π_r from a rectangular portion (of sides a and b and area $S=ab$) of the infinite panel for

an incident wave with trace wavenumber $k_t = k_0 \sin \theta \cos \phi$. Then the transmission coefficient can be defined as [82]

$$\tau_{1_f}(\theta, \phi) = \frac{\Pi_f(k_t, \phi)}{I_{\infty_in} S}, \quad (3.28)$$

where I_{∞_in} denotes the intensity incident on the infinite panel. Similarly, by spatially windowing the sound incident field, a correction factor $\tau_{2_f}(\theta, \phi)$ is defined as [82]

$$\tau_{2_f}(\theta, \phi) = \frac{\Pi_{f'}(k_t, \phi)}{I_{\infty_in} S}, \quad (3.29)$$

where $\Pi_{f'}(k_t, \phi)$ represents the incident power on the finite sized window. After windowing both the incident field and the radiated field, the transmission coefficient can be found by [82]

$$\tau_f(\theta, \phi) = \tau_{2_f}(\theta, \phi) \tau_{1_f}(\theta, \phi) = \tau_\infty(\theta, \phi) [\sigma(k_t, \phi) \cos \theta]^2, \quad (3.30)$$

where the radiation efficiency is defined (from [82]) as

$$\begin{aligned} \sigma(k_t, \phi) = & \frac{S}{\pi^2} \int_0^{k_{n+1}} \int_0^{2\pi} \frac{1 - \cos(k_r \cos \psi - k_t \cos \phi) a}{[(k_r \cos \psi - k_t \cos \phi) a]^2} \frac{1 - \cos(k_r \sin \psi - k_t \cos \phi) b}{[(k_r \cos \psi - k_t \cos \phi) b]^2} \\ & \times \frac{k_{n+1} k_r}{\sqrt{k_{n+1}^2 - k_r^2}} d\psi dk_r. \end{aligned} \quad (3.31)$$

In the above analysis, windows for both the incident and radiated field pressure fields are used, as described in [82]. Some authors [86] suggest windowing only for the radiated field, so that equation (3.30) becomes

$$\tau_f(\theta, \phi) = \tau_\infty(\theta, \phi) \sigma(k_t, \phi) \cos \theta. \quad (3.32)$$

This in many cases gives better agreement with measurements.

3.2.7 Summary

In summary, the proposed approach involves the following steps:

- The dynamic stiffness matrices for the fluid layers are derived analytically.
- A WFE model for each solid layer is developed, the spectral dynamic stiffness matrices found and the DOFs other than transverse surface displacements condensed.
- The fluid and solid layers are assembled.
- The internal DOFs are condensed, leaving only the transverse displacements of the outer surfaces.
- The semi-infinite fluid layers are included using equation (3.26).
- By solving equation (3.26), the reflected and transmitted acoustic pressures can be found, and sound transmission loss for an infinite panel calculated.
- Finally, a windowing technique is applied for finite-sized panels.

3.3 Illustrative Examples

In this section various numerical examples are presented to illustrate the application of the WFE method to predict the STL of multi-layered structures. For simple structures (e.g., finite, rectangular thin plates), analytical methods are available for comparison. The analytical predictions for simple panels follow chapter 5 in Ref. [7] using analytical equations for the spectral dynamic stiffness matrices of the panels. The analytical results are compared with those of the WFE method. The WFE results are also compared to experimental data.

3.3.1 Single Layer Panel

Consider the case of an aluminium plate of sides $1.1\text{m} \times 1.4\text{m}$. The material properties in table 3.1 are taken from Ref. [82]. A small segment of the structure is taken and meshed by one ANSYS SOLID181 element of sides $L_x = L_y = 1\text{mm}$. Structural damping is considered by making the stiffness matrix complex. The STL is predicted analytically and numerically. It can be seen

from figure 3.2(a) that the agreement between the two methods is excellent. Figure 3.2(b) shows the predictions and measurements [82] in 1/3 octave frequency bands, where two ways of applying the spatial windowing technique were applied using equation (3.32) and equation (3.30). Both predictions show good agreement with the measurements, although structural resonances lead to discrepancies at low frequencies. Furthermore, the double-sided window seems to give better agreement with measurements in this case. Henceforth, unless otherwise stated, two-sided windowing is used for finite panels. The weighted sound reduction index for the frequency range of 100-3150Hz was also calculated. The measured sound reduction index is 24dB whereas both the WFE method and the analytical method give 23dB.

3.3.2 Three Layer Isotropic Panels

The second case considered is a double glazing panel of dimensions 1.48m × 1.23m. It consists of two identical panes of 4-mm thickness and a 12-mm thick air cavity. The material properties of the glass taken from Ref. [82] are shown in table 3.1. The STL of this structure is predicted by two WFE models. In model 1, four ANSYS SOLID185 elements of sides $L_x = L_y = 1\text{mm}$ are used to mesh each pane of a small segment of the structure and the fluid in the cavity is modelled by the analytical wave model. In model 2 the entire segment of the structure is meshed using twelve ANSYS FLUID30 elements and eight ANSYS SOLID185 elements.

Figure 3.3 shows the STL predicted by the two models for given angles of incidence, neglecting structural and acoustic damping. It can be seen that the agreement is very good. The STL dips occurring at 285 Hz, 380 Hz and 495 Hz are due to the mass-air-mass resonance. At higher frequencies, the coincidence effect leads to the notches in the curves at 4000 Hz and 6000 Hz.

The diffuse-field STL was predicted using the analytical and WFE methods. Figure 3.4(a) shows the results for the infinite double panel, whereas figure 3.4(b) shows the predictions for

a finite panel in 1/3 octave frequency bands, together with measurements from Ref. [82]. Again, the agreement between the analytical and WFE results is excellent in figure 3.4(a). Two dips can be observed at 250 Hz and 3150 Hz respectively due to the double wall resonance and the coincidence effect. In figure 3.4(b), the discrepancies occurring in the 300-3000 Hz range between the measurements and the predictions are due to the fact that the model assumes the fluid layers are infinite and no windowing is used. In the literature (e.g., Refs. [14, 81, 84, 88]), internal fluid damping is often taken into account for better agreement with measurements. In this chapter damping of 0.001 is used for the air cavity. The WFE method overestimates the STL above the coincidence frequency (3150 Hz) since flanking transmission at the edges of the structure is not considered. Again, structural resonances for the finite panel are the likely cause of discrepancies at low frequencies below the double wall resonance frequency (250 Hz). The measured weighted sound reduction index is 30 dB whereas both the WFE method and the analytical method give the same prediction of 29 dB.

Another three-layer panel considered here is a steel panel consisting of a pair of 2-mm thick steel panels and a 25-mm thick air cavity. The dimensions of the panel are 1.105 m \times 2.25 m. The material properties shown in table 3.1 are taken from Ref. [84]. A small segment of the three-layer panel is taken and meshed using two ANSYS SOLID185 elements of sides $L_x = L_y = 1$ mm. In figure 3.5, the predicted STL using the WFE method is seen to agree very well with that of the analytical method. There are two STL dips occurring at 160 Hz and 6300 Hz due to the double wall resonance and the coincidence effect, as observed in figure 3.4. The discrepancies between the measurements [82] and predictions are small. The weighted sound reduction index is 34 dB whereas both the WFE method and the analytical method predict 35 dB.

3.4 Application Examples

In this section, the WFE method is applied to complex structures for which using analytical methods is difficult, including two orthotropic laminated panels and a complex multilayer structure consisting of a honeycomb-cored layer, an air gap and a laminate layer.

3.4.1 Three Layer Orthotropic Panel

Consider a three-layer, symmetric, panel with composite Plywood skins and a thick Styrofoam core. The physical properties of the structure are taken from Ref. [14] and shown in table 3.2 (Skin 1 and Core 1). A small segment of the structure is modelled using ANSYS SOLID185 elements. Two elements of sides $L_x = L_y = 3\text{mm}$ are used to mesh each skin and 20 elements of the same size are used for the core. The diffuse-field STL is calculated using the WFE model. Two values of damping are taken for the core: the value (0.05) used in reference [17] and a larger value (0.09) which give better agreement with measurements at higher-frequencies.

The predicted result is plotted in figure 3.6(a) together with that of the discrete laminate model (DLM) in Ref. [17] and the measured results digitised from figure 2 in Ref. [14]. It can be seen that the WFE model accurately captures the dilatational resonance frequency at 1250 Hz and the coincidence frequency at 3200 Hz. The agreement between the DLM model and the WFE model is good below the coincidence frequency, with resonances of the finite structure leading to discrepancies at low frequencies. The discrepancies above the critical frequency between the three curves are likely due to damping. Note that the coincidence frequency around 3200Hz is not observed in the measurements but is apparent in the predictions because the amount of damping assumed is much less than in the real system. Increasing the level of damping in the core in the WFE model gives better agreement at high frequencies.

Another symmetric sandwich panel considered here has a thinner core of thickness 38.1mm. The physical properties of the structure are also taken from Ref. [14] and shown in table 3.2 (Skin2 and Core 2). Again, a small segment of sides $L_x = L_y = 3\text{mm}$ of the structure is modelled by ANSYS SOLID185 elements. Two elements are used for the skin and thirteen elements for the core. The predicted diffuse-field STL is shown in figure 3.6(b) along with the result estimated by the DLM model [17] and the measurements in Ref. [14]. The agreement between the two models is excellent below the critical frequency (2000 Hz). Again, structural resonances lead to discrepancies at low frequencies. The discrepancies between the three curves at frequencies around or greater than the coincidence frequency are due to assumed value of damping.

3.4.2 Complicated Multi-layered Panel

The multi-layered panel considered here represents a construction typical of an aircraft fuselage side wall. The upper panel is a Nomex honeycomb-cored structure sandwiched by carbon reinforced epoxy resin facings. The honeycomb core is, however, modelled as a continuum using data from reference [22]. (Chapter 4 extends the method to modelling of periodic structures at low frequencies). The lower panel consists of a layer of aluminium sheet and a Willtec foam layer. The two panels are separated by 12.7mm-thick airspace. For this structure, establishing analytical models using stress-displacement relations in an elastic solid is difficult. It is straightforward to use the WFE method. A small segment of the structure is taken. Twenty ANSYS SOLID185 elements of sides $L_x = L_y = 1\text{mm}$ were used to mesh the upper panel through the thickness whereas eleven ANSYS SOLID185 elements were used for the lower panel. The physical properties of the structure are taken from reference [136] and shown in table 3.3. The air properties are the same as listed in table 3.1.

The sound transmission loss for a given pair of incident angles (θ, ϕ) is shown in figure 3.7. It can be seen from figure 3.7(a) that the lowest mass-air-mass resonance frequency occurs

at 452 Hz for normal incidence, which is the same as the result calculated by Eq. (4.82) in Ref. [7]. The mass-air-mass resonance frequency increases with increasing angle of incidence for a given heading angle of the trace wave. There is a notch at 2600Hz for incident angle $\theta = 30^\circ$ due to coincidence.

Due to the orthotropic characteristics of the face sheets of the honeycomb panel, the bending stiffness of the structure varies with the direction of the trace wave. This can be seen from figure 3.7(b) where the coincidence frequency is seen to be dependent on the heading angle ϕ . Figure 3.8(a) shows the transmission coefficient as a function of heading angle ϕ . Because of symmetry, the range of ϕ in Eq. (44) can be reduced to $[0, \pi/2]$. Figure 3.8(b) shows the diffuse-field transmission loss curve. The mass-air-mass resonance leads to a dip around 650Hz.

3.5 Conclusions

In this chapter, a modelling approach based on the WFE method was described for predicting sound transmission through multi-layered panels with fluid layers. This approach starts with meshing a small segment of each solid layer of the structure using a conventional FE method to find the mass and stiffness matrices, which are then post-processed using periodicity and equilibrium conditions to obtain the spectral dynamic stiffness matrices, assuming the panels extend to infinity. Each fluid layer, including the two infinite half-spaces, is modelled analytically, the merit being that it is simpler to formulate and quicker to implement in software. The total spectral dynamic stiffness matrix of the system is formed by assembling the spectral dynamic stiffness matrices of the solid and fluid layers and the response of the infinite multi-layered panel to acoustic excitation determined.

To consider the effect of the finite size on the sound transmission loss, a geometrical correction was made by applying a spatial windowing technique to the infinite panel. A series

of numerical examples were presented to illustrate this method. These include an aluminium plate, three-layer isotropic panel constructions, orthotropic solid panels and a complicated composite panel with a fluid layer. For simple panels, the sound reduction indices were calculated and compare well with experimental measurements and those of existing analytical methods. For complex multi-layered structures, it is difficult to use analytical methods and hence the WFE method becomes valuable. The WFE method can give accurate and fast predictions at small computation cost.

The honeycomb-cored panel considered in this chapter was regarded as a uniform, homogeneous structure using data from a smoothed or homogenised model taken from the literature. This is of course an approximate model with approximate stiffness constants. In the next chapter, a wave and finite element based homogenised model will be developed for predicting the sound transmission loss of such periodic structure, when the periodic cell is small enough. This allows predictions to be made straightforwardly for structures such as honeycomb-cored panels without making various assumptions and approximations.

Figures

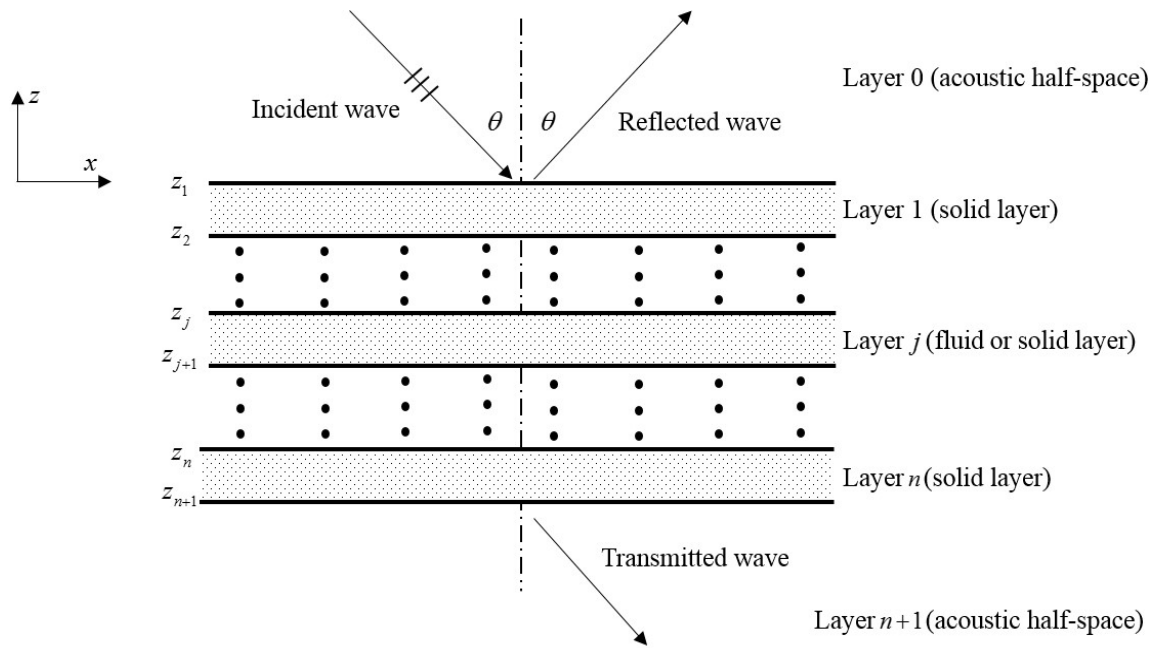


Figure 3.1: Coordinates and system definition for sound transmission through a multi-layered structure; the z -coordinate of the interface between layers j and $j+1$ is denoted by z_{j+1} .

Table 3.1: Material and air properties

	Aluminium	Glass	Steel	air
Young's modulus (Pa)	0.7×10^{11}	0.62×10^{11}	2×10^{11}	-
Density (kg/m^3)	2700	2500	7800	1.225
Poisson ratio	0.33	0.22	0.28	-
Loss factor	0.01	0.05	0.03	-
Sound speed (m/s)	-	-	-	340

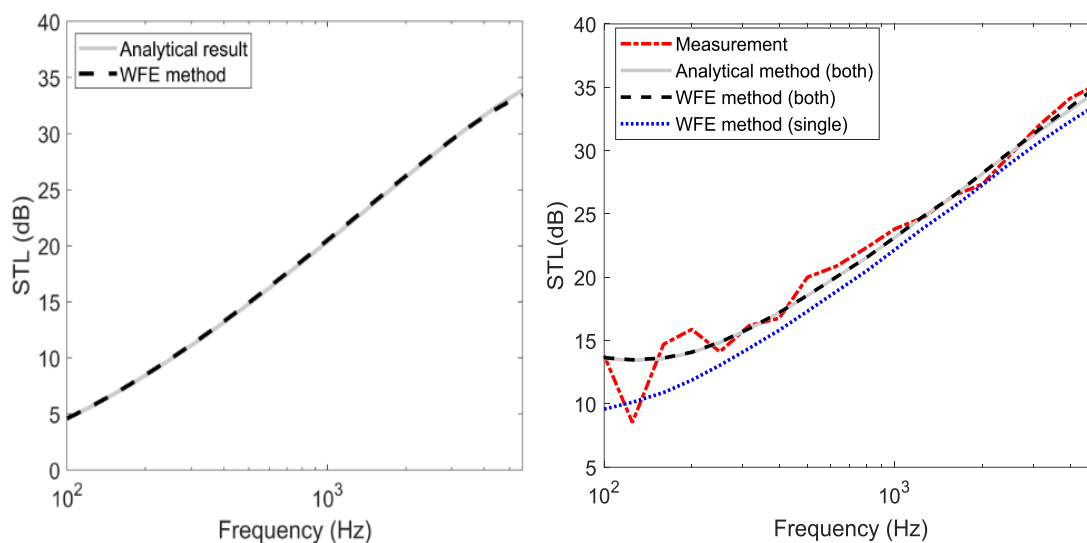


Figure 3.2: Comparison of diffuse field sound transmission loss for an aluminium plate: (a) discrete frequency, infinite panel; (b) 1/3 octave frequency bands, finite panel, measured values from reference [82], “-----“ and “——”: windowing both the incident and radiated fields, “.....” windowing only the radiated field.

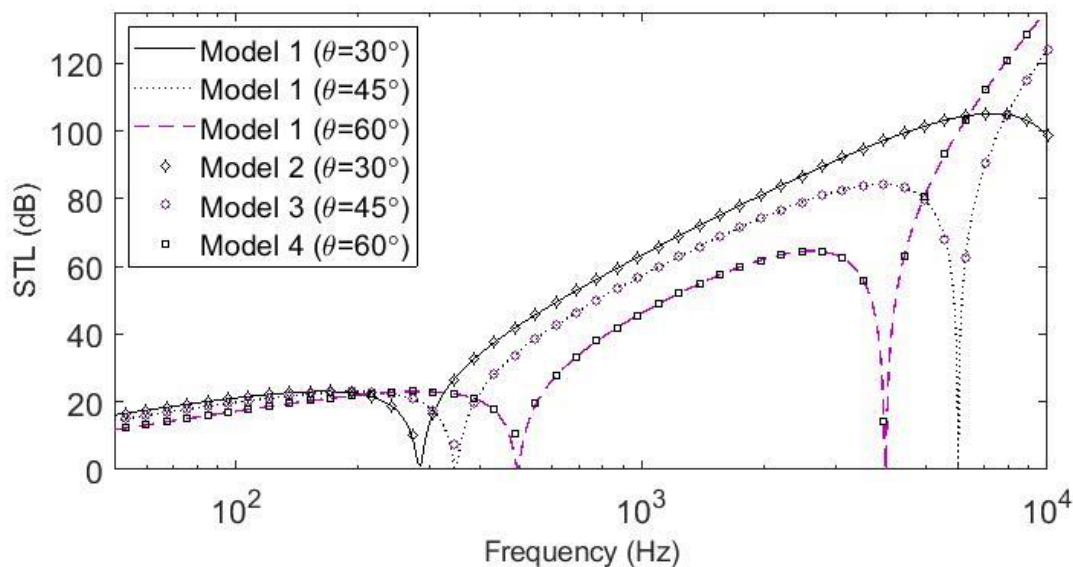


Figure 3.3: Comparison of sound transmission loss: model 1: using the analytical wave model; model 2: using a full FE model of the segment.

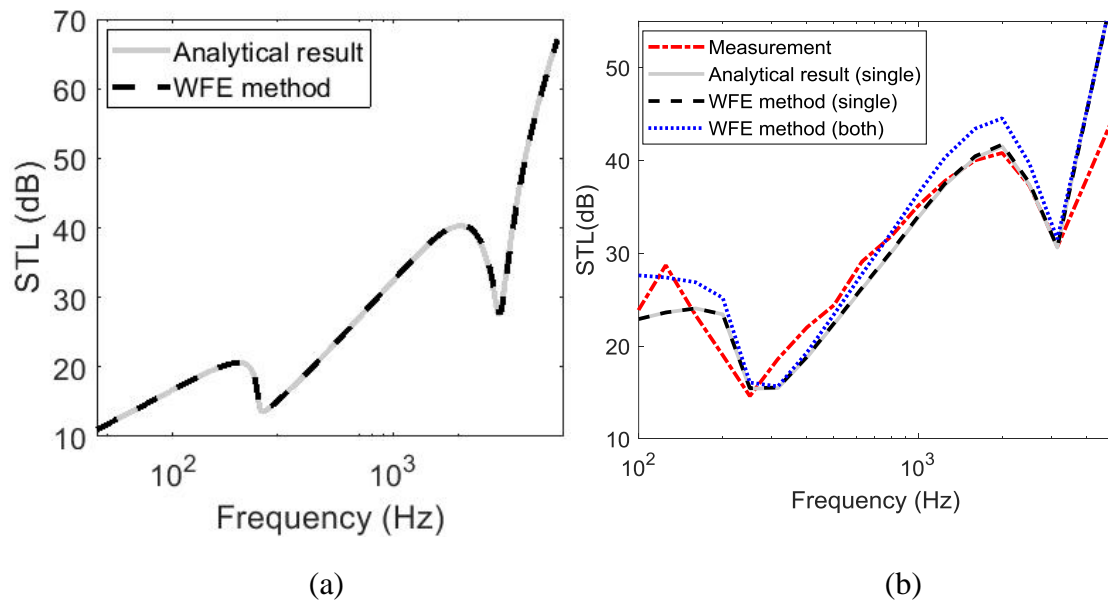


Figure 3.4: Diffuse field sound transmission loss for a three-layer glass panel: (a) discrete frequency, infinite panel; (b) 1/3 octave frequency bands, finite panel, measured values from reference [82], “-----“ and “———“: windowing only the radiated field, “.....” windowing both the incident and radiated fields.

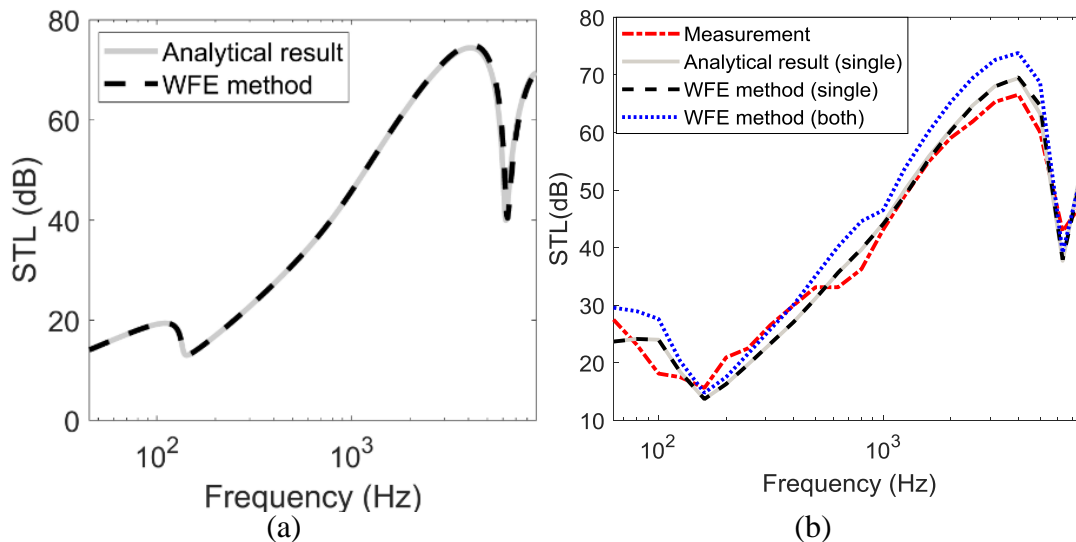


Figure 3.5: Comparison of sound transmission loss for a three layer steel panel: (a) discrete frequency, infinite panel; (b) 1/3 octave frequency bands, finite panel, measured values from reference [86], “-----“ and “———“: windowing only the radiated field, “.....” windowing both the incident and radiated fields.

Table 3.2: Physical properties of the three-layer orthotropic panels

	Young's modulus (Pa)	Shear modulus (Pa)	Poisson's ratio	Material density (kg/m ³)	Loss factor	Thickness (mm)
Skin 1	$E_x = E_y = 7 \times 10^9$, $E_z = 1.05 \times 10^6$	$G_{xy} = G_{xz} = G_{yz} =$ 2.7×10^9	$\nu_{xy} = \nu_{xz} =$ $\nu_{yz} = 0.3$	587.4	0.03	6.35
Core 1	$E_x = E_y = E_z =$ 8.3×10^6	$G_{xy} = G_{xz} = G_{yz} =$ 3.1×10^6	$\nu_{xy} = \nu_{xz} =$ $\nu_{yz} = 0.34$	16	0.05	76.2
Skin 2	$E_x = E_y = 7 \times 10^9$, $E_z = 1.29 \times 10^6$	$G_{xy} = G_{xz} = G_{yz} =$ 2.7×10^9	$\nu_{xy} = \nu_{xz} =$ $\nu_{yz} = 0.3$	587.4	0.03	6.35
Core 2	$E_x = E_y = E_z =$ 8.3×10^9	$G_{xy} = G_{xz} = G_{yz} =$ 3.1×10^6	$\nu_{xy} = \nu_{xz} =$ $\nu_{yz} = 0.34$	16	0.05	38.1

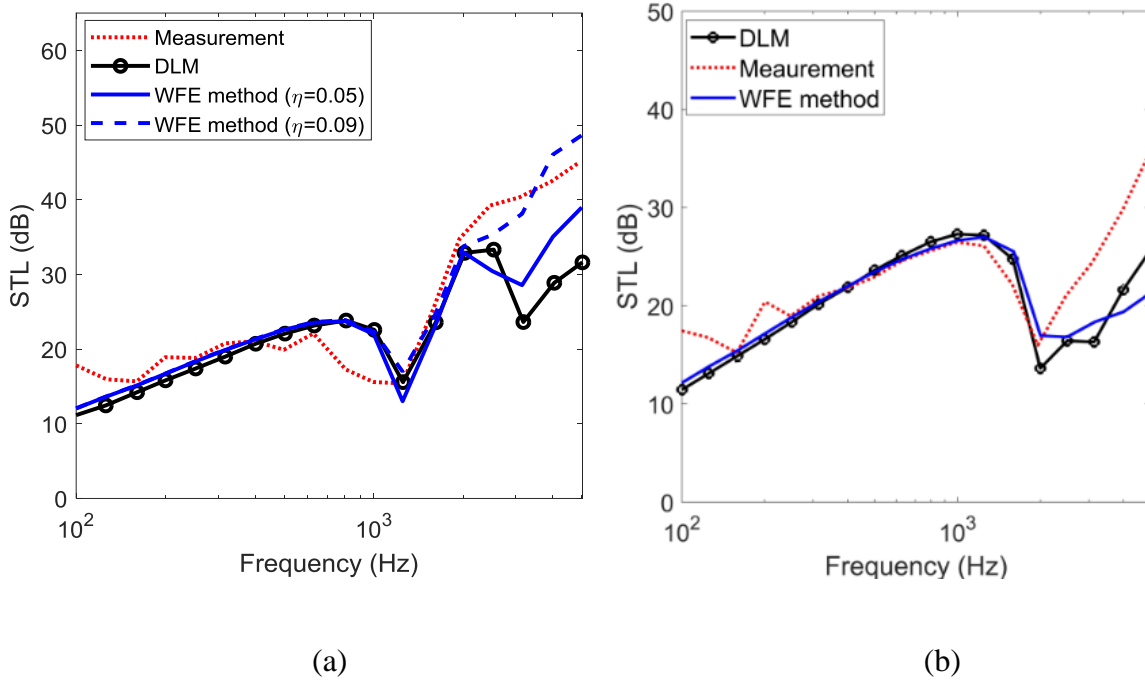


Figure 3.6: Comparison of sound transmission loss for composite panels with an orthotropic panel: (a) DLM model in reference [17], measurements digitalised from figure 3 in reference (skin 1, core1); (b) DLM model in reference, measurement result digitalised from figure 5 in reference [14] (skin 2, core 2).

Table 3.3: The physical properties of the complex multi-layered panel

	Honeycomb-cored panel		Laminate panel	
	Skin	Core	Skin	Foam
Thickness (mm)	1	19	0.5	25.4
Young's modulus E_x (Pa)	1.34×10^{11}	5.5×10^9	7×10^{10}	2.53×10^5
Young's modulus E_y (Pa)	7.7×10^9	5.5×10^9	7×10^{10}	2.53×10^5
Young's modulus E_z (Pa)	7.7×10^9	5.5×10^9	7×10^{10}	2.53×10^5
Shear modulus G_{xy} (Pa)	3.1×10^9	2.7×10^9	2.87×10^{10}	8.91×10^4
Shear modulus G_{xz} (Pa)	3.1×10^9	2.7×10^9	2.87×10^{10}	8.91×10^4
Shear modulus G_{yz} (Pa)	2.6×10^9	2.7×10^9	2.87×10^{10}	8.91×10^4
Poisson ratio ν_{xy}	0.29	0.33	0.22	0.42
Poisson ratio ν_{xz}	0.29	0.33	0.22	0.42
Poisson ratio ν_{yz}	0.49	0.33	0.22	0.42
Material density (kg/m^3)	1550	1240	2500	7.64
Loss factor	0.05	0.048	0.03	0.2

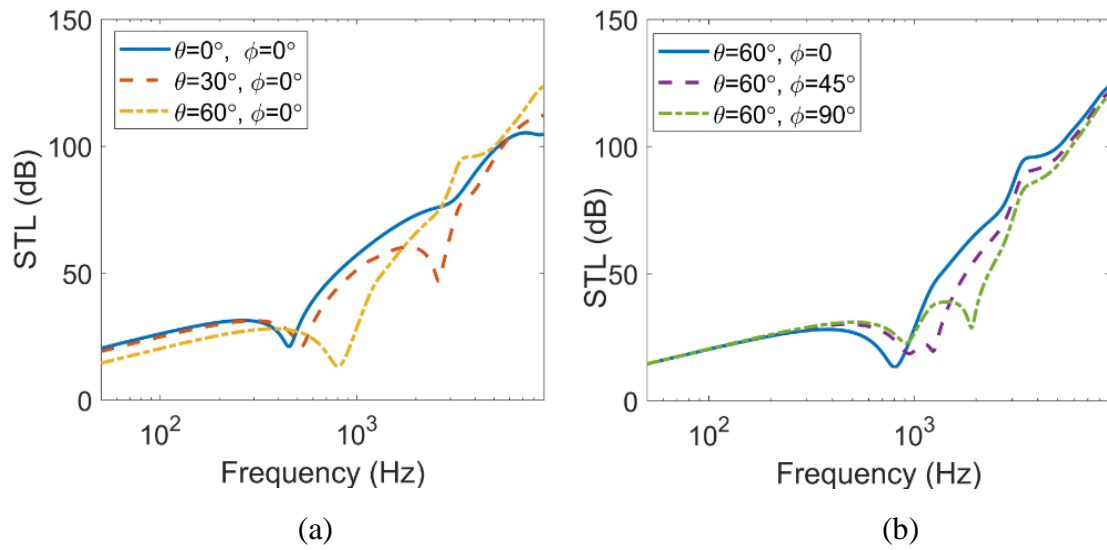


Figure 3.7: Sound transmission loss of multi-layer panels for incident plane waves: (a) heading angle ϕ given; (b) given elevation angle θ .

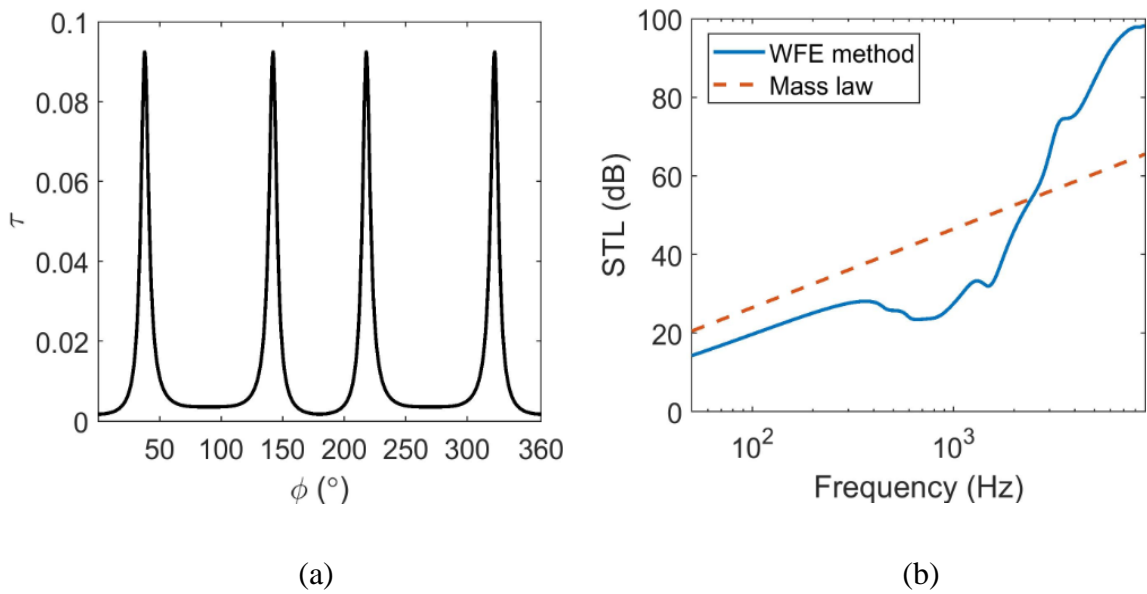


Figure 3.8: Transmission coefficient and diffuse-field STL of multi-layer panels: (a) transmission coefficient, at 1000Hz as a function of heading angle, ϕ ; (b) diffuse field transmission loss.

Chapter 4

SOUND TRANSMISSION THROUGH COMPOSITE HONEYCOMB PANELS

Chapters 2 and 3 concerned the vibroacoustics of structures that have uniform properties in the plane. This chapter concerns panels that are periodic, but with a periodic length that is small compared to any structural or acoustic wavelengths such that the bandgaps induced by the periodicity are not relevant and homogenised models are considered. The emphasis is placed on honeycomb cores.

A wave and finite element based homogenised model is developed in this chapter for predicting sound transmission through honeycomb-cored panels with arbitrary cores. The complexity of the core geometry can lead to a large FE model. Guyan reduction is used to reduce the model size.

4.1 Introduction

Since honeycomb-cored structures typically have high strength-to-weight ratio, they are widely used in various engineering applications, e.g., spacecraft, marine vessels and the walls of high-speed rail vehicles cars. However, they are prone to poor acoustic performance due to their low mass per unit area [7]. Various analytical approaches have been developed for investigating their vibroacoustic behaviour e.g. references [20, 27, 28, 53]. Typically, these methods model the honeycomb core as a uniform orthotropic material characterised by nine

independent stiffness constants [2, 14, 77], which are usually calculated using the equations developed by Gibson and Michael [22].

Several studies model the modal density of honeycomb sandwich panels by modelling the structure as a homogenised orthotropic plate with a vibroacoustic response which is almost identical to the actual sandwich structure at low frequencies. These models involve various assumptions. For example, in reference [23], the skin thickness of the structure is assumed to be very small compared to the core thickness so that the bending stiffness of the skin is neglected. Symmetric laminate skins and first-order shear deformation are assumed in reference [24].

These approximate models have other disadvantages. For example, they are often inaccurate at mid-to-high frequencies. Also, homogenisation becomes difficult for honeycomb-cored panels with irregular core structures e.g. a core structure with an irregular hexagonal core as the repeating cell. Therefore numerical methods become valuable for predicting the vibroacoustic response of the panel. Such methods include the FE method [90, 119], SEA [97] and the transfer matrix method [77, 79, 80].

An alternative method, described here, is the wave and finite element (WFE) method. This method has been developed [111, 113] and applied to predict the forced response of continuous [128-130] and periodic structures [30, 124, 131, 132]. This method starts with meshing a periodic cell of an entire structure. For complex structures (e.g. corrugated-cored panels, multi-layered systems, honeycomb-cored structures), the complicated geometry of the periodic cell leads to a large FE model, which increases the computational cost. Therefore, model reduction methods such as component mode synthesis (CMS) (see, for example, [29, 31, 98, 124, 131, 133]) can be used to reduce the internal DOFs of the cell. In references [128-130], the model size is reduced by representing the motion as a set of wave bases with different weights.

In this Chapter, a combination of the wave and finite element method and Guyan reduction is proposed to predict the sound transmission loss of honeycomb-cored panels without making any assumptions to reduce the complexity of the structure. Note that this chapter focuses on the low frequencies where the free structural and acoustic wavelengths are much larger than the dimensions of the cells. Using this method, a three-dimensional periodic cell of the structure is modelled using a conventional finite element method. Due to the complexity of the core geometry, a fine mesh is often needed for accurately modelling the geometry. The finite element model can contain a large number of internal nodes. For reducing the model size, Guyan reduction is used. Wave propagation in the fluids surrounding the structure is modelled analytically. The acoustic excitation is modelled using equivalent external nodal forces. Using the relatively small-sized mass and stiffness matrices, a fluid/structure coupled spectral dynamic stiffness matrix is derived to calculate the response to an incident acoustic wave. Excitation of the structure by oblique plane waves and a diffuse sound field are both considered. Various numerical examples are presented to illustrate this approach. This method is straightforward and accurate for modelling sound transmission through composite honeycomb panels with an arbitrary complex core.

4.2 Theory and Formulation

In section 4.2.1, a fluid/structure coupled system is described where the fluids are modelled analytically. A periodic cell of the structure is modelled by a detailed FE mesh in section 4.2.2. Model reduction is described in section 4.2.3. The acoustic pressures are discretised into external nodal forces in section 4.2.4. A reduced WFE model is developed in section 4.2.5 for calculating the forced response to acoustic excitations. Modal density and group velocity are considered in section 4.2.6 for comparison with the approximate models in the literature. The diffuse-field STL is found using the formula developed in chapter 2. In section 4.3, numerical examples are presented to illustrate the accuracy of the WFE model, including an aerospace

grade aluminium honeycomb-cored panel, honeycomb-cored panels consisting of steel skins and hexagonal aluminium core and a composite honeycomb-cored panel made up of square Nomex core and carbon reinforced epoxy resin skins. For simple honeycomb structures, approximate models are readily developed. The analytical results are compared to the results predicted by the WFE method. Experimental data in the literature is also taken for comparison for validating the accuracy of this method. The WFE method is then applied to a complicated honeycomb-cored structure with composite skins and a square core, for which developing an analytical model is difficult.

4.2.1 Fluid-Structure Interaction

Assume an oblique plane wave (see equation (2.14)) is incident at an angle θ to the normal of the top surface of the infinite honeycomb-cored panel shown in figure 4.1. The motion, in turn, excites reflected and transmitted waves (see equation 2.15) in the upper and lower half-spaces respectively.

For a periodic structure, the response also has space harmonics with wavenumbers, $(k_x + 2m\pi/L_x, k_y + 2n\pi/L_y)$ with m and n being integers [46] and L_x and L_y being the lengths of the periodic cell in the x and y directions. Here it is assumed that the frequency is low enough so that the amplitudes of these space harmonics are negligible, i.e. $k_x L_x, k_y L_y \leq 1$. For typical honeycomb-cored structures this covers the audiofrequency range.

The continuity condition at the interfaces between the structure and the surrounding fluids relates the acoustic pressures to the normal displacements of the skins (similar to equation (2.20)).

4.2.2 FE Model of a Periodic Cell

As an example, consider the infinite honeycomb-cored structure shown in figure 4.1 for which the core is a regular hexagonal honeycomb. The core can be arbitrary shaped, e.g. square,

triangular, etc. Only a periodic cell of the entire structure needs to be modelled using a conventional FE method. The geometrical parameters of the honeycomb core of the structure are described by the five parameters shown in figure 4.2, the included cell angle α , wall length of the core h , angled length l , wall thickness t , and core thickness h_c . The selection of the periodic cell is not unique. Figure 4.3 shows two potential periodic cells, along with the FE model of a rectangular periodic cell of the structure.

The FE model in figure 4.3(b) was created using mixed triangular and quadrilateral shell elements. The only constraint for the FE mesh is that the nodes along the connected edges of the core, and the top and bottom skins of the periodic cell must be identically arranged. The total DOFs \mathbf{q} of the FE model can be partitioned into boundary (edge (l,r,b,t) , corner $(1,2,3,4)$), and interior DOFs (I). The boundary and internal DOFs are indicated by subscripts “ B ” and “ I ” respectively such that

$$\mathbf{q} = [\mathbf{q}_B^T \quad \mathbf{q}_I^T]^T, \quad (4.1)$$

where the superscript “ T ” denotes the transpose, and

$$\mathbf{q}_B = [\mathbf{q}_1^T \quad \mathbf{q}_2^T \quad \mathbf{q}_3^T \quad \mathbf{q}_4^T \quad \mathbf{q}_b^T \quad \mathbf{q}_r^T \quad \mathbf{q}_t^T \quad \mathbf{q}_l^T]^T. \quad (4.2)$$

Similarly, for the nodal forces,

$$\mathbf{f} = [\mathbf{f}_B^T \quad \mathbf{f}_I^T]^T, \quad (4.3)$$

where

$$\mathbf{f}_B = [\mathbf{f}_1^T \quad \mathbf{f}_2^T \quad \mathbf{f}_3^T \quad \mathbf{f}_4^T \quad \mathbf{f}_b^T \quad \mathbf{f}_r^T \quad \mathbf{f}_t^T \quad \mathbf{f}_l^T]^T. \quad (4.4)$$

Assuming time-harmonic motion, the equation of motion of the periodic cell can be written as

$$\mathbf{D}\mathbf{q} = \mathbf{f} + \mathbf{e}, \quad \mathbf{D} = \mathbf{K} - \omega^2\mathbf{M}, \quad (4.5)$$

where \mathbf{D} is dynamic stiffness matrix, ω is the angular frequency, \mathbf{e} represents the external nodal forces, the structural damping is neglected for simplicity but could be included readily by a viscous damping matrix \mathbf{C} or by \mathbf{K} being complex.

If a small periodic cell is used, at very low frequencies, the calculation of the DSM inside the square bracket of equation (4.5) can lead to substantial round-off errors: K_{ij} is very large compared to $\omega^2 M_{ij}$ such that some digits associated with the inertia terms are truncated. The number of the digits truncated can be estimated by $n_{ij} = \log_{10} \left(\left| \frac{K_{ij}}{\omega^2 M_{ij}} \right| \right)$ [112]. However this error can be reduced by meshing a larger periodic cell or using higher precision arithmetic. As an alternative, a number of the original FE model of the small periodic cell are concatenated to form a super FE model without remodelling a large periodic cell [112].

4.2.3 Reduction of the FE Model

For modelling the complicated geometry of the periodic cell, the FE model can have a large number of internal nodes. In order to reduce the computational cost, the DOFs need to be condensed. There are many existing methods for reducing the size of the mass and stiffness matrices (e.g., Guyan reduction [32], CMS condensation [29]). In this chapter, Guyan reduction is used. For convenience, the FE model without condensation is simply referred to as the “full model”. Assume the total DOFs of the full model are categorised into master DOFs, and slave DOFs, which are respectively denoted by subscripts “ m ” and “ s ”. With this arrangement, the equation of motion can be partitioned as

$$\begin{bmatrix} \mathbf{D}_{mm} & \mathbf{D}_{ms} \\ \mathbf{D}_{sm} & \mathbf{D}_{ss} \end{bmatrix} \begin{Bmatrix} \mathbf{q}_m \\ \mathbf{q}_s \end{Bmatrix} = \begin{Bmatrix} \mathbf{f}_m \\ \mathbf{f}_s \end{Bmatrix}. \quad (4.6)$$

From the second row of equation (4.6), the slave DOFs \mathbf{q}_s may be expressed in terms of the master DOFs \mathbf{q}_m as

$$\mathbf{q}_s = -\mathbf{D}_{ss}^{-1} \mathbf{D}_{sm} \mathbf{q}_m + \mathbf{D}_{ss}^{-1} \mathbf{f}_s, \quad (4.7)$$

where \mathbf{D}_{ss} is the dynamic stiffness matrix associated with the slave DOFs. Its inverse can be written as

$$\mathbf{D}_{ss}^{-1} = (\mathbf{K}_{ss} - \omega^2 \mathbf{M}_{ss})^{-1} = (\mathbf{I} - \omega^2 \mathbf{K}_{ss}^{-1} \mathbf{M}_{ss})^{-1} \mathbf{K}_{ss}^{-1}. \quad (4.8)$$

This leads to dynamic condensation of the slave DOFs, with \mathbf{D}_{ss}^{-1} having to be recalculated at each frequency. If the effects of the slave DOF inertia are neglected, equation (4.8) can be approximated by [128]

$$\mathbf{D}_{ss}^{-1} = \mathbf{K}_{ss}^{-1} + O(\omega^2 \mathbf{K}_{ss}^{-1} \mathbf{M}_{ss} \mathbf{K}_{ss}^{-1}). \quad (4.9)$$

Then

$$\mathbf{q}_s = -\mathbf{K}_{ss}^{-1} \mathbf{K}_{sm} \mathbf{q}_m. \quad (4.10)$$

Therefore the displacement vector \mathbf{q} can be expressed as

$$\mathbf{q} = \begin{Bmatrix} \mathbf{q}_m \\ \mathbf{q}_s \end{Bmatrix} = \mathbf{R} \mathbf{q}_m, \quad (4.11)$$

where the coordinate transformation matrix \mathbf{R} relates the DOFs to the master DOFs, and is given by

$$\mathbf{R} = \begin{bmatrix} \mathbf{I} \\ -\mathbf{K}_{ss}^{-1} \mathbf{K}_{sm} \end{bmatrix}. \quad (4.12)$$

Substituting equation (4.11) into equation (4.6), and premultiplying by \mathbf{R}^T yields

$$\bar{\mathbf{D}} \mathbf{q}_m = \mathbf{f}_m, \quad \bar{\mathbf{D}} = \bar{\mathbf{K}} - \omega^2 \bar{\mathbf{M}} \quad (4.13)$$

where $\bar{\mathbf{D}}$ is the dynamic stiffness matrix of the reduced model, $\bar{\mathbf{K}}$ and $\bar{\mathbf{M}}$ are the equivalent mass and stiffness matrices, given by

$$\begin{aligned}\bar{\mathbf{K}} &= \mathbf{K}_{mm} - \mathbf{K}_{ms} \mathbf{K}_{ss}^{-1} \mathbf{K}_{sm} \\ \bar{\mathbf{M}} &= \mathbf{M}_{mm} - \mathbf{K}_{ms} \mathbf{K}_{ss}^{-1} \mathbf{M}_{sm} - \mathbf{M}_{ms} \mathbf{K}_{ss}^{-1} \mathbf{K}_{sm} + \mathbf{K}_{ms} \mathbf{K}_{ss}^{-1} \mathbf{M}_{ss} \mathbf{K}_{ss}^{-1} \mathbf{K}_{sm}.\end{aligned}\quad (4.14)$$

This is Guyan reduction, or static condensation. Note that the equivalent mass and stiffness matrices are independent of ω and thus the model reduction needs to be done only once for all frequencies. The combination of mass and stiffness submatrices in equation (4.14) reduces round-off errors after calculating the equivalent mass matrix.

To reduce the errors due to neglecting the high-order inertia terms by Guyan reduction, equation (4.9) can be expressed in a higher-order Taylor series. More details about improving the accuracy of Guyan reduction can be found in Refs. [33, 128].

An alternative model reduction method is CMS [29]. There are many forms of CMS, with perhaps the most common being Craig-Bampton (CB) or fixed interface CMS. In CB CMS all the boundary DOFs are selected as the master DOFs whereas the internal DOFs are the slave DOFs. The CB CMS uses a coordinate transformation matrix

$$\mathbf{R} = \begin{bmatrix} \mathbf{I} & \mathbf{0} \\ -\mathbf{K}_{ss}^{-1} \mathbf{K}_{sm} & \Phi_c \end{bmatrix} \quad (4.15)$$

where Φ_c consists of a set of retained modal vectors found by solving the eigenvalue problem

$$\left[\mathbf{K}_{ss} - \omega^2 \mathbf{M}_{ss} \right] \mathbf{q}_s = \mathbf{0}. \quad (4.16)$$

The coordinate transformation matrix \mathbf{R} relates the total DOFs \mathbf{q} to the physical DOFs \mathbf{q}_m of the boundary nodes and a subset of modal DOFs \mathbf{q}_c by

$$\mathbf{q} = \begin{bmatrix} \mathbf{q}_m \\ \mathbf{q}_s \end{bmatrix} = \mathbf{R} \begin{bmatrix} \mathbf{q}_m \\ \mathbf{q}_c \end{bmatrix} \quad (4.17)$$

where the modal DOFs \mathbf{q}_c can be eliminated by dynamic condensation [98, 134]. Note that Guyan reduction is the same as CB if no fixed interface modes are retained. More details can be found in Ref. [29].

4.2.4 Acoustic Excitation

After the FE discretisation, the acoustic pressures on the top and bottom surfaces are discretised into external nodal forces on those DOFs that correspond to the normal displacements $w_{1,2}$ of the two skins. Therefore,

$$\mathbf{e} = 2\tilde{p}_i \mathbf{e}_0 - D_{f,1} \Gamma_1 \mathbf{q} - D_{f,2} \Gamma_2 \mathbf{q} \quad (4.18)$$

where \mathbf{e}_0 is a nodal force vector; Γ_1 and Γ_2 are left diagonal matrices. All the elements in the vector, and the two matrices are zero, except for those corresponding to the normal displacement of the interfaces between the periodic cell and the fluids; The non-zero elements represent the equivalent nodal forces which can be calculated as consistent nodal forces using equation (2.25) of chapter 2.

Substituting equation (4.11) into equation (4.18) gives

$$\mathbf{e} = 2\tilde{p}_i \mathbf{e}_0 - D_{f,1} \Gamma_1 \mathbf{R} \mathbf{q}_m - D_{f,2} \Gamma_2 \mathbf{R} \mathbf{q}_m. \quad (4.19)$$

Again inserting equation (4.19) into equation (4.5), and premultiplying equation (4.5) by \mathbf{R}^T lead to

$$(\bar{\mathbf{D}} + \bar{\mathbf{\Phi}}) \mathbf{q}_m = \mathbf{f}_m + \bar{\mathbf{e}} \quad (4.20)$$

where $\bar{\mathbf{\Phi}}$ denotes the effect of fluid loading, $\bar{\mathbf{e}}$ represents the equivalent external nodal forces at the master DOFs of the reduced model, They can be expressed as

$$\bar{\mathbf{\Phi}} = D_{f,1} \mathbf{R}^T \Gamma_1 \mathbf{R} + D_{f,2} \mathbf{R}^T \Gamma_2 \mathbf{R}, \quad \bar{\mathbf{e}} = 2\tilde{p}_i \mathbf{R}^T \mathbf{e}_0. \quad (4.21)$$

4.2.5 The WFE Model and Sound Transmission

The analysis now follows the lines described in chapter 2 while the main steps are summarised here. Note that the model, here, contains a large number of internal DOFs which are condensed using Guyan reduction. The boundary DOFs are condensed using the periodicity conditions.

Assuming a plane wave propagates through the structure, the nodal DOFs at the corners of the periodic cell (see figure 3(b)) can be related by the periodicity (see equation (2.30)), where the wave propagation constants are the same as equation (2.31). Similarly, for the DOFs at the bottom, top, left, and right edges,

$$\mathbf{q}_r = \lambda_x \mathbf{q}_l, \quad \mathbf{q}_t = \lambda_y \mathbf{q}_b. \quad (4.22)$$

Hence,

$$\mathbf{q}_B = \Lambda_R \begin{Bmatrix} \mathbf{q}_l \\ \mathbf{q}_t \\ \mathbf{q}_b \end{Bmatrix}, \quad \Lambda_R = \begin{bmatrix} \mathbf{I} & \lambda_x \mathbf{I} & \lambda_y \mathbf{I} & \lambda_x \lambda_y \mathbf{I} & \mathbf{0} & \mathbf{0} & \mathbf{0} & \mathbf{0} \\ \mathbf{0} & \mathbf{0} & \mathbf{0} & \mathbf{0} & \mathbf{0} & \lambda_x \mathbf{I} & \mathbf{0} & \mathbf{I} \\ \mathbf{0} & \mathbf{0} & \mathbf{0} & \mathbf{0} & \mathbf{I} & \mathbf{0} & \lambda_y \mathbf{I} & \mathbf{0} \end{bmatrix}^T. \quad (4.23)$$

Equilibrium at hypernode 1 gives the same equation as equation (2.33) while equilibrium at the left, and bottom mid-side nodes leads to

$$\mathbf{f}_l + \lambda_x^{-1} \mathbf{f}_r = \mathbf{0}, \quad \mathbf{f}_b + \lambda_y^{-1} \mathbf{f}_t = \mathbf{0}. \quad (4.24)$$

Therefore,

$$\Lambda_L \mathbf{f}_B = \begin{Bmatrix} \mathbf{0} \\ \mathbf{0} \\ \mathbf{0} \end{Bmatrix}, \quad \Lambda_L = \begin{bmatrix} \mathbf{I} & \lambda_x^{-1} \mathbf{I} & \lambda_y^{-1} \mathbf{I} & \lambda_x^{-1} \lambda_y^{-1} \mathbf{I} & \mathbf{0} & \mathbf{0} & \mathbf{0} & \mathbf{0} \\ \mathbf{0} & \mathbf{0} & \mathbf{0} & \mathbf{0} & \mathbf{0} & \lambda_x^{-1} \mathbf{I} & \mathbf{0} & \mathbf{I} \\ \mathbf{0} & \mathbf{0} & \mathbf{0} & \mathbf{0} & \mathbf{I} & \mathbf{0} & \lambda_y^{-1} \mathbf{I} & \mathbf{0} \end{bmatrix}. \quad (4.25)$$

For Guyan reduction, if all the boundary DOFs are selected as the master DOFs, that is, $\mathbf{q}_B = \mathbf{q}_m$, substituting equation (4.23) into equation (4.20), and premultiplying by Λ_L gives

$$\tilde{\mathbf{D}} \begin{Bmatrix} \mathbf{q}_l \\ \mathbf{q}_b \end{Bmatrix} = \tilde{\mathbf{e}}, \quad \tilde{\mathbf{D}} = \tilde{\mathbf{K}} - \omega^2 \tilde{\mathbf{M}} + \tilde{\mathbf{\Phi}}, \quad \tilde{\mathbf{e}} = \Lambda_L \bar{\mathbf{e}} \quad (4.26)$$

where $\tilde{\mathbf{D}}$ is the reduced spectral dynamic stiffness matrix, and

$$\tilde{\mathbf{K}} = \Lambda_L \bar{\mathbf{K}} \Lambda_R, \quad \tilde{\mathbf{M}} = \Lambda_L \bar{\mathbf{M}} \Lambda_R, \quad \tilde{\mathbf{\Phi}} = \Lambda_L \bar{\mathbf{\Phi}} \Lambda_R. \quad (4.27)$$

Once the structural response is calculated from equation (4.26), the reflected and transmitted acoustic pressures then follow from equation (2.20). Equations (2.41-2.43) are used to calculate the diffuse-field STL.

4.2.6 Modal Density and Group Velocity

The total number of modes below an angular frequency ω for a panel having area A can be estimated by [101]

$$N(\omega) = \frac{A}{4\pi^2} \int_S dk_x dk_y \quad (4.28)$$

where the integration region S is defined as the projected area in the (k_x, k_y) plane of the propagation surface for frequencies below the given frequency ω . The mode counts can be expressed in polar coordinate as

$$N(\omega) = \frac{A}{8\pi^2} \int_0^{2\pi} k^2(\theta, \omega) d\theta, \quad k(\theta, \omega) = \sqrt{k_x^2(\theta, \omega) + k_y^2(\theta, \omega)}. \quad (4.29)$$

Then, the modal density can be written as

$$n(\omega) = \frac{\partial N(\omega)}{\partial \omega} = \int_0^{2\pi} n(\theta, \omega) d\theta, \quad n(\theta, \omega) = \frac{Ak(\theta, \omega)}{4\pi^2 c_g(\theta, \omega)} \quad (4.30)$$

where $c_g(\theta, \omega) = \partial \omega / \partial k(\theta, \omega)$ is the group velocity in the direction of the normal to the curves in the wavenumber plane for constant ω [102]. For the undamped structure, the group velocity

is equal to the velocity of energy flow. The group velocity is an important characteristic for wave analysis.

The group velocity might be evaluated numerically using a finite element difference method, as seen in Ref. [111] where the wavenumbers of various waves were obtained by solving eigenproblems using the WFE method for one-dimensional waveguides. An alternative way can be found from the eigenvalue problem of equation (4.26) or so by making $\bar{\Phi} = \mathbf{0}$ and $\tilde{\mathbf{e}} = \mathbf{0}$, i.e. for free wave propagation neglecting fluid loading. Let $(\omega, \boldsymbol{\varphi})$ represents a solution for a particular wave type. Evaluating the partial derivative of the equation with respect to wavenumber $k(\theta, \omega)$ leads to [119]

$$\left[\frac{\partial \Lambda_L}{\partial k(\theta, \omega)} \bar{\mathbf{D}} \Lambda_R + \Lambda_L \bar{\mathbf{D}} \frac{\partial \Lambda_R}{\partial k(\theta, \omega)} - 2\omega \frac{\partial \omega}{\partial k(\theta, \omega)} \tilde{\mathbf{M}} \right] \boldsymbol{\varphi} + (\tilde{\mathbf{K}} - \omega^2 \tilde{\mathbf{M}}) \frac{\partial \boldsymbol{\varphi}}{\partial k(\theta, \omega)} = \mathbf{0}. \quad (4.31)$$

Note that $\tilde{\mathbf{K}}$ and $\tilde{\mathbf{M}}$ are Hermitian matrices, and eigenvectors $\boldsymbol{\varphi}$ are mass normalised such that $\boldsymbol{\varphi}^H \tilde{\mathbf{M}} \boldsymbol{\varphi} = 1$. Pre-multiplying equation (4.31) by $\boldsymbol{\varphi}^H$ leads to [119]

$$\frac{\partial \omega}{\partial k(\theta, \omega)} = \frac{1}{2\omega} \left[\boldsymbol{\varphi}^H \frac{\partial \Lambda_L}{\partial k} \bar{\mathbf{D}} \Lambda_R \boldsymbol{\varphi} + \boldsymbol{\varphi}^H \Lambda_L \bar{\mathbf{D}} \frac{\partial \Lambda_R}{\partial k} \boldsymbol{\varphi} \right] \quad (4.32)$$

where the superscript ‘‘H’’ denotes the conjugate transpose.

Once the wavenumber and eigenvector are found for a given frequency and direction of wave propagation, the group velocity can be calculated using equation (4.32). Note that equations (4.31, 4.32) are only valid in vacuo.

4.3 Numerical Examples

In this section, numerical examples are presented to illustrate this method, including an aerospace grade hexagonal honeycomb-cored panel, two honeycomb-cored panels made up of steel skins and a regular hexagonal aluminium core, and a composite honeycomb-cored

structure having a square core. The dispersion curves, modal density, group velocity, and STL are calculated using equivalent models from the literature, the WFE model, and the results compared.

4.3.1 Honeycomb Panels with Hexagonal Core and Isotropic Skins

1. Wavenumber analysis

Consider a honeycomb-cored panel consisting of aluminium skins and a regular hexagonal core. The material and geometrical properties shown in table 4.1 (panel 1) are taken from Ref. [28]. A rectangular periodic cell ($L_x=5.2\text{mm}$, $L_y=9\text{mm}$) of the structure is used and meshed using 500 ANSYS SHELL181 elements. The full FE model (full model 1) has 278 nodes, and each node of the element has six DOFs, which leads to a total of 1668 DOFs. The number of internal nodes is 180 with 1080 DOFs.

For checking the convergence of the FE mesh shown in figure 4.3(b), the FE mesh is refined using 1104 ANSYS SHELL181 elements (full model 2). The total number of nodes increases to 887 with 685 internal nodes. Due to the complexity of the core geometry, the element size should not be too coarse, otherwise, the FE model is unable to capture the abrupt changes in the core geometry. The intersection edges between the skins and the walls of the core should be discretised, and the nodes must match. Figures 4.4 and 4.5 show the wavenumber predicted using the two full WFE models. It can be seen that the wavenumber agreement is excellent for the bending (figure (4.4)), shear (figure (4.5)), and extensional (figure (4.5)) waves. Note that the full model contains a large number of DOFs. In order to avoid the numerical issues which arise from solving the ill-conditioned eigenvalue problem (e.g., using a transfer matrix method [112].), Zhong's method [124] is used for calculating the eigenvalues.

For validation, the wavenumber for wave propagation in the x -propagation direction is also calculated using various approximate models. The equivalent material properties of these models are calculated using equations in reference [25]. Also, the analytical results are compared with those of the full WFE model (full model 1). Figure 4.6 shows the wavenumber of the bending wave while figure 4.7 shows the wavenumbers of the shear (the upper curve), and extensional waves (the lower curve).

The first approximate model is an isotropic plate with an equivalent shear stiffness developed in Ref. [23]. It can be seen from figure 4.6 that the wavenumber agreement between the equivalent model and the full WFE model is good below 250 Hz. Above 250 Hz, the wavenumber discrepancies increase with the frequency up to 2 kHz. The wavenumbers of the shear, and extensional waves are shown in figure 4.7. The simple model assumes that the skin thickness is much smaller than the core thickness such that the bending stiffness of the skin is negligible and a sixth-order differential equation reduces to a fourth-order one.

The second model is a three-dimensional laminate panel whose honeycomb core is approximated as a continuous medium with nine equivalent elasticity moduli calculated by the method described in Ref. [22]. The wavenumbers are predicted numerically using the WFE method [113]. It can be seen from figure 4.6 that that similar wavenumber discrepancies between the equivalent model and the full WFE model can be observed for the bending wave. For example, at low frequencies (below 250Hz), the wavenumber agreement is good whereas at high frequencies (above 250 Hz), the discrepancies are noticeable. Figure 4.7 shows that the wavenumber agreements are excellent for the shear, and extensional waves.

The third model is a one-dimensional, symmetric, three-layer sandwich beam developed by Nilsson *et al.* [26], where the honeycomb core is modelled as an isotropic material with an equivalent shear stiffness, Young's modulus and density. It can be seen from figure 4.6 that the

wavenumber agreement is excellent for the bending wave between the equivalent model and the full WFE model. For the shear, and extensional waves, generally the wavenumber agreement is good as seen in figure 4.7 while small discrepancies can be seen at high frequencies (above 3000 Hz).

The irreducible part of the first Brillouin zone [38] is shown in figure 4.8(a) while the dispersion characteristics around this contour are plotted in figure 4.8(b). Figure 4.8(b) shows that the curves of the in-plane waves (red solid line: shear wave, black dash-dot: extensional wave), and the out-of-plane wave (dash line: bending wave) do not cross but “veer away” from each other. The in-plane motion is coupled to the out-of-plane motion above 6.8 kHz. Similar dispersion characteristics can also be found in Refs. [28, 39]. It can also be seen that there are no stop-bands of wave propagation existing below 6 kHz. Note that the minimum structural wavelength is 95.2mm below 6 kHz whereas the maximum dimension of the periodic cell in the x - y plane is about 10.4 mm. Therefore the homogenisation of the structure as a continuous structure below 6 kHz is reasonable.

2. Group velocity and modal density

A three-dimensional view of the propagation frequency in the wavenumber space is shown in figure 4.9 for the bending wave. It can be seen that the propagation surface is symmetric about the frequency axis (see figure 4.9(a)), and the wavenumber modulus is independent of propagation direction as shown in figure 4.9(b).

The group velocity in the x -direction and modal density are calculated for the bending wave of the structure having an area of 3.87m^2 . Both the WFE models and the approximate model [24] are used. The results are shown in figure 4.10, where a central difference method is used for numerically calculating the group velocity. It can be seen that the agreement is excellent.

3. Sound transmission loss

a) *Air-to-air:*

First consider the case where both fluids are air (density $\rho = 1.21 \text{ kg/m}^3$, the speed of sound $c = 340 \text{ m/s}$). The oblique STL was calculated for given pairs of incidence angles (θ, ϕ) . Both the reduced and full models are used. It can be seen from figure 4.11 that the agreement is excellent. The dips occur when the wavelength of the acoustic trace wave equals to that of the structural bending wave, e.g. 450 Hz ($\theta = 80^\circ$), 625 Hz ($\theta = 60^\circ$), and 2450 Hz ($\theta = 40^\circ$). The wavelength matches can also be seen in figure 4.12. For this choice of structure and fluid, the effects of fluid loading are generally weak, although it should be noted that they are significant at, and around the coincidence frequency.

The small-sized model is used to calculate the diffuse-field STL which is compared with that of an approximate model having nine stiffness constants (see figure 4.13). Overall, the approximate model can predict the STL well except for around the coincidence frequencies. The reduced WFE model predicts coincidence at 550 Hz whereas the approximate model at 500 Hz. The reason is that the equivalent model underestimates the wavenumber for the bending wave as observed in figure 4.4.

For comparison with measurements in reference [77], another two honeycomb-cored panels (panel 2 and panel 3) with isotropic steel faces are considered. They have the same material properties (shown in table 4.1) but different thicknesses. The predicted diffuse-field STL is plotted together with the measurements in one-third octave bands in figure 4.14. The agreement can be seen to be reasonable. The WFE model predicts the coincidence frequency at 500 Hz for the first panel of 25-mm thickness while for the other panel (30-mm thickness), the STL dip occurs at 400Hz.

b) *Air-to-water:*

Now consider the case where water ($\rho = 1000 \text{ kg/m}^3$, $c = 1500 \text{ m/s}$) occupies the space $z \leq 0$. Since the two media have different wave speeds refraction occurs, with there being no propagating transmitted wave for angles of incidence greater than 14.2° . Figure 4.15(a) shows the 3D plot of the magnitude of the power transmission coefficient $\tau(\theta, \phi)$ as a function of the angle of incidence θ , and frequency, while the diffuse-field STL is shown in Figure 4.15(b).

4.3.2 Honeycomb Panels with Composite Faces and Square Core

1. Dispersion characteristics

A honeycomb-cored panel having composite skins and square core is considered in this section. The stacking sequence of the laminate skins and the material properties (panel 4) are shown in table 4.1 [136]. Again, a rectangular periodic cell ($L_x = L_y = 4.76 \text{ mm}$) is modelled using FE. Multi-layer triangular ANSYS SHELL181 elements are used to discretise the skins of the periodic cell, and the core is modelled using 4-noded rectangular ANSYS SHELL181 elements. The FE model contains a total of 131 nodes with 63 internal nodes. The drilling DOFs (rotation about the z -axis) of the skins are neglected. The FE model of the periodic cell is shown in figure 4.16.

Figure 4.17 shows the variation of the wavenumber at 6 kHz. For the bending wave, figure 4.17 (a) shows that the magnitude of the wavenumber modulus does not vary significantly with directions. In contrast, in figure 4.17(b), the directionality of wave propagation is clear for the shear (outer curve), and extensional waves (inner curve). Furthermore the minimum structural wavelength is 86.1mm below 6 kHz while the maximum dimension of the periodic cell is 6.7 mm in the x - y plane. The structural wavelength is much larger than the dimensions of the cell. The homogenisation of the structure is reasonable.

Again Guyan reduction is used to reduce the size of the model. All the boundary DOFs are selected as master DOFs while all the internal DOFs are slave DOFs. The slave DOFs of the

periodic cell have a minimum natural frequency of 41 kHz when the masters are fixed so that results can be expected to be accurate to about 1/3 of this frequency [35]. Figure 4.18 shows the wavenumbers predicted by the full and reduced models. It can be seen that the wavenumber agreement is excellent (branch *a*: bending wave, branch *b*: shear wave, branch *c*: extensional wave).

2. Sound transmission loss

The oblique STL is predicted for three acoustic plane waves with incidence angles (θ, ϕ) using the full and reduced models respectively, where the fluid spaces are filled with air. The results are shown in figure 4.19. It can be seen that the agreement is excellent. The dips occurring at 560 Hz, and 840 Hz for the two curves ($\theta = 60^\circ$ and $\theta = 80^\circ$) are due to the wavenumber matches between acoustic trace waves and structural bending wave (see figure 4.20). No STL dip occurs for $\theta = 30^\circ$ in the frequency range due to the wavenumber mismatch. The reduced model is used to calculate the diffuse-field STL. The predictions are shown in figure 4.21. A dip can be observed at 762 Hz due to coincidence.

4.4 Conclusions

This chapter described a wave and finite element based homogenised model for predicting the sound transmission loss of infinite honeycomb-cored panels in the frequency range where the structural and acoustic wavelengths are much larger than the dimensions of the periodic cells.

This model is developed using a WFE modelling approach. A three-dimensional periodic cell of the structure is modelled using a conventional finite element method. The geometry complexity can lead to a large number of internal DOFs. For reducing the computational cost, Guyan reduction is used to reduce the model size at low frequencies. By post-processing the relatively small mass and stiffness matrices of the reduced model using a periodic structure theory and equilibrium conditions, the wave propagation characteristics in the structure are

found. Dispersion curves, modal density and group velocity are calculated. Wave propagation in the fluids surrounding the structure is modelled analytically. The acoustic excitation is modelled using equivalent nodal forces. A reduced spectral dynamic stiffness matrix is derived for the homogenised model for calculating the structural response to acoustic excitations.

A series of numerical examples were presented to illustrate this method, including hexagonal honeycomb-cored panels with various core thicknesses, and a honeycomb-cored panel having composite skins and a square core. The predictions (e.g., dispersion characteristics, STL, group velocity and modal density) made by the WFE model were compared with those of approximate models. The STL was also compared to the measurements in the literature. The WFE model can accurately predict the STL of various honeycomb-cored panels. The homogenised model developed in this work is general and can be applied to any complex structure with arbitrary core geometry.

Chapters 2 to 4 considered plane structures. In next chapter, sound transmission through curved structures is considered.

Figures

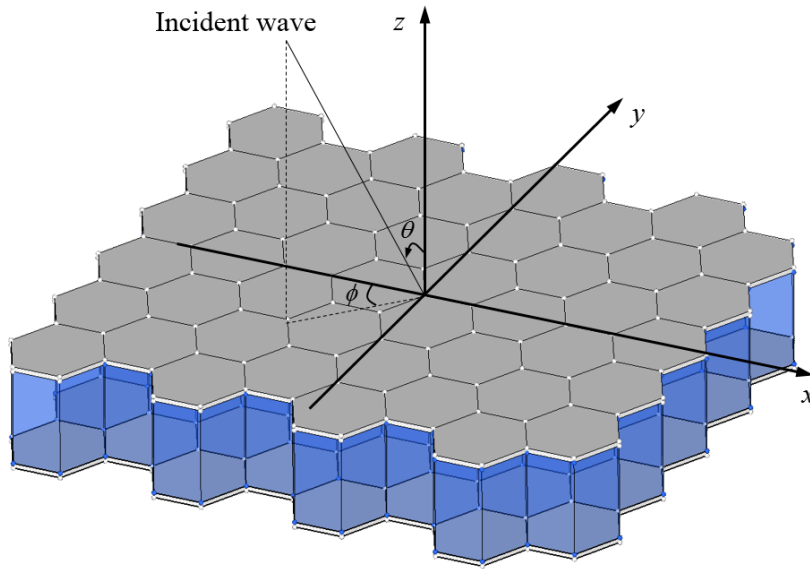


Figure 4.1: Coordinate system definition for sound transmission through an infinite honeycomb-cored panel.

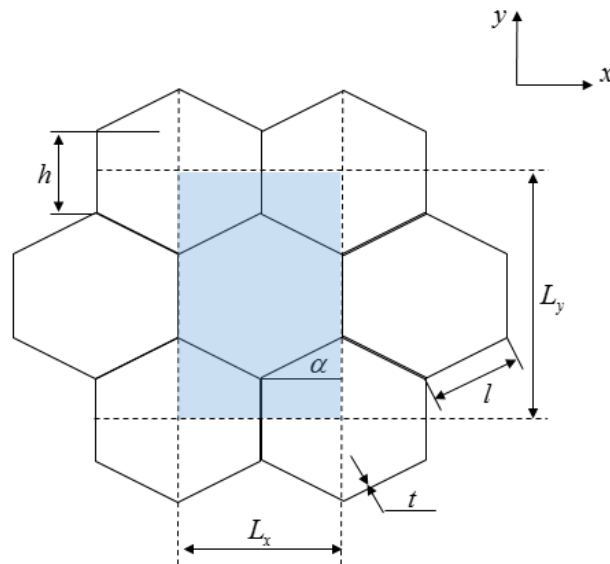


Figure 4.2: Geometrical parameter definition for a honeycomb core where the shaded part denotes a rectangular periodic cell.

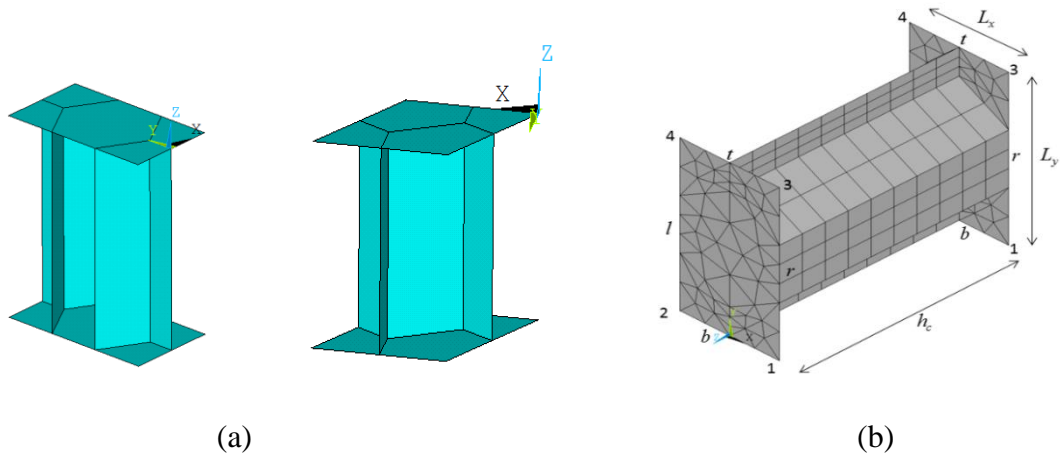


Figure 4.3: Periodic cell and FE model for a honeycomb panel with a regular hexagonal core: (a) a rectangular periodic cell and a parallelogram periodic cell; (b) FE mesh of the rectangular periodic cell with the hyper-nodes marked.

Table 4.1. Physical properties of honeycomb-cored panels

Material parameters	Panel 1 (hexagonal core)	Panels 2 and 3 (steel skins)	Panel 4 (square core)	
Density (kg/m^3)	$\rho = 1670$	$\rho = 7700$	$\rho = 1550$	
Thickness (mm)	1	0.6	0.5	
Skins	Young's modulus (Pa)	1.3×10^{11}	1.95×10^{11}	$E_x = 1.34 \times 10^{11}, E_y = 7.7 \times 10^9,$ $E_z = 7.7 \times 10^9$
	Shear modulus (Pa)	9.7×10^{10}	1.5×10^{11}	$G_{yz} = 2.6 \times 10^9, G_{xz} = 3.1 \times 10^9,$ $G_{xy} = 3.1 \times 10^9$
	Poisson ratio	0.34	0.28	0.03
	Loss factor	0.01	0.015	0.03
Stacking sequence	–	–	$0^\circ/90^\circ$	
Core	Density (kg/m^3)	2700	2700	1240
	Young's modulus (Pa)	7×10^{10}	7.1×10^{10}	5.5×10^9

Shear modulus (Pa)	2.6×10^{10}	2.4×10^{10}	2.7×10^9
Poisson ratio	0.33	0.33	0.33
Cell size l (mm)	3	9.52	4.76
Core thickness h_c (mm)	12	25, 30	19
Wall thickness t (mm)	0.018	0.014	0.076
Loss factor	0.01	0.01	0.03

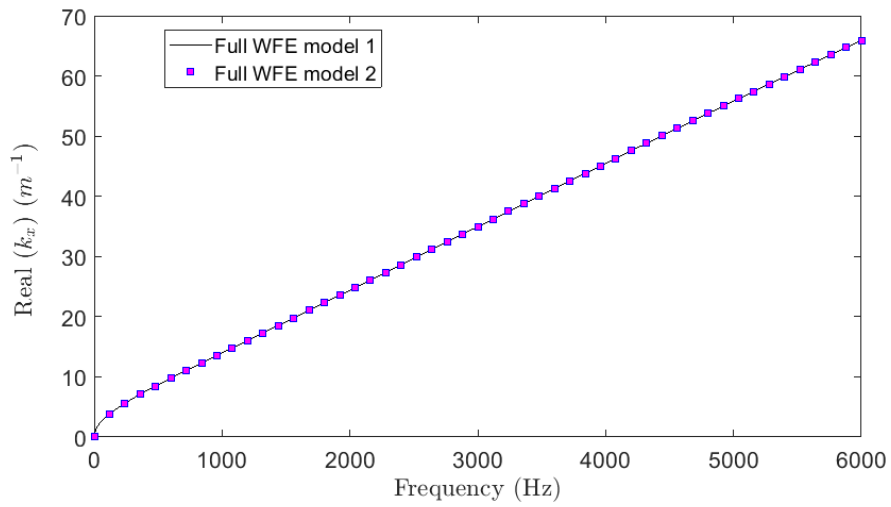


Figure 4.4: Wavenumber comparison (bending wave) between the full WFE models of panel 1: solid line: full model 1; square dot: full model 2.

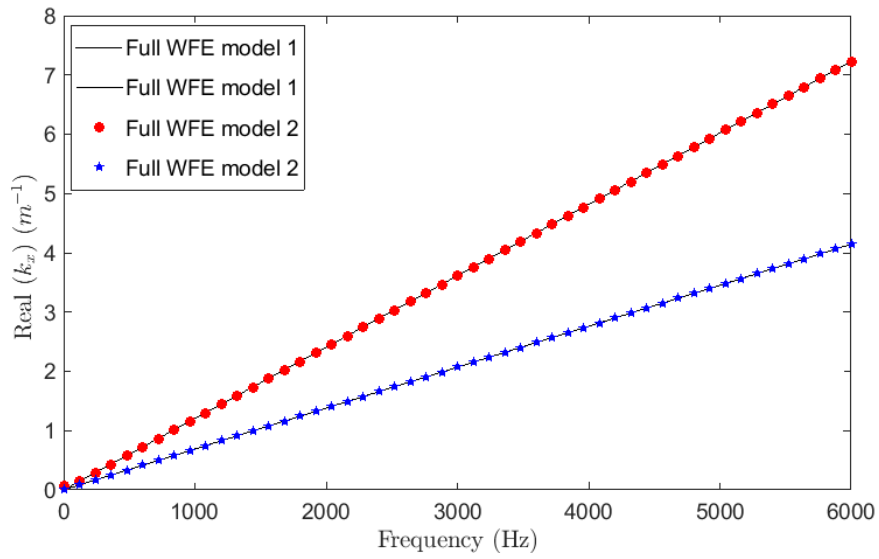


Figure 4.5: Wavenumber comparison (shear, and extensional waves) between the full WFE models of panel 1: solid lines: full model 1; round dot: shear wave (full model 2); star: extensional wave (full model 2).

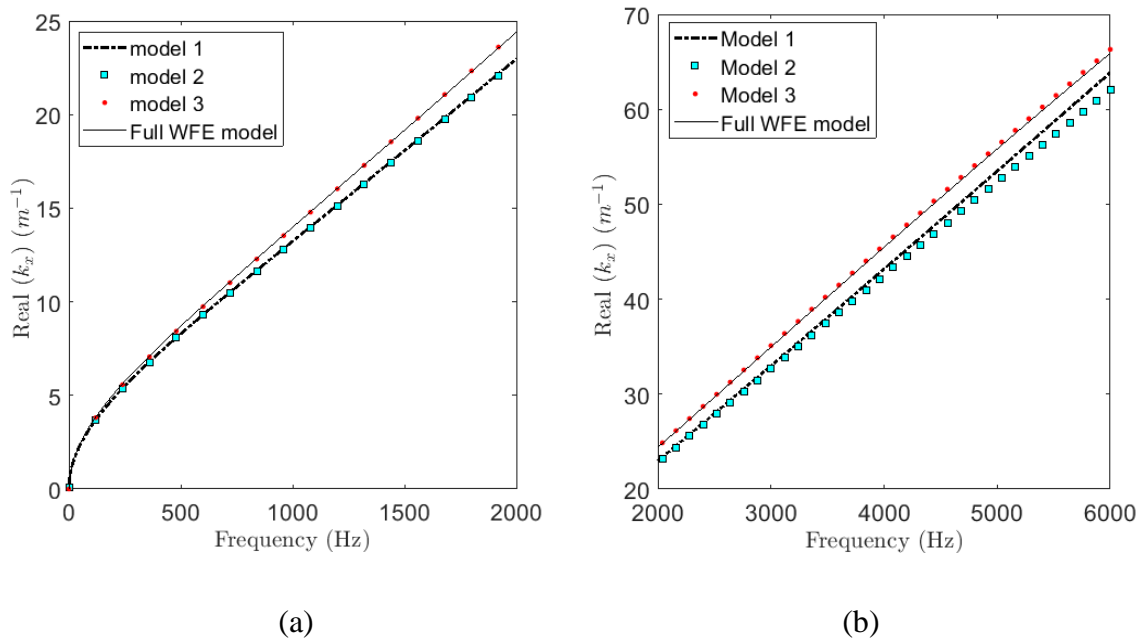


Figure 4.6: Wavenumber comparison for the bending wave between various models: dash line: model 1 (Clarkson and Ranky model [23]); square dot: model 2 (Gibson and Ashby model [22]); Red dot: model 3 (Nilsson and Nilsson model [26]); black line: full WFE model.

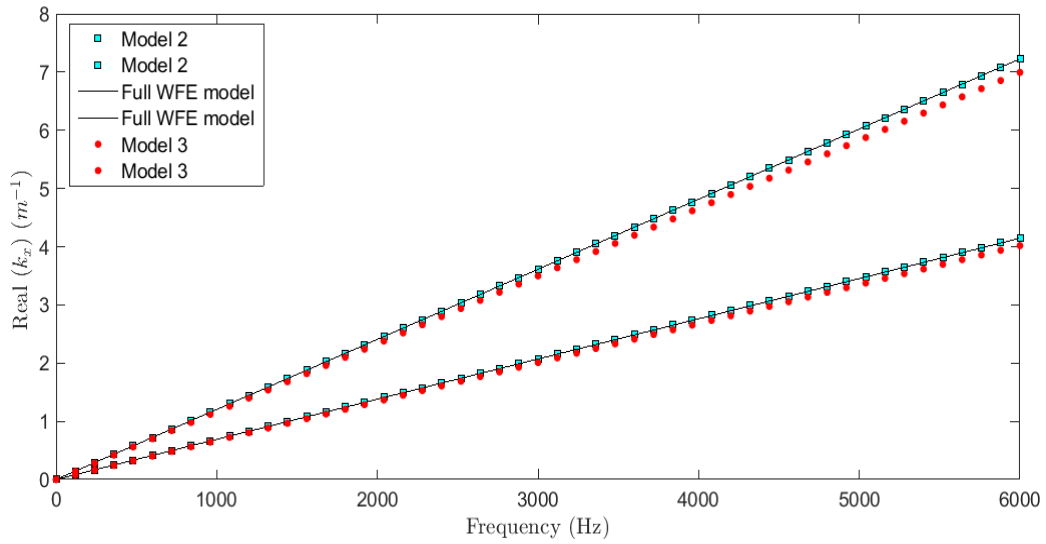


Figure 4.7: Wavenumber comparison for the shear (the upper curve) and extensional waves (the lower curve) between various models: square dot: model 2 (Gibson and Ashby model [22]); Red dot: model 3 (Nilsson and Nilsson model [26]); black line: full WFE model.

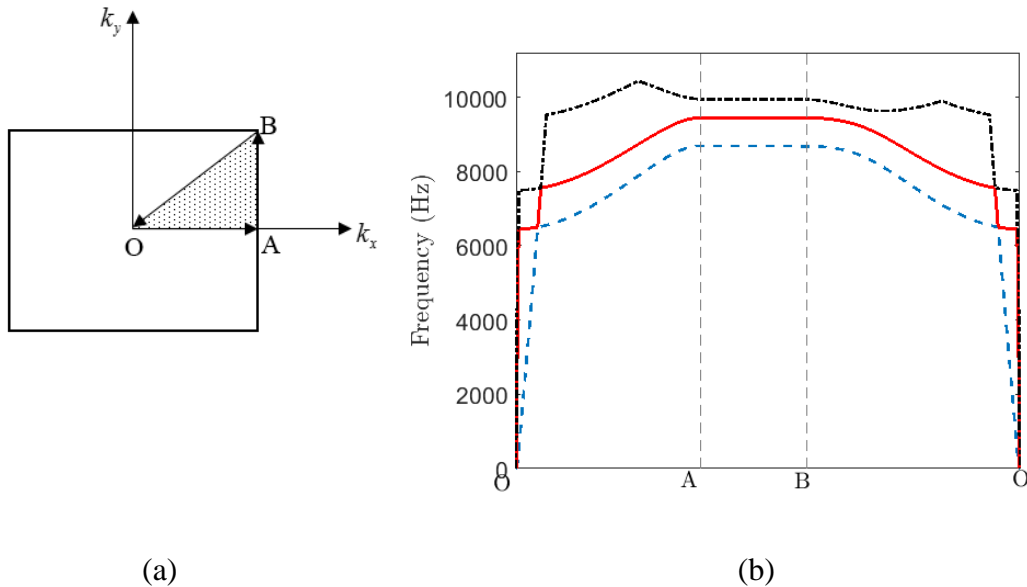


Figure 4.8: First Brillouin zone and propagation frequencies of panel 1: (a) the irreducible Brillouin zone (dotted region), the locus is defined by points O (0, 0), A (0, π/L_x) and B (π/L_y), π/L_x) in the wavenumber space; (b) propagation frequency along the edges of the irreducible part of the first Brillouin zone, red solid line: shear wave, dash line: bending wave, dash dot: extensional wave.

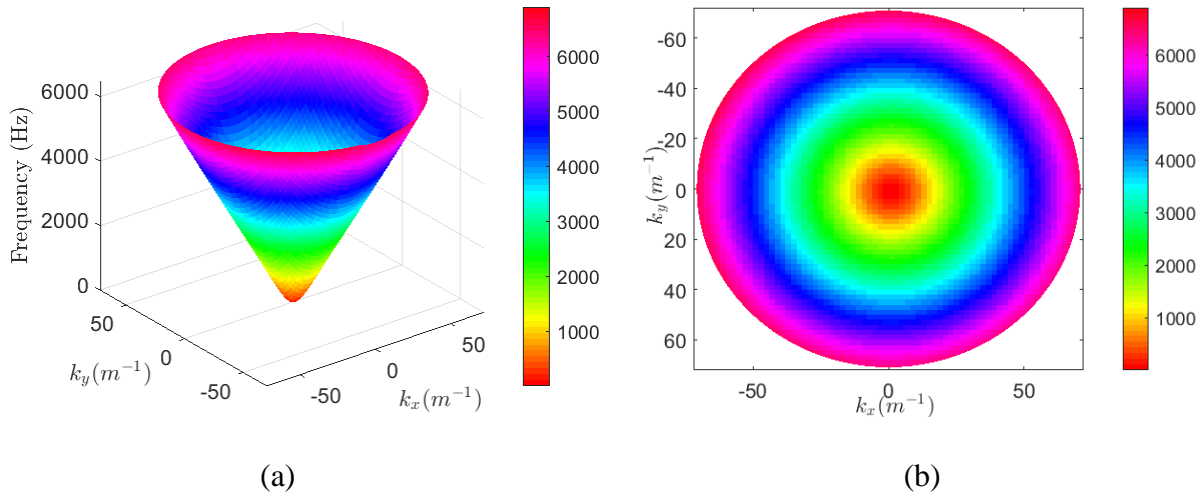


Figure 4.9: Propagation surfaces and directionality of wave propagation of panel 1: (a) three dimensional view of the propagation frequency for the bending wave; (b) directionality of wave propagation.

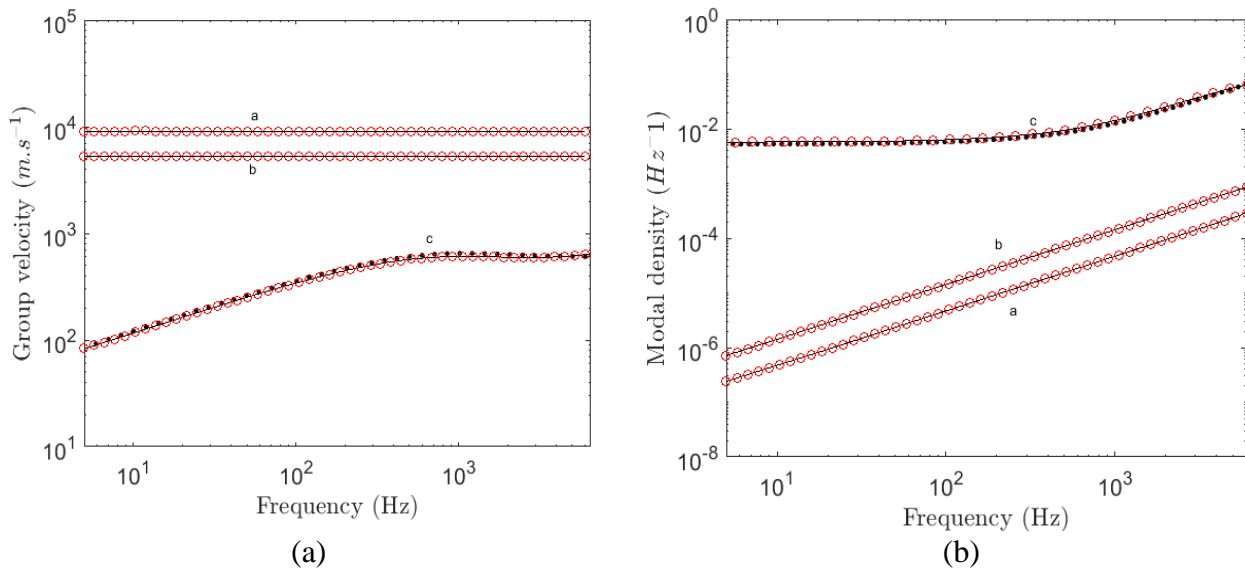


Figure 4.10: Group velocity and modal density of panel 1: (a) group velocity in the x -direction; (b) modal density; extensional wave (a), shear wave (b) and bending wave (c); dots: Renji and Nair model [24]; solid lines: a full WFE model; circles: a reduced WFE model by Guyan reduction.

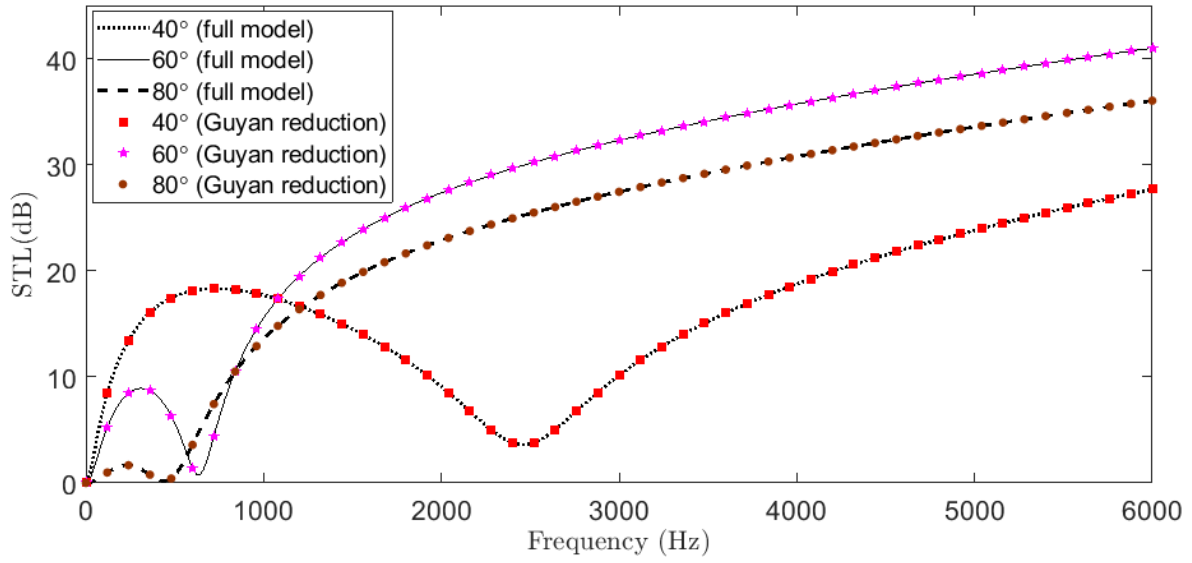


Figure 4.11: Oblique STL for the hexagonal honeycomb-cored panel with isotropic faces (air-to-air, $\phi = 0^\circ$): a full WFE model and a reduced model by Guyan reduction.

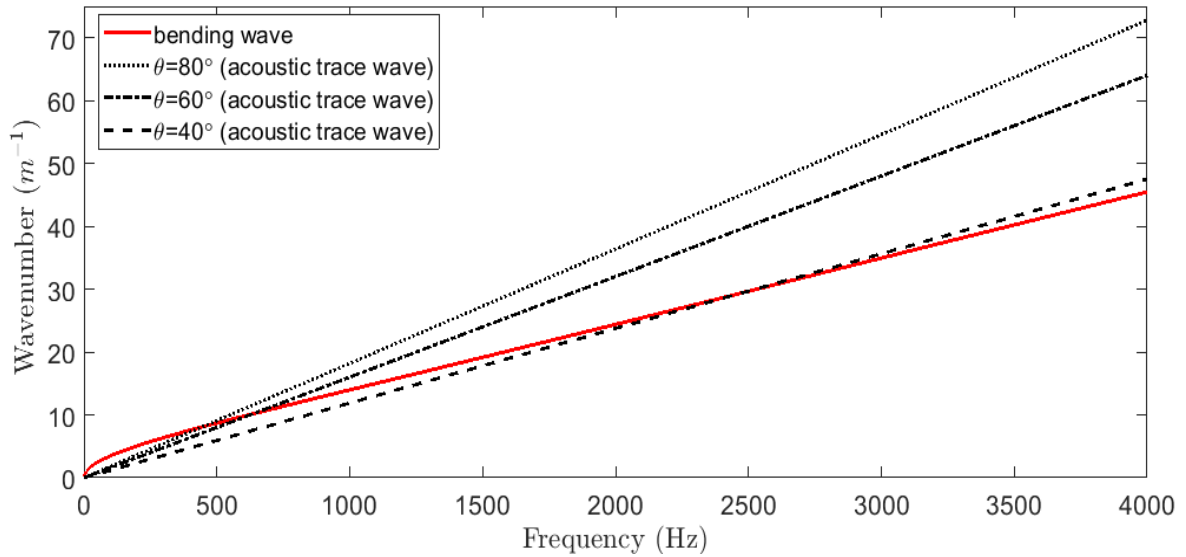


Figure 4.12: Wavenumbers of the bending wave of the hexagonal honeycomb-cored panel, and the acoustic trace wavenumbers.

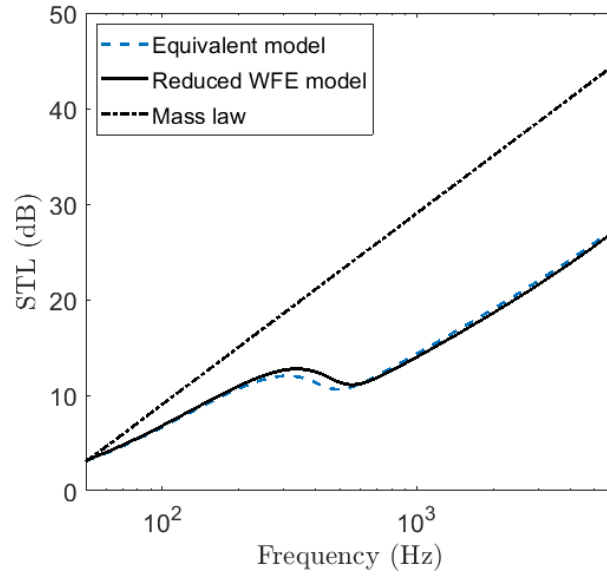


Figure 4.13: Diffuse-field STL comparison (air-to-air) of panel 1: dash line: an equivalent model; solid line: a reduced WFE model by Guyan reduction; dash dot: mass law.

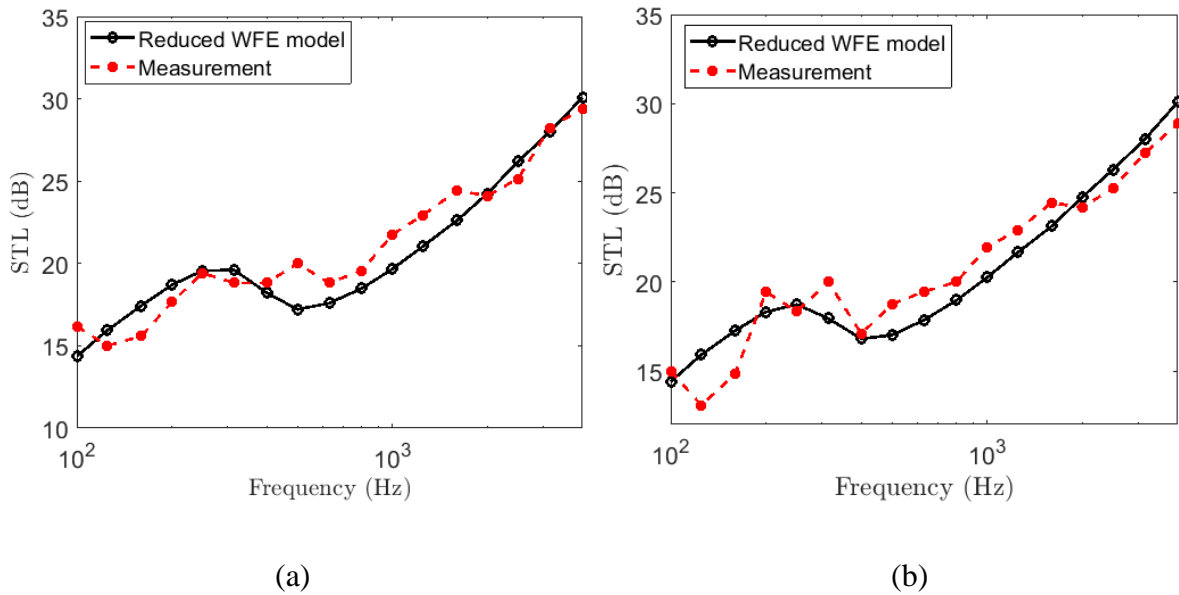


Figure 4.14: Comparison with measurements (air-to-air) of panels 2 and 3: (a) core thickness $h_c = 25\text{mm}$; (b) core-thickness $h_c = 30\text{mm}$.

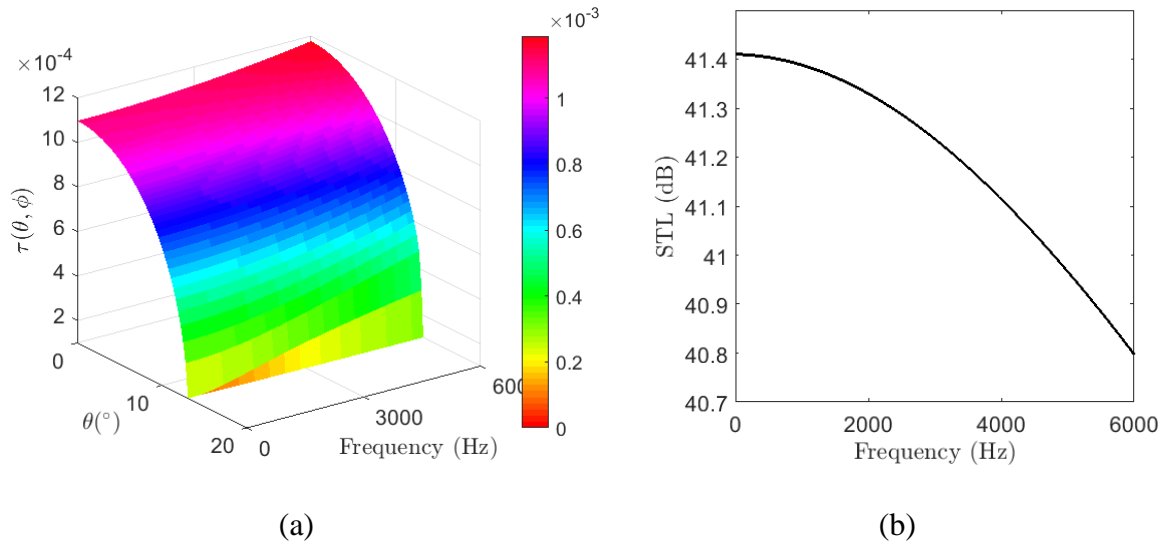


Figure 4.15: 3D plot of the power transmission coefficient and diffuse-field STL (air-to-water) of panel 1: (a) heading angle of wave propagation $\phi = 0^\circ$; (b) diffuse-field STL.

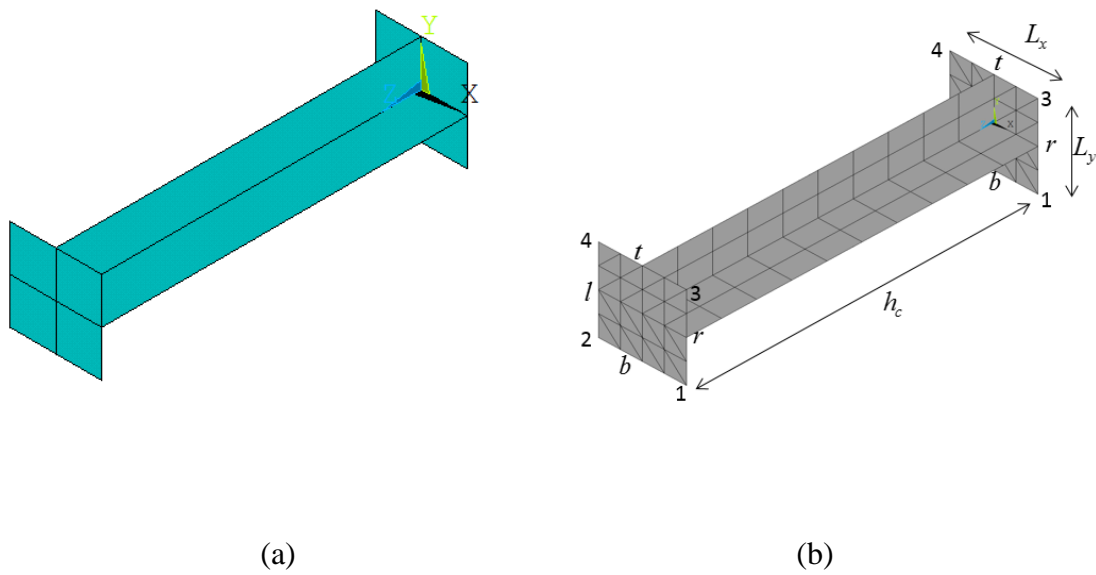


Figure 4.16: Periodic cell and FE model for a honeycomb panel having a rectangular core: (a) a rectangular periodic cell; (b) FE mesh of the rectangular periodic cell with the hypernodes denoted by numbers and alphabets.

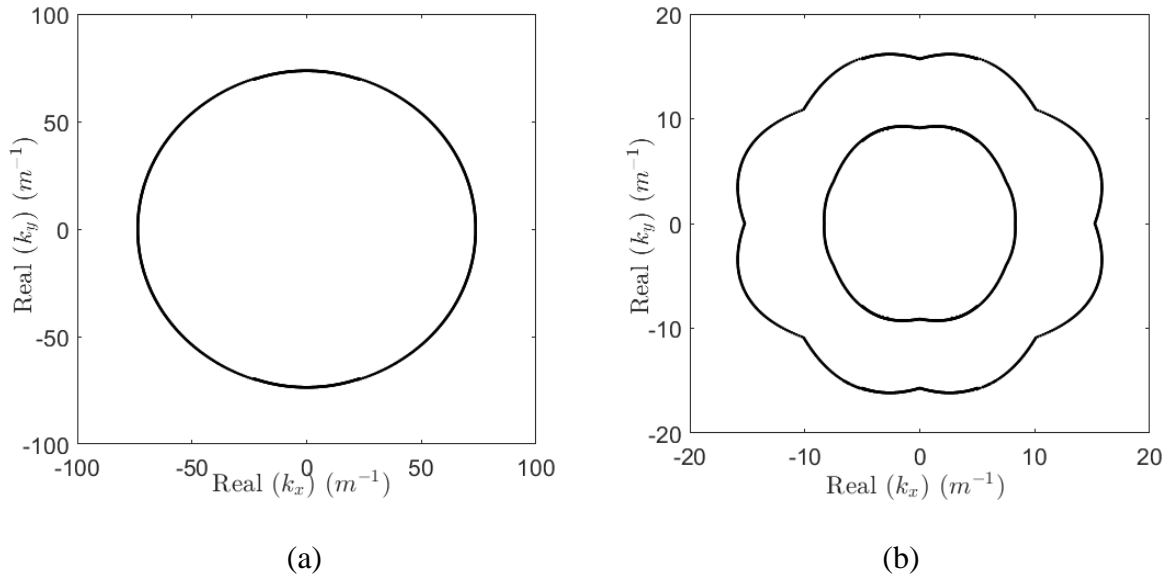


Figure 4.17: Directionality of plane waves predicted by the full WFE model at 6 kHz of panel 3: (a) bending wave; (b) shear wave (outer curve), and extensional wave (inner curve).

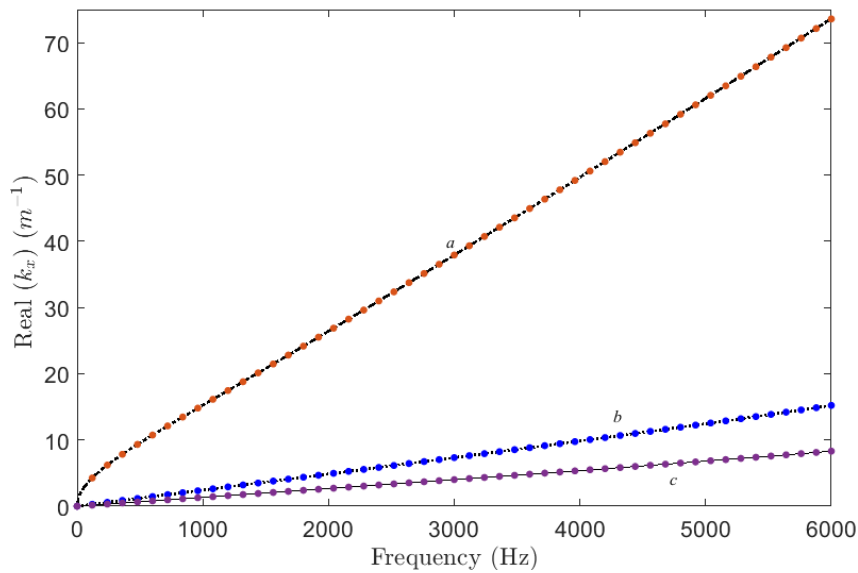


Figure 4.18: Wavenumber comparison of panel 3: using a full WFE model (solid line: extensional wave (branch *c*), dot line: shear wave (branch *b*), dash-dot: bending wave (branch *a*)), and using a reduced WFE model (denoted by round dot).

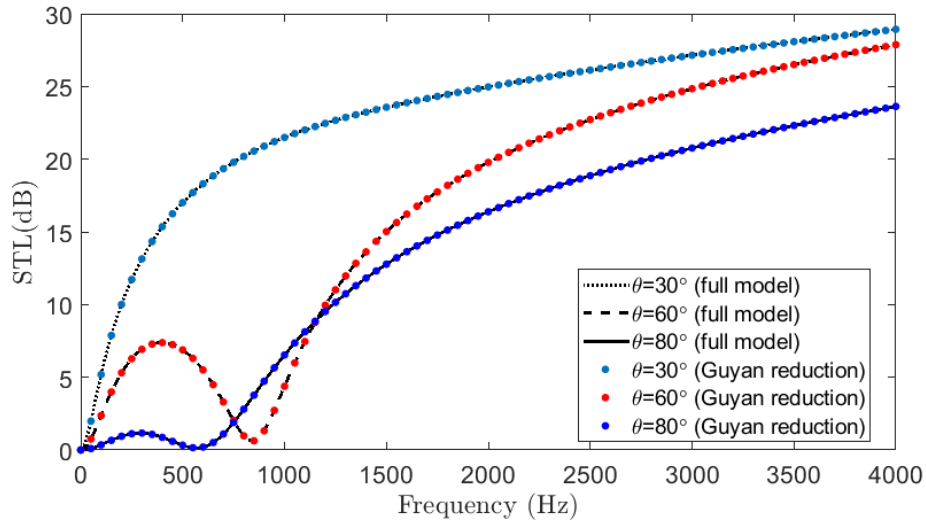


Figure 4.19: Oblique STL for the honeycomb-cored panel with composite skins and a square core (air-to-air, $\phi = 0^\circ$): using a full WFE model and a reduced WFE model made by Guyan reduction.

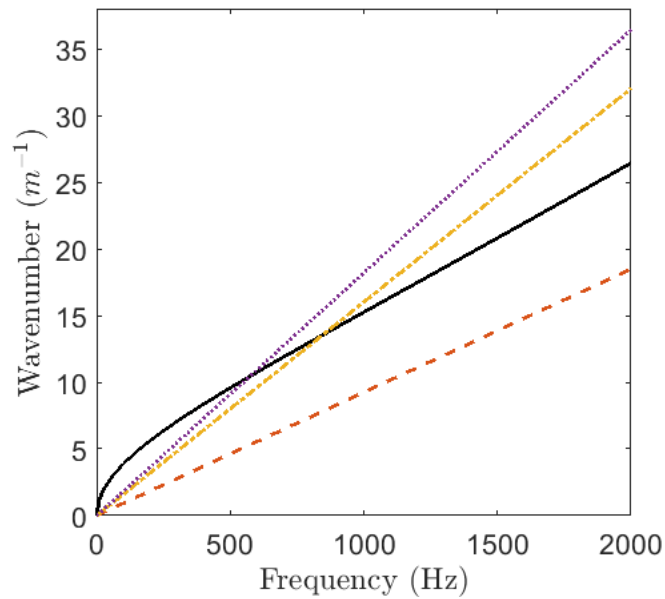


Figure 4.20: Wavenumbers for the bending wave of panel 3 and the acoustic trace waves: solid line (structural bending wave), dash line (acoustic trace wave, $\theta = 30^\circ$), dot line (acoustic trace wave, $\theta = 80^\circ$), dash-dot (acoustic trace wave, $\theta = 60^\circ$).

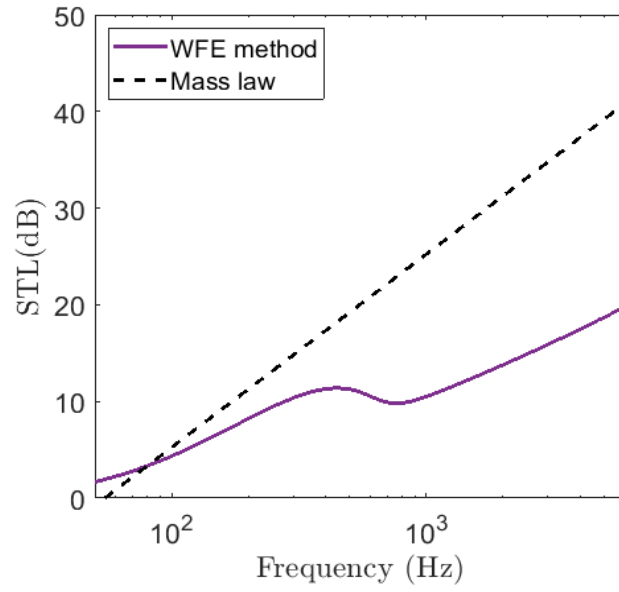


Figure 4.21: Diffuse-field STL (air-to-air): solid line: using a reduced WFE model by Gyan method; dash line: mass law.

Chapter 5

SOUND TRANSMISSION THROUGH TWO DIMENSIONAL CYLINDRICAL SHELLS

This chapter concerns sound transmission through isotropic, uniform, cylindrical shells. For simplicity, the cylinders are modelled as two-dimensional with no variation in the axial direction. The analysis follows similar lines to those in chapters 2-4 for plane structures: the interior and exterior acoustic spaces are modelled analytically, polar coordinates being separable; the structure is modelled using a wave and finite element method, and is assumed to be axisymmetric allowing for the application of periodicity equations in the circumferential direction.

5.1 Introduction

Cylindrical structures are extensively used in engineering applications, e.g. pipes, aircraft fuselages, submarines, etc. Analytical methods are often used for studying the vibroacoustics of such structures. For simple structures (e.g., an infinitely long, thin and isotropic cylindrical shell), establishing an analytical equation of motion is straightforward. However, for more complicated constructions, such as composite materials consisting of many layers having different physical properties (e.g., the cross-ply angles of the materials, physical properties), using analytical methods is difficult.

Although some authors have developed analytical models using formulations for laminated cylindrical shells, typically layer-wise theories, these models involve various

assumptions, e.g. neglecting the transverse shear stress and rotational inertia [8], assuming that the structural wavelength is much larger than the shell thickness, etc. Furthermore, it is difficult to use analytical methods for calculating the dispersion curves of complicated structures, particularly for short waves with large circumferential wavenumbers. There has been some application of numerical methods in the literature (e.g., a FE method [119], a SEA method [100] and a transfer matrix method [78]).

An alternative method developed here is the wave and finite element method. This chapter aims to extend this method to predict sound transmission through cylindrical shells. For simplicity, the infinitely long cylindrical shell is reduced to a circular shell in two dimensions, in effect assuming no spatial variation in the axial direction. Both the analytical and WFE methods are used to predict the forced response of the structure subjected to acoustic excitations. For validating this method, the predictions are compared with analytical results.

5.2 Theory and Formulation

The system considered is shown in figure 5.1, where the infinitely long cylinder is excited by a line source parallel to the axial direction. The interior and exterior fluids are modelled analytically in section 5.2.1. Fourier transforms are used to decompose the acoustic pressures into a sum of space-harmonic components in the circumferential direction. The interactions between the structure and the fluids are modelled in section 5.2.2. The acoustic excitations are modelled using equivalent nodal forces in section 5.2.3. A simple structure is modelled analytically in section 5.2.4 for later validation studies. The WFE model is developed in section 5.2.5. It can be applied to structures with arbitrary cross-sections (e.g., isotropic and laminated shells). In section 5.3, a numerical example is presented and analytical predictions compared with those of the WFE method.

5.2.1 Fluid Spaces

In this section, the pressure field generated by a line mass source is considered. The line source can be located exterior to, or inside the cavity of, the cylindrical shell of thickness h . The acoustic pressure satisfies the equation [11]

$$\nabla^2 p - \frac{1}{c^2} \frac{\partial^2 p}{\partial t^2} = -\rho \frac{\partial q}{\partial t}, \quad (5.1)$$

where $q(r, \phi, t)$ is the strength of the volume flow source within the fluid, and

$$\nabla^2 p = \frac{\partial^2 p}{\partial r^2} + \frac{1}{r} \frac{\partial p}{\partial r} + \frac{1}{r^2} \frac{\partial^2 p}{\partial \phi^2} \quad (5.2)$$

for cylindrical coordinates.

For considering the problem in the frequency domain, the Fourier transform pair

$$\begin{aligned} \tilde{p}(r, \phi, \omega) &= \frac{1}{2\pi} \int_{-\infty}^{+\infty} p(r, \phi, t) \exp(-i\omega t) dt, \\ p(r, \phi, t) &= \int_{-\infty}^{+\infty} \tilde{p}(r, \phi, \omega) \exp(i\omega t) d\omega. \end{aligned} \quad (5.3)$$

is defined. Since time-harmonic motion is assumed, applying the Fourier transform to equation (5.1) gives

$$\nabla^2 \tilde{p} + k^2 \tilde{p} = i\omega \rho_0 \tilde{q}, \quad (5.4)$$

where the acoustic wavenumber $k = \omega/c$.

In the two-dimensional space, the volume source strength

$$q(r, \phi, t) = Q_0(t) \delta(r - r_s) \frac{\delta(\phi - \phi_s)}{r}, \quad (5.5)$$

where $Q_0(t)$ is the volume flow rate per unit length of the line source, and the location of the line source is defined by coordinates (r_s, ϕ_s) ; note that the units of the Dirac delta are the inverse

of those of the arguments r and ϕ . Taking the Fourier transform of equation (5.5) using equation (5.3) leads to

$$\tilde{q}(r, \phi, \omega) = Q_0(\omega) \frac{\delta(r - r_s)}{r} \delta(\phi - \phi_s). \quad (5.6)$$

For solving equation (5.4), it is convenient to define the Fourier transform pair

$$\tilde{p}_n(r, \omega) = \frac{1}{2\pi} \int_0^{2\pi} \tilde{p}(r, \phi, \omega) e^{-in\phi} d\phi, \quad \tilde{p}(r, \phi, \omega) = \sum_{n=-\infty}^{\infty} \tilde{p}_n(r, \omega) e^{in\phi} \quad (5.7)$$

which decomposes the pressure into a sum of space-harmonic components in the azimuthal direction. Applying the Fourier transform of equation (5.7) to equation (5.4) yields

$$\frac{1}{r} \frac{d}{dr} \left(r \frac{d\tilde{p}_n}{dr} \right) + \left(k^2 - \frac{n^2}{r^2} \right) \tilde{p}_n = i\omega\rho_0 Q_0 \frac{\delta(r - r_s)}{2\pi r} e^{-in\phi_s}. \quad (5.8)$$

It is convenient to make the substitution

$$\tilde{p}_n(r, \omega) = \frac{i\omega\rho_0 Q_0}{2\pi} e^{-in\phi_s} Y(r). \quad (5.9)$$

Equation (5.8) can be expressed as

$$\frac{d}{dr} \left(r \frac{dY}{dr} \right) + \left(k^2 r - \frac{n^2}{r} \right) Y = \delta(r - r_s). \quad (5.10)$$

According to appendix 6.B of reference [11], the solution to equation (5.10) is given by

$$Y(r) = -\frac{Y_+(r_>)Y_-(r_<)}{r[Y_+(r_>)Y_-'(r_<) - Y_-(r_<)Y_+'(r_>)]}, \quad (5.11)$$

where $r_>$ is the greater of r and r_s , while $r_<$ is the lesser of r and r_s and Y_+ and Y_- are two linearly independent solutions of the homogeneous form of equation (5.10). They are determined using the boundary conditions as described in the next section.

5.2.2 Fluid-Structure Interaction

The line source can be located inside the cavity of the cylindrical structure (e.g., for modelling the noise radiated from pipes) or exterior to the structure (e.g., for modelling the sound radiation from an exterior source into and aeroplane). Hence in this section, both the fluid spaces inside the cavity and outside the structure are considered.

5.2.2.1 Source Exterior to a Cylinder

For a line source lying exterior to the structure, radial velocity continuity at the interface between the outer surface of the structure and the exterior fluid space leads to

$$\frac{\partial \tilde{p}_n^o(r, \omega)}{\partial r} = \omega^2 \rho_0 \tilde{w}_n^o, \quad (5.12)$$

where \tilde{w}_n^o represents the radial displacement of the outer surface for the n -th circumferential order and ρ_0 denotes the density of the exterior fluid. In equation (5.11), $Y_+(r)$ is expected to satisfy the boundary condition at the outer surface of the structure, and $Y_-(r)$ satisfy the radiation condition as r tends to infinity. Hence, $Y_+(r)$ and $Y_-(r)$ can be expressed as

$$Y_-(r) = J_n(kr) + A_n H_n^{(1)}(kr), \quad Y_+(r) = H_n^{(1)}(kr), \quad (5.13)$$

where $J_n(kr)$ and $H_n^{(1)}$ are Bessel and Hankel functions of the first kind respectively. Substituting equation (5.13) into equation (5.11), and then inserting the result into equation (5.9) gives

$$\tilde{p}_n^o(r, \omega) = \frac{\omega \rho_0 \tilde{Q}_0}{4} H_n^{(1)}(kr_s) [J_n(kr) + A_n H_n^{(1)}(kr)] e^{-in\phi_s}, \quad (5.14)$$

where $r < r_s$, and A_n is an unknown constant. Substituting equation (5.14) into equation (5.12) leads to

$$\tilde{w}_n^o = \frac{k\tilde{Q}_0}{4\omega} H_n^{(1)}(kr_s) [J_n'(kr_0) + A_n H_n^{(1)'}(kr_0)] e^{-in\phi_s}. \quad (5.15)$$

Assuming the normal displacement \tilde{w}_n^o is known, equation (5.15) can be rearranged to give

$$A_n = \frac{4\omega\tilde{w}_n^o e^{in\phi}}{k\tilde{Q}_0 H_n^{(1)}(kr_s) H_n^{(1)'}(kr_0)} - \frac{J_n'(kr_0)}{H_n^{(1)'}(kr_0)}. \quad (5.16)$$

Substituting equation (5.16) into equation (5.14) leads to the pressure exterior to the cylinder,

$$\tilde{p}_n^o(r, \omega) = \tilde{p}_b^o - D_{f,o} \tilde{w}_n^o, \quad (5.17)$$

where the pressure \tilde{p}_b^o , and the dynamic stiffness of the exterior fluid $D_{f,o}$ are

$$\begin{aligned} \tilde{p}_b^o &= \frac{\omega\rho_0\tilde{Q}_0}{4} H_n^{(1)}(kr_s) \left[J_n(kr) - \frac{J_n'(kr_0)}{H_n^{(1)'}(kr_0)} H_n^{(1)}(kr) \right] e^{-in\phi_s}, \\ D_{f,o}^n &= -\frac{\omega^2\rho_0 H_n^{(1)}(kr)}{kH_n^{(1)'}(kr_0)}. \end{aligned} \quad (5.18)$$

Note that the first term in equation (5.17) denotes ‘‘blocked’’ pressure if the structure were rigid, and the second term represents the acoustic pressure caused by the vibration of the surface.

The pressure \tilde{p}_n^i must satisfy

$$\frac{d^2\tilde{p}_n^i}{dr^2} + \frac{1}{r} \frac{d\tilde{p}_n^i}{dr} + \left(k_i^2 - \frac{n^2}{r^2} \right) \tilde{p}_n^i = 0, \quad (5.19)$$

where $k_i = \omega/c_i$ is the acoustic wavenumber of the interior fluid with speed of sound, c_i . Using the boundary condition

$$\frac{\partial\tilde{p}_n^i(r, \omega)}{\partial r} = \omega^2\rho_i\tilde{w}_n^i, \quad (5.20)$$

where \tilde{w}_n^i represents the radial displacement of the interior surface of the structure for the n -th harmonic component, ρ_i denotes the density of the interior fluid.

The solution to equation (5.19) which is finite along the axis of the cylinder is of the form

$$\tilde{p}_n^i = B_n J_n(k_i r), \quad (5.21)$$

where B_n is a constant which is determined by continuity at the inner surface and is given by

$$B_n = \frac{\omega^2 \rho_i \tilde{w}_n^i}{k_i J_n'(k_i r_i)}. \quad (5.22)$$

Inserting equation (5.22) into equation (5.21) yields

$$\tilde{p}_n^i = D_{f,i}^n \tilde{w}_n^i. \quad (5.23)$$

where

$$D_{f,i}^n = \frac{\omega^2 \rho_i J_n(k_i r)}{k_i J_n'(k_i r_i)} \quad (5.24)$$

is the dynamic stiffness of the interior fluid.

5.2.2.2 Source inside a Cylinder

When the source is in the cavity of the cylinder, $Y_-(r)$ is chosen to satisfy the boundary condition at $r=0$ and $Y_+(r)$ to satisfy the boundary condition at $r=r_i$ such that

$$Y_-(r) = J_n(k_i r), \quad Y_+(r) = A_n J_n(k_i r) + H_n^{(1)}(k_i r), \quad (5.25)$$

where A_n is an unknown constant which is yet to be determined. Substituting equation (5.25) into equation (5.11), and then inserting the result into equation (5.9) give

$$\tilde{p}_n^i(r, \omega) = \frac{i\omega\rho_i\tilde{Q}_0}{4} J_n(k_i r_s) [A_n J_n(k_i r) + H_n^{(1)}(k_i r)] e^{-in\phi_s}. \quad (5.26)$$

The boundary condition on the interior surface requires that the acoustic particle velocity is equal to the radial velocity of the inner surface of the cylinder. Inserting equation (5.26) into equation (5.20) gives

$$A_n = \frac{-4i\omega e^{in\phi} \tilde{w}_n^i}{k\tilde{Q}_0 J_n(k_i r_s) J_n'(k_i r_i)} - \frac{H_n^{(1)'}(k_i r_i)}{J_n'(k_i r_i)}. \quad (5.27)$$

The acoustic pressure inside the cylinder can be obtained by substituting equation (5.27) into equation (5.26), i.e.

$$\tilde{p}_n^i(r, \omega) = \tilde{p}_b^i + D_{f,i}^n \tilde{w}_n^i, \quad (5.28)$$

where the pressure \tilde{p}_b^i , and the fluid dynamic stiffness $D_{f,i}^n$ can be written as

$$\begin{aligned} \tilde{p}_b^i &= \frac{i\omega\rho_i\tilde{Q}_0}{4} J_n(k_i r_s) \left[H_n^{(1)}(k_i r) - \frac{H_n^{(1)'}(k_i r_i)}{J_n'(k_i r_i)} J_n(k_i r) \right] e^{-in\phi}, \\ D_{f,i}^n &= \frac{\omega^2 \rho_i J_n(k_i r)}{k_i J_n'(k_i r_i)}. \end{aligned} \quad (5.29)$$

Again the first term indicates the blocked pressure by a rigid shell. The second term represents the contribution of the vibration of the surface. For the acoustic field outside the cylinder, the acoustic pressure \tilde{p}_n^o must satisfy

$$\frac{d^2 \tilde{p}_n^o}{dr^2} + \frac{1}{r} \frac{d\tilde{p}_n^o}{dr} + \left(k_o^2 - \frac{n^2}{r^2} \right) \tilde{p}_n^o = 0 \quad (5.30)$$

which is subjected to the boundary condition as equation (5.2), and a radiation condition as r becomes infinitely large. Consequently, the solution to equation (5.30) is

$$\tilde{p}_n^o(r, \omega) = B_n H_n^{(1)}(k_o r), \quad (5.31)$$

where from continuity at the inner surface

$$B_n = \frac{\omega^2 \rho_o \tilde{W}_n^o}{k_o H_n^{(1)'}(k_o r_o)}. \quad (5.32)$$

Substituting equation (5.32) into equation (5.31) gives

$$\tilde{P}_n^o(r, \omega) = -D_{f,o}^n \tilde{W}_n^o, \quad (5.33)$$

where the fluid dynamic stiffness is expressed as

$$D_{f,o}^n = -\frac{\omega^2 \rho_o H_n^{(1)}(k_o r)}{k_o H_n^{(1)'}(k_o r_o)}. \quad (5.34)$$

5.2.3 Analytical Model and Responses

In this section, the analytical model is used to model the structure. The analytical model is only valid for thin, isotropic cylindrical shells.

There are various theories for establishing the equations of motion for cylindrical structures e.g. Sanders's theory, Reissner's theory, etc. [6]. Different theories have different assumptions. For example, the assumptions of Love's model are: the thickness of the shell is very small compared with other dimensions; higher-order terms in the strain-displacement relations are neglected; the transverse normal and shear stresses are negligible. In this chapter, the Flugge-Byrne-Lur'ye theory [6] is used. In the following equations, the transverse normal and shear stresses are both considered,

$$-\frac{Eh}{R^2(1-\nu^2)} \frac{\partial^2 w_\phi}{\partial \phi^2} - \frac{Eh}{R^2(1-\nu^2)} \frac{\partial w_r}{\partial \phi} + \rho_s h \frac{\partial^2 w_\phi}{\partial t^2} = 0 \quad (5.35)$$

$$\begin{aligned} \frac{Eh}{R^2(1-\nu^2)} \frac{\partial w_\phi}{\partial \phi} + \left[\frac{Eh}{R^2(1-\nu^2)} + \frac{Eh^3}{12R^4(1-\nu^2)} \right] w_r + \frac{Eh}{6R^4(1-\nu^2)} \frac{\partial^2 w_r}{\partial \phi^2} \\ + \frac{Eh^3}{12R^4(1-\nu^2)} \frac{\partial^4 w_r}{\partial \phi^4} + \rho_s h \frac{\partial^2 w_r}{\partial t^2} = p_n, \end{aligned} \quad (5.36)$$

where p_n is the total pressure acting on the shell mean-surface (which is assumed to act in the radial direction), E is Young's modulus, ν is Poisson's ratio, w_ϕ is the displacement of the shell mean-surface in the ϕ -direction and w_r is the displacement of the shell mean-surface in the r -direction.

Applying Fourier transform to the Flugge-Byrne-Lur'ye equations yields

$$-\frac{Ehn^2}{R^2(1-\nu^2)}\tilde{w}_{\phi,n} - \frac{iEhn}{R^2(1-\nu^2)}\tilde{w}_{r,n} + \rho_s h \tilde{w}_{\phi,n} = 0, \quad (5.37)$$

$$\begin{aligned} & \frac{iEh}{R^2(1-\nu^2)}\tilde{w}_{\phi,n} \\ & + \left[\frac{Eh^3n^4}{12R^4(1-\nu^2)} - \frac{Ehn^2}{6R^4(1-\nu^2)} + \frac{Eh^3}{12R^4(1-\nu^2)} + \frac{Eh}{R^2(1-\nu^2)} - \rho_s h \omega^2 \right] \tilde{w}_{r,n} = \tilde{p}_n. \end{aligned} \quad (5.38)$$

It is assumed that the velocities of the inner and outer surfaces of the cylinder are equal to the radial velocity of the shell mean-surface, e.g. $\tilde{v}_n^i = \tilde{v}_n^o = -i\omega\tilde{w}_{r,n}$. Substituting equation (5.50) into equation (5.38) yields the following system of equations which describes the Fourier transform of the response of the thin cylindrical shell to the acoustic field produced by the line mass source.

$$\begin{bmatrix} A & B \\ C & D \end{bmatrix} \begin{bmatrix} \tilde{w}_{\phi,n} \\ \tilde{w}_{r,n} \end{bmatrix} = \begin{bmatrix} 0 \\ E \end{bmatrix}, \quad (5.39)$$

$$A = \frac{Ehn^2}{R^2(1-\nu^2)} - \rho_s h \omega^2, \quad B = -\frac{iEhn}{R^2(1-\nu^2)}, \quad C = \frac{iEhn}{R^2(1-\nu^2)}, \quad (5.40)$$

$$\begin{aligned} D &= \frac{Eh^3n^4}{12R^4(1-\nu^2)} - \frac{Ehn^2}{6R^4(1-\nu^2)} + \frac{Eh^3}{12R^4(1-\nu^2)} + \frac{Eh}{R^2(1-\nu^2)} - \rho_s h \omega^2 \\ & - (D_{f,i}^n + D_{f,o}^n), \end{aligned} \quad (5.41)$$

$$E = -\frac{\omega\rho_0\tilde{Q}_0}{4}H_n^{(1)}(kr_s)\left[J_n(kr_o) - \frac{J_n'(kr_o)}{H_n^{(1)'}(kr_o)}H_n^{(1)}(kr_o)\right]. \quad (5.42)$$

The equations can be solved to find $\tilde{w}_{r,n}$ and $\tilde{w}_{\phi,n}$ which can then be used in equation (5.17) and equation (5.23) to calculate the acoustic pressures exterior to, and interior to, the cylinder. Note that in many cases (usually when the acoustic mediums have low densities relative to the density of the cylindrical shell), it is expected that the loading on the structure due to the acoustic pressures produced by its vibration may be neglected. This can be done by setting the fluid dynamic stiffnesses zero.

5.2.4 The WFE Model and Responses

In this section, the WFE method is extended to calculate the response of the cylindrical shell to the excitation of the parallel line source. The modelling follows the line described in chapter 2.

5.2.4.1 FE Modelling of a Curved Segment

The curved structure can be modelled using several methods [65, 66, 98]. Here, small flat elements are used to model the curvature of the structure since curved elements are not available in available commercial software. In particular, this modelling uses a single ANSYS SHELL 181 element of dimensions $L_x \times L_y$ where $L_x = R\Delta\phi$ and L_y is the length of the segment along the cylinder axis and $\Delta\phi$ denotes the subtended angle of the element in the circumferential direction which is assumed to be small enough. The rectangular element has four nodes, and six DOFs at each node: translations in the nodal x , y and z directions and rotations about the nodal x , y and z axes. For modelling the structural motion in the x - y plane, the translational and rotational DOFs about the z -axis are set to be zeros. The vector of nodal DOFs of the element (illustrated in figure 2) can be partitioned as

$$\mathbf{q} = \left[\mathbf{q}_1^T \quad \mathbf{q}_2^T \quad \mathbf{q}_3^T \quad \mathbf{q}_4^T \right]^T, \quad (5.43)$$

where the superscript “T” denotes transposition and the subscripts “1”, “2”, “3”, “4”, correspond to corner nodes. The vector of internal nodal forces, \mathbf{f} , and external nodal forces, \mathbf{e} , are partitioned in the same manner.

For modelling the curvature of the structure, the nodal coordinates of the nodes of the flat element are rotated around the y -axis by an angle $\Delta\phi$. Hence the FE matrices of the flat element with nodal coordinates rotated are

$$\tilde{\mathbf{M}} = \mathbf{R}^T \mathbf{M} \mathbf{R}, \quad \tilde{\mathbf{K}} = \mathbf{R}^T \mathbf{K} \mathbf{R}, \quad (5.44)$$

where \mathbf{M} and \mathbf{K} are the mass and stiffness matrices of the original shell element, the rotation matrix, \mathbf{R} , can be written as

$$\mathbf{R} = \begin{bmatrix} \mathbf{I} & \mathbf{0} & \mathbf{0} & \mathbf{0} \\ \mathbf{0} & \bar{\mathbf{R}} & \mathbf{0} & \mathbf{0} \\ \mathbf{0} & \mathbf{0} & \mathbf{I} & \mathbf{0} \\ \mathbf{0} & \mathbf{0} & \mathbf{0} & \bar{\mathbf{R}} \end{bmatrix}, \quad (5.45)$$

where $\bar{\mathbf{R}}$ allows the rotation of the hyper-nodes with number “2” and “4”, \mathbf{I} , $\mathbf{0}$, and, $\bar{\mathbf{R}}$, are matrices of order equal to the number of DOFs of the corresponding hyper-nodes in the FE model. \mathbf{I} is an identity matrix, $\mathbf{0}$ is a matrix of zeros and $\bar{\mathbf{R}}$ is defined as

$$\bar{\mathbf{R}} = \begin{bmatrix} \cos(\Delta\phi) & 0 & -\sin(\Delta\phi) & 0 & 0 & 0 \\ 0 & 1 & 0 & 0 & 0 & 0 \\ \sin(\Delta\phi) & 0 & \cos(\Delta\phi) & 0 & 0 & 0 \\ 0 & 0 & 0 & \cos(\Delta\phi) & 0 & -\sin(\Delta\phi) \\ 0 & 0 & 0 & 0 & 1 & 0 \\ 0 & 0 & 0 & \sin(\Delta\phi) & 0 & \cos(\Delta\phi) \end{bmatrix}. \quad (5.46)$$

The forced equation of motion of the flat element can be written as

$$[\tilde{\mathbf{K}} - \omega^2 \tilde{\mathbf{M}}] \mathbf{q} = \mathbf{f} + \mathbf{e}. \quad (5.47)$$

For modelling the curved structure in two-dimensions, the shell element needs be degenerated into one-dimensional straight elements by setting $\mathbf{q}_1 = \mathbf{q}_3$, and $\mathbf{q}_2 = \mathbf{q}_4$ such that equation (5.51) becomes

$$[\bar{\mathbf{K}} - \omega^2 \bar{\mathbf{M}}] \bar{\mathbf{q}} = \mathbf{C}^T \mathbf{f} + \mathbf{C}^T \mathbf{e}, \quad (5.48)$$

where $\bar{\mathbf{M}}$ and $\bar{\mathbf{K}}$ are the mass and stiffness matrices after the degeneration, \mathbf{C}^T is the transformation matrix, $\bar{\mathbf{q}}$ is the DOFs vector of the degenerated element. They can be written as

$$\bar{\mathbf{K}} = \mathbf{C}^T \tilde{\mathbf{K}} \mathbf{C}, \quad \bar{\mathbf{M}} = \mathbf{C}^T \tilde{\mathbf{M}} \mathbf{C}, \quad \bar{\mathbf{q}} = [\mathbf{q}_1^T \quad \mathbf{q}_2^T], \quad \mathbf{C} = \begin{bmatrix} \mathbf{I} & \mathbf{0} & \mathbf{I} & \mathbf{0} \\ \mathbf{0} & \mathbf{I} & \mathbf{0} & \mathbf{I} \end{bmatrix}^T. \quad (5.49)$$

5.2.4.2 Acoustic Excitations

The acoustic pressures generated on the outer and inner surfaces of the cylinder subjected to the excitation by a line source have been described in section 5.2.2. The equivalent nodal forces are found in this section.

For a source exterior to the cylinder, the total pressure applied to the outer-surface of the cylindrical shell can be written as (using equation (5.17) and equation (5.23))

$$\tilde{p}_n(r, \omega) = \tilde{p}_b^o + D_{f,i}^n \tilde{w}_n^i + D_{f,o}^n \tilde{w}_n^o, \quad (5.50)$$

where $r = R + h/2$ is the radius of the outer surface. For a source inside the cavity of the cylinder (using equation (5.28) and equation (5.33)),

$$\tilde{p}_n(r, \omega) = \tilde{p}_b^i + D_{f,i}^n \tilde{w}_n^i + D_{f,o}^n \tilde{w}_n^o, \quad (5.51)$$

where $r = R - h/2$ is the radius of the inner surface.

It can be seen that equation (5.50) and equation (5.51) explicitly separate the excitation into two parts, i.e. the “blocked” pressure and the fluid loadings. In the FE discretisation, these

acoustic pressures are modelled using equivalent external nodal forces. Using the notation in chapter 2, the nodal force for j -th hyper-node of the FE model of a small curved segment of the structure can be written as

$$\mathbf{e}_j = (\tilde{p}_n^o \mathbf{u}_1 - \tilde{p}_n^i \mathbf{u}_2) \alpha_j, \quad (5.52)$$

where the coefficient α_j is preferably calculated as a consistent nodal force, but may be approximated using lumped forces, i.e.

$$\alpha_j = \iint_{S_j} e^{-in\phi} dx dy \quad (5.53)$$

where the integration area associated with the j -th hyper-node is denoted by S_j .

5.2.4.3 Spectral Dynamic Stiffness Matrix and Responses

Now, applying the periodicity condition in the circumferential direction leads to $\mathbf{q}_2 = \lambda_x \mathbf{q}_1$, where the wave propagation constant $\lambda_x = \exp(-in\Delta\phi)$. Considering the equilibrium at hyper-node 1 (similar to equation (2.33)), the following equation can be obtained, i.e.

$$\mathbf{D}_s \mathbf{q}_1 = \Lambda^H \mathbf{C}^T \mathbf{e}, \quad \mathbf{D}_s = \Lambda^H [\bar{\mathbf{K}} - \omega^2 \bar{\mathbf{M}}] \Lambda, \quad \Lambda = [\mathbf{I} \quad \lambda_x \mathbf{I}]^T, \quad (5.54)$$

where superscript ‘‘H’’ denotes the conjugate transpose. Substituting equation (5.52) into equation (5.54) gives

$$\mathbf{D} \mathbf{q}_1 = \tilde{p}_b \varepsilon \mathbf{u}_1, \quad (5.55)$$

where the total spectral dynamic stiffness matrix, \mathbf{D} , and the coefficient, ε , can be expressed as

$$\begin{aligned} \mathbf{D} &= \mathbf{D}_s + \varepsilon D_{f,o}^n \mathbf{u}_1 \mathbf{u}_1^T + \varepsilon D_{f,i}^n \mathbf{u}_2 \mathbf{u}_2^T, \\ \varepsilon &= \alpha_1 + e^{in\Delta\phi} \alpha_2 + \alpha_3 + e^{in\Delta\phi} \alpha_4, \end{aligned} \quad (5.56)$$

Once the displacement vector, \mathbf{q}_1 , is calculated from equation (5.55), the acoustic pressures can be found from equation (5.17) and equation (5.23) for the case of source exterior to the cylinder.

5.3 Illustrative examples

In this section, the WFE method is used to calculate the structural response and radiated pressures from a 2-dimensional cylinder excited by sound from an acoustic line source. The cylinder has a density of 7800kg/m^3 , a Young's modulus of $2 \times 10^{11}\text{Pa}$, Poisson's ratio 0.2, and mean-surface radius 0.3m and a thickness of 1.8mm. The fluids interior and exterior to the cylinder have density 1000kg/m^3 . The line source is located at a radius of 0.4m and has a strength of $1\text{m}^2/\text{s}$.

A small curved segment of the structure is modelled using a degenerated shell element. In the degeneration, the translation and rotation about the z -axis are constrained and the transformation matrix \mathbf{C} is used to find the equivalent mass and stiffness matrices of the degenerated element. The results are compared with the results of calculations made using the analytic model of section 5.2.3.

Figure 5.3 plots the magnitude of the radial displacement of the shell, $\tilde{w}_{r,n}$, against frequency for four different values of n . The agreement between the WFE method and the analytical solution is excellent. Figure 5.4 plots the magnitude of the acoustic pressure against radius using the structural response calculated using the WFE method. It can be seen that the pressure amplitude in the structure increases with radius until a discontinuity occurring at $r=R$.

5.4 Conclusions

In this chapter, sound transmission through two-dimensional cylindrical structure was studied. The acoustic excitation can be arbitrary. A line source, which can be located inside the cavity

of the cylinder or exterior to the structure, was considered. The sound pressures in the fluid spaces are modelled analytically.

A thin, isotropic cylindrical structure was considered using an analytical model and a WFE method. The equations developed for the WFE model for the simple cylinder can be applied to arbitrary complex cylinders. Note that it is difficult to develop analytical models for complicated structures. For the WFE model, the acoustic excitation is modelled by using equivalent external nodal forces. By post-processing the mass and stiffness matrices of a small segment of the structure using periodicity theory and equilibrium conditions, a fluid-structure coupled model is developed. A total spectral dynamic stiffness matrix is found in the wavenumber domain for calculating the structural response to acoustic excitations.

An illustrative example is presented to validate the WFE model. The agreement between the WFE prediction and the analytical results is excellent. The WFE method is straightforward and valuable for complex structures.

In next chapter, this method will be extended to three-dimensional cylindrical shells and applied to more complicated structures (e.g. thick cylindrical shells, and various laminated cylindrical shell).

Figures

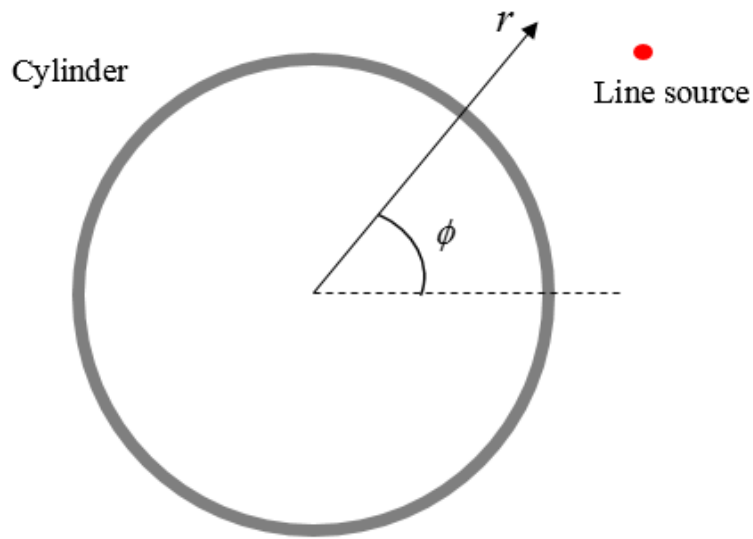


Figure 5.1: Schematic showing a cylinder with an exterior line source.

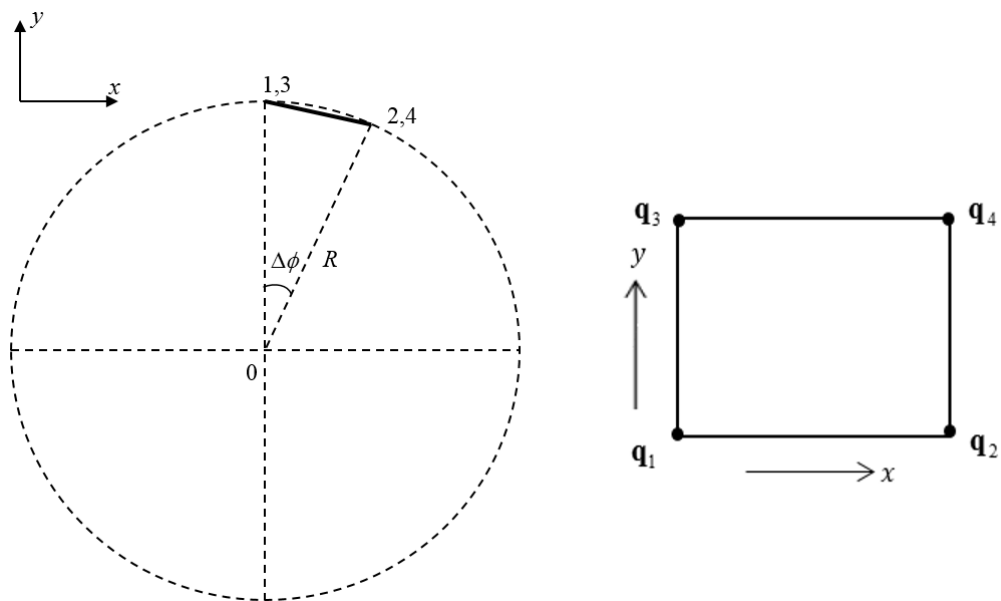


Figure 5.2: Modelling of the curved structure in two-dimensions using equivalent one-dimensional elements.

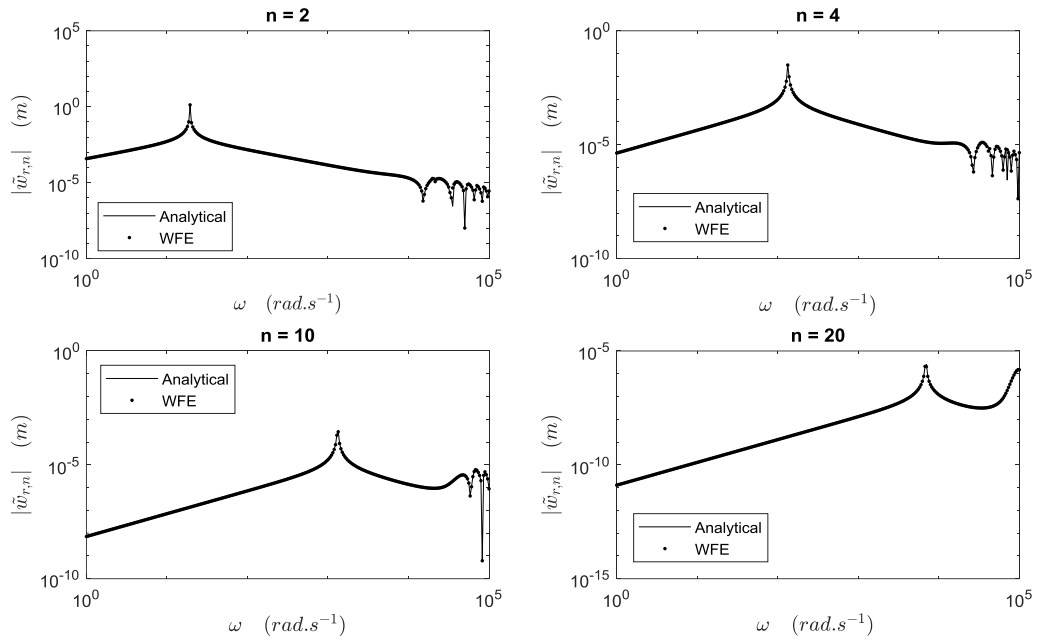


Figure 5.3: Magnitude of the radial displacement.

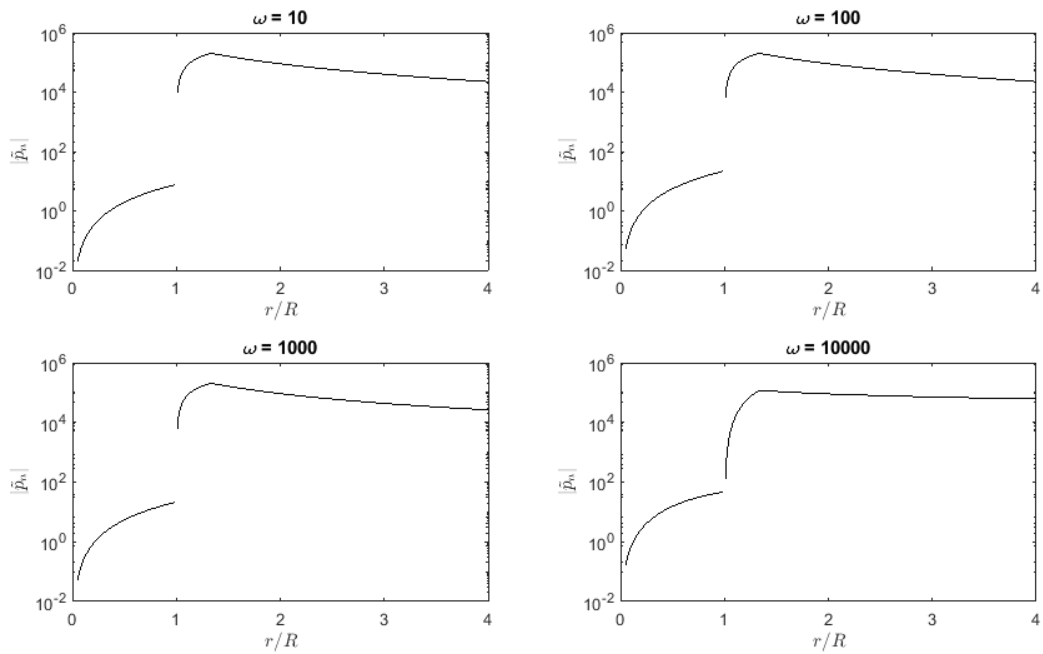


Figure 5.4: Magnitude of the pressure.

Chapter 6

SOUND TRANSMISSION THROUGH THREE DIMENSIONAL CYLINDRICAL SHELLS

This chapter closely follows chapter 5. A general WFE model is developed for three-dimensional, circular cylindrical shells. Sound transmission through, and radiation from various cylindrical shells with different configurations are considered.

6.1 Introduction

This chapter extends the analysis presented in chapter 5 to three-dimensional infinite cylinders. Again a Fourier transform method is used to decompose the applied acoustic or structural loading into wave components. The extended WFE method is then applied and the inverse transform used to determine the total structural response and radiated sound pressure.

There are several analytical models developed for predicting the vibroacoustic performance of cylindrical shells. For example, Koval presented analytic models for calculating the sound transmission of an oblique incident plane wave into orthotropic [62] and also laminated composite [63], infinite cylindrical shells. Unlike here, the internal sound field was modelled as non-resonant (with only inward propagating waves). Blaise and Lesueur also presented analytical models for calculating the sound transmission into orthotropic [66], 2D orthotropic multi-layered [65] and 3-D orthotropic multi-layered cylindrical shells [67, 68]. Ghinet *et al.* [70] extend this work further and present two analytical models for calculating the diffuse-field transmission loss of infinite, laminated composite cylindrical shells.

In addition to these analytic approaches, a number of numerical methods exist for calculating sound transmission through complex cylindrical structures. Examples of these include Cotoni *et al.* [98] and Chronopoulos *et al.* [99]. Cotoni *et al.* describe a method for efficiently calculating the vibroacoustic response of structures (including cylindrical shells) using a hybrid SEA approach where an FE model of a segment of the structure is analysed using periodicity theory to obtain the required SEA properties for the entire structure. The number of internal degrees of freedom of the FE model is reduced using component mode synthesis. Chronopoulos *et al.* present a model for calculating the vibroacoustic performance of composite shells of various geometries for use in an SEA model. The dispersion characteristics of the panel are calculated using the WFE method and this information is used to calculate the vibroacoustic response of the panel within an SEA approach.

An alternative method is the WFE method, developed here, where an FE model of only a small segment of the structure is used. The structural and acoustic responses to structural or acoustic excitation can be found readily by postprocessing the mass and stiffness matrices for this segment using the periodicity and equilibrium conditions.

6.2 Theory and Formulation

In section 6.2.1, analytical equations are presented for modelling the interior and exterior acoustic fields. The interactions between the acoustic fluids and the structure are studied in section 6.2.1.1 and section 6.2.1.2. Excitation can arise from acoustic sources or structural excitation. The sound pressures on the surfaces of the structure are described analytically. The FE discretisation leads to equivalent nodal forces being applied to the model. The WFE method is presented in section 6.2.2 to model the cylindrical shell. An analytical model is presented in section 6.2.2.1 for calculating the vibroacoustic response of a thin cylindrical shell made from a homogeneous, isotropic material for later verification of the WFE results. In section 6.3, several illustrative examples are used to demonstrate the method. The results of calculations

using both the analytical model and the WFE method are compared and shown to be in excellent agreement, verifying the implementation. The usefulness of the WFE method is then demonstrated by analysing the response of a number of complicated cylindrical structures in section 6.4 for which analytical models are not readily available.

6.2.1 Fluid Spaces

Consider the infinite cylinder shown in figure 6.1. The axis of symmetry of the structure is the y -axis. Assume that the structure is filled and surrounded by acoustic fluids. The location of the outer and inner surfaces of the cylinder are denoted by $r = r_o$ and $r = r_i$, and the thickness of the cylindrical shell is h with mean surface radius $r = R$. The subscripts “ i ” and “ o ” denote the inner and outer surfaces. The displacements are represented by w_y, w_r and w_ϕ in the axial, radial and azimuthal directions respectively. Time-harmonic motion of the form $\exp(-i\omega t)$ is assumed. The structure can be excited by an exterior source, an interior source or stresses applied to the inner and/or outer surfaces of the cylinder.

6.2.1.1 Interior Acoustic Field

Assume that there are no acoustic sources inside the cavity of the vibrating cylinder, the acoustic pressures within the cavity must satisfy the Helmholtz equation (see chapter 1 of reference [7])

$$\left[\frac{\partial^2}{\partial r^2} + \frac{1}{r} \frac{\partial}{\partial r} + \frac{1}{r^2} \frac{\partial^2}{\partial \phi^2} + \frac{\partial^2}{\partial y^2} + k_i^2 \right] p = 0, \quad r < r_i \quad (6.1)$$

where $k_i = \omega/c_i$ is the acoustic wavenumber inside the cavity. It is convenient to define the Fourier transform pair

$$\tilde{p}(k_y, r, n) = \frac{1}{4\pi^2} \int_0^{2\pi} \int_{-\infty}^{\infty} p(y, r, \phi) \exp(-ik_y y - in\phi) dy d\phi \quad (6.2)$$

$$p(y, r, \phi) = \sum_{n=-\infty}^{\infty} \int_{-\infty}^{\infty} \tilde{p}(k_y, r, n) \exp(ik_y y + in\phi) dk_y. \quad (6.3)$$

Applying the Fourier transform to equation (6.1) yields

$$\left[\frac{d^2}{dr^2} + \frac{1}{r} \frac{d}{dr} + k_{r,i}^2 - \frac{n^2}{r^2} \right] \tilde{p} = 0, \quad r < r_i \quad (6.4)$$

where $k_{r,i} = \sqrt{k_i^2 - k_y^2}$ is the radial wavenumber.

The solution to equation (6.4) has the same form as equation (5.21) with k_i replaced by $k_{r,i}$, subjected to finite pressures along the axis of the cylinder. Again, the constant B_n is determined by the continuity of particle displacement in the radial direction on the inner surface of the cylinder. Consequently, the solution can be written as

$$\tilde{p}(k_y, r, n) = \frac{\rho_i \omega^2 \tilde{w}_{r,i}(k_y, n) J_n(k_{r,i} r)}{k_{r,i} J'_n(k_{r,i} r_i)} \quad (6.5)$$

On the inner surface of the cylinder, the sound pressure $\tilde{p}_{i,v}$ can be expressed as

$$\tilde{p}_{i,v}(k_y, n) = -D_{f,i} \tilde{w}_{r,i}(k_y, n), \quad (6.6)$$

where the subscript “v” is used to represent the pressure due to the vibrating shell, and

$$D_{f,i} = -\frac{\rho_i \omega^2 J_n(k_{r,i} r_i)}{k_{r,i} J'_n(k_{r,i} r_i)}, \quad (6.7)$$

is the spectral dynamic stiffness of the interior fluid.

Note that the pressure \tilde{p}_i is singular when $J'_n(k_{r,i} r_i) = 0$. This suggests infinite fluid loading at the natural frequencies of the rigid-walled cylindrical cavity. In practice, the fluid loading is limited due to the dissipation mechanism. Damping can be included by making the

speed of sound c_i complex, i.e. $c_i(1+in_f)$, with a small imaginary part. In the numerical examples of this chapter, $n_f = 0.001$ is used.

The structure can also be excited by a sound source within the cavity of the cylinder. In this case, the “blocked” pressure – that is the pressure of the incident wave plus the pressure produced by the scattered field from a geometrically identical, rigid cylinder – should be added to the pressure produced by the cylinder vibration to obtain the total acoustic field and total normal stress acting on the inner surface of the cylinder.

Similar analysis has been made for two-dimensional cylindrical shells in chapter 5. The total acoustic pressures can be found in equation (5.51) to be a sum of the “blocked” pressure and the pressures due to structural vibrations for the case of the sound source located inside the cavity of the structure.

6.2.1.2 Exterior Acoustic Field

A similar analysis to that presented in the previous section can be made for the radiated sound pressure caused by the vibration of the outer surface of the cylinder $r \geq r_o$. The sound pressure exterior to the cylinder can be expressed as

$$\tilde{p} = \frac{\rho_o \omega^2 \tilde{w}_{r,o}}{k_{r,o}} \frac{H_n^{(1)}(k_{r,o} r)}{H_n^{(1)'}(k_{r,o} r)}, \quad (6.8)$$

where $k_{r,o} = \sqrt{k_o^2 - k_y^2}$ is the wavenumber component in the radial direction, and $H_n^{(1)}$ is the Hankel function of the first kind of order n .

Similar to before, the Fourier transform of the pressure on the outer surface can be written as

$$\tilde{p}_{o,v} = D_{f,o} \tilde{w}_{r,o}, \quad (6.9)$$

where

$$D_{f,o} = \frac{\rho_o \omega^2}{k_{r,o}} \frac{H_n^{(1)}(k_r r_o)}{H_n^{(1)'}(k_r r_o)}, \quad (6.10)$$

is the spectral dynamic stiffness of the exterior fluid.

Again, the expressions (equation (6.8) and equation (6.9)) are for the acoustic pressures caused by the vibration of the outer surface of the cylinder. In the case of an incident acoustic wave generated by a sound source located outside of the cylinder. The blocked pressure should be added to the pressure caused by the forced vibration of the outer surface for obtaining the total acoustic field and total normal stress acting on the outer surface of the cylinder.

Similar to equation (5.18), the amplitude of the blocked pressure for a time-harmonic point source with energy strength $Q_0 \text{ m}^3/\text{s}$ can be written as

$$\tilde{P}_{b,o}(r, \omega) = -\frac{\rho_o \tilde{Q}_0 \omega}{8\pi} H_n^{(1)}(k_{r,o} r_s) \left[J_n(k_{r,o} r_o) - \frac{J_n'(k_{r,o} r_o)}{H_n^{(1)'}(k_{r,o} r_o)} H_n^{(1)}(k_{r,o} r_o) \right] \quad (6.11)$$

where r_s represents the radial location of the sound source, and $r_s > r_o$.

6.2.2 Solid Structure

In this part, the cylinder structure is modelled using both the WFE method and an analytical method (for a thin, and isotropic cylinder). The analytical formulation is for verifying the WFE model developed in the next section. Note that using an analytical method is difficult for complicated cylinders.

6.2.2.1 Analytical Model

There are various theories (e.g. Donnel-Mushrai-Vlasove equation [60], and Love's equation [6]) available for modelling the dynamics of cylindrical shells. Different theories have different assumptions for the analytical models. For example, the in-plane motion is completely

neglected in Donnel-Mushrai-Vlasove's theory. The transverse shear forces are not considered in Mindlin-Reissner's plate theory [60]. For considering the in-plane, out-of-plane and shear forces, Flugge, Byrne, Lur'ye's shell theory [6] is used in this section.

Consider a thin ($w_r = w_{r,o} = w_{r,i}$), isotropic cylinder of thickness h and density ρ_s , which has displacements in the axial, w_y , radial, w_r , and tangential, w_ϕ , directions which are described by an equation of motion of the form (see section 2.2 of reference [6])

$$\left[\mathbf{L} - \rho_s h \omega^2 \mathbf{I} \right] \begin{bmatrix} w_y \\ w_\phi \\ w_r \end{bmatrix} = \begin{bmatrix} 0 \\ 0 \\ p_s \end{bmatrix} \quad (6.12)$$

where \mathbf{L} is the partial differential operator matrix and the total external radial pressure applied on the mean surface is denoted by p_s . Taking the Fourier transform of equation (6.12) and making use of equations (6.6) and (6.8), the following fluid-structure coupled equation of motion can be found for each harmonic wave.

$$\left[\tilde{\mathbf{L}} - \rho_s h \omega^2 \mathbf{I} + (D_{f,i} + D_{f,o}) \right] \begin{bmatrix} 0 & 0 & 0 \\ 0 & 0 & 0 \\ 0 & 0 & 1 \end{bmatrix} \begin{bmatrix} \tilde{w}_y \\ \tilde{w}_\phi \\ \tilde{w}_r \end{bmatrix} = \begin{bmatrix} 0 \\ 0 \\ \tilde{p}_{b,o} \end{bmatrix} \quad (6.13)$$

where $\tilde{p}_{b,o}$ is the Fourier transform of the blocked pressure. For the Flugge Byrne Lur'ye model, the components of $\tilde{\mathbf{L}}$ are

$$\begin{aligned}
\tilde{L}_{1,1} &= \left(k_y^2 + \frac{n^2(1-\nu)}{2R^2} + \frac{(1-\nu)h^2n^2}{24R^4} \right) \frac{Eh}{(1-\nu^2)} \\
\tilde{L}_{1,2} &= \left(\frac{k_y n(1+\nu)}{2R} \right) \frac{Eh}{(1-\nu^2)} \\
\tilde{L}_{1,3} &= \left(-\frac{ik_y \nu}{R} - \frac{ik_y^3 h^2}{12R} + \frac{ik_y(1-\nu)h^2 n^2}{24R^3} \right) \frac{Eh}{(1-\nu^2)} \\
\tilde{L}_{2,1} &= \left(\frac{k_y n(1+\nu)}{2R} \right) \frac{Eh}{(1-\nu^2)} \\
\tilde{L}_{2,2} &= \left(\frac{k_y^2(1-\nu)}{2} + \frac{h^2 k_y^2(1-\nu)}{8R^2} + \frac{n^2}{R^4} \right) \frac{Eh}{(1-\nu^2)} \\
\tilde{L}_{2,3} &= \left(-\frac{in}{R^2} - \frac{ik_y^2(3-\nu)h^2 n}{24R^2} \right) \frac{Eh}{(1-\nu^2)} \\
\tilde{L}_{3,3} &= \left(\frac{1}{R^2} + \frac{h^2}{12} \left[k_y^4 + \frac{2n^2 k_y^2}{R^2} + \frac{n^4}{R^4} + \frac{1}{R^4} - \frac{2n^2}{R^4} \right] \right) \frac{Eh}{(1-\nu^2)} \\
\tilde{L}_{3,1} &= -\tilde{L}_{1,3} \\
\tilde{L}_{3,2} &= -\tilde{L}_{2,3}
\end{aligned} \tag{6.14}$$

Structural damping is included by making the Young's modulus E complex such that E is replaced by $E(1+i\eta_s)$ in equation (6.13). In the numerical examples, $\eta_s = 0.01$ is used, unless otherwise stated. For light fluid loading, the fluid loading effect might be neglected by setting the terms $D_{f,i}$ and $D_{f,o}$ in equation (6.13) equal to zero.

6.2.2.2 WFE Model

In this section, a wave and finite element method is used to model the structure. The cylinder is assumed to be homogeneous in the axial and circumferential directions, but has arbitrary through-thickness properties, so that laminates etc. can be modelled straightforwardly.

Only a small curved segment of the cylindrical shell is used. The segment is discretised using finite element. The modelling approach for the curved structure is similar to reference [130]. There are various elements available in FE software. Typically shell elements are used to model thin, isotropic cylindrical shells. For more complicated structures (e.g. laminates),

ANSYS SOLID185 elements are preferred for modelling the deformation through the thickness of the laminated structure.

The segment subtends an angle $\Delta\phi$ at the axis of the cylinder, as shown in figure 6.2. The angle should be small enough such that the curved segment can be approximated using a flat rectangular segment since curved elements are not commonly available in commercial FE software. The nodal coordinates of the FE model at the right hand side of the segment should be rotated by an angle $\Delta\phi$ for modelling the curvature of the cylinder. Considering the FE model of the segment with dimensions $L_x \times L_y$ shown in figure 6.2. There are no internal, or edge, boundary DOFs in this FE model. Interior and edge nodes can be included straightforwardly [113] and eliminated by dynamic condensation. The vector of DOFs \mathbf{q} is partitioned as

$$\mathbf{q} = [\mathbf{q}_1^T \quad \mathbf{q}_2^T \quad \mathbf{q}_3^T \quad \mathbf{q}_4^T]^T \quad (6.15)$$

where the superscript “ T ” denotes transposition and the subscripts “1”, “2”, “3”, “4” correspond to the corner hyper-nodes of the segment. The vectors of internal nodal forces \mathbf{f} and external nodal forces \mathbf{e} are partitioned in the same manner.

The mass and stiffness matrices \mathbf{M}_{loc} and \mathbf{K}_{loc} of the curved segment are found in the local coordinate system of the element. Curvature of the cylinder is allowed for by rotating the nodal coordinates of those of the flat segment around the y-axis by an angle of $\Delta\phi$. The mass and stiffness matrices are then

$$\mathbf{M} = \mathbf{R}^T \mathbf{M}_{loc} \mathbf{R} \quad \mathbf{K} = \mathbf{R}^T \mathbf{K}_{loc} \mathbf{R} \quad (6.16)$$

where the transformation matrix \mathbf{R} can be found from equation (5.45) and equation (5.46). The equation of motion of the segment can be written as

$$[\mathbf{K} - \omega^2 \mathbf{M}] \mathbf{q} = \mathbf{f} + \mathbf{e} \quad (6.17)$$

where structural damping can be included straightforwardly by making the stiffness matrix complex, $\mathbf{K}(1 + i\eta_s)$. If each layer of the laminated segment has different damping loss factors, they can be considered separately and assembled together using the method described in reference [140].

6.2.3 Fluid-Structural Interaction

During the FE discretisation, the external pressures on the surfaces of the segment are modelled as equivalent nodal forces using the approach developed in chapter 2. For example, for the j -th hyper-node, the vector of external nodal forces can be written as

$$\mathbf{e}_j = \tilde{p}_i \mathbf{u}_1 \alpha_j - \tilde{p}_o \mathbf{u}_2 \alpha_j \quad (6.18)$$

where \tilde{p}_i and \tilde{p}_o represent the complex amplitudes of the total external pressures applied on the inner and outer surfaces of the structure respectively. All the elements in vectors $\mathbf{u}_{1,2}$ are zero except for those corresponding to the normal displacements of the inner (w_1) and outer (w_2) surfaces of the segment, i.e.

$$w_1 = \mathbf{u}_1^T \mathbf{q}_j \quad w_2 = \mathbf{u}_2^T \mathbf{q}_j. \quad (6.19)$$

The coefficients α_j can be obtained by calculating the consistent nodal forces

$$\alpha_j = \iint_{S_j} e^{-in\phi - ik_z z} N_j(x, y, z) dx dy \quad (6.20)$$

where the integration area is denoted by S_j for the j -th hyper-node and $N_j(x, y, z)$ is the corresponding shape function associated with the normal displacements of the surface. Alternatively they may be approximated by lumped forces.

6.2.4 Spectral Dynamic Stiffness Matrix and Responses

The spectral dynamic stiffness matrix is derived in this section for a small segment of the structure. The DOFs of the hyper-nodes of the FE model can be related using the periodicity theories and equilibrium conditions, e.g.,

$$\mathbf{q}_2 = \lambda_x \mathbf{q}_1, \quad \mathbf{q}_3 = \lambda_y \mathbf{q}_1, \quad \mathbf{q}_4 = \lambda_x \lambda_y \mathbf{q}_1, \quad (6.21)$$

where $\lambda_x = e^{-ik_x L_x}$ with $k_x = n/R$, and $\lambda_y = e^{-ik_y L_y}$ are wave propagation constants for each harmonic wave component. Thus, the total DOF vector \mathbf{q} can be expressed as

$$\mathbf{q} = \Lambda_R \mathbf{q}_1, \quad \Lambda_R = \begin{Bmatrix} \mathbf{I} \\ \lambda_x \mathbf{I} \\ \lambda_y \mathbf{I} \\ \lambda_x \lambda_y \mathbf{I} \end{Bmatrix}. \quad (6.22)$$

Similarly for the nodal forces equilibrium implies that

$$\Lambda_L \mathbf{f} = \mathbf{0}, \quad \Lambda_L = \{ \mathbf{I} \quad \lambda_x^{-1} \mathbf{I} \quad \lambda_y^{-1} \mathbf{I} \quad \lambda_x^{-1} \lambda_y^{-1} \mathbf{I} \}. \quad (6.23)$$

Substituting equation (6.22) into equation (6.17), and pre-multiplying each side by Λ_L gives

$$\mathbf{D}_s \mathbf{q}_1 = \Lambda_L \mathbf{e}, \quad \mathbf{D}_s = \Lambda_L [\mathbf{K} - \omega^2 \mathbf{M}] \Lambda_R \quad (6.24)$$

where \mathbf{D}_s is the spectral dynamic stiffness matrix without considering the fluid loading effect.

Substituting equation (6.20) into equation (6.18), and the results into equation (6.24) gives

$$\mathbf{D} \mathbf{q}_1 = \tilde{P}_{b,o} \varepsilon \mathbf{u}_1 \quad (6.25)$$

where the total spectral dynamic stiffness matrix \mathbf{D} and the coefficient ε can be expressed as

$$\begin{aligned} \mathbf{D} &= \mathbf{D}_s + \varepsilon D_{f,i}^n \mathbf{u}_1 \mathbf{u}_1^T + \varepsilon D_{f,o}^n \mathbf{u}_2 \mathbf{u}_2^T, \\ \varepsilon &= \alpha_1 + \lambda_x^{-1} \alpha_2 + \lambda_y^{-1} \alpha_3 + \lambda_x^{-1} \lambda_y^{-1} \alpha_4, \end{aligned} \quad (6.26)$$

Once the displacement vector \mathbf{q}_i is calculated from equation (6.25), the acoustic pressures can be found from equation (6.6) and equation (6.9).

6.2.5 Acoustic Potential Energy

In this section, an expression is developed to quantify the pressure level within a cylindrical shell excited by an exterior sound source. The time-averaged acoustic potential energy can be written as

$$E_p = \frac{1}{4c_i^2 \rho_i} \int_{-\infty}^{\infty} \int_0^{r_i} \int_0^{2\pi} |p|^2 r d\phi dr dy \quad (6.27)$$

where the acoustic pressure is given by equation (6.3) and equation (6.5). Substituting and evaluating the integral give

$$E_p = \sum_{n=-\infty}^{\infty} \int_{-\infty}^{\infty} \tilde{E}_p dk_y, \quad (6.28)$$

where

$$\tilde{E}_p = \frac{(2\pi\rho_i\omega^2)^2}{4c_i^2 \rho_i} |I_r| \frac{|\tilde{w}_{r,i}|^2}{|k_{r,i} J'_n(k_{r,i} r_i)|^2}. \quad (6.29)$$

In equation (6.29), I_r can be written as [76]

$$I_r = \int_0^{r_i} J_n^2(k_{r,i} r) r dr = \frac{1}{2} r_i^2 \left[J_n^2(k_{r,i} r_i) - J_{n-1}(k_{r,i} r_i) J_{n+1}(k_{r,i} r_i) \right]. \quad (6.30)$$

6.3 Illustrative Examples

In this section, various numerical examples are presented to illustrate the application of the WFE method. The examples include a thin, isotropic cylinder excited by an exterior acoustic monopole source, an infinite cylindrical pipe made from isotropic material subjected to a radial, time-harmonic point force, and sound transmission through an orthotropic cylinder. The WFE results are compared with those of an analytical model taken from the literature.

6.3.1 Spherical Wave Interacting with a Cylindrical Shell

The excitation of a thin, cylindrical, steel shell by an exterior time-harmonic monopole source is first considered. The point source has the strength $Q_0 = 1\text{m}^3/\text{s}$ and is located at $y = 0, r = 1.2\text{m}$, and $\phi = 0^\circ$. The cylinder is constructed from a homogeneous, isotropic material with density $7800\text{kg}/\text{m}^3$, Young's modulus $2 \times 10^{11}\text{Pa}$ and Poisson's ratio 0.3. The cylinder has a thickness of 1.8 mm and a mean radius of 1 m. The fluid inside the cavity of the cylinder has density $1.225\text{kg}/\text{m}^3$ and speed of sound $340\text{m}/\text{s}$ while the fluid exterior to the cylinder has density $0.4135\text{kg}/\text{m}^3$ and speed of sound $299.5\text{m}/\text{s}$.

A small curved segment of the structure is discretised using one ANSYS SHELL181 element to obtain the mass and stiffness matrices. This element is rectangular with 4 nodes and six degrees of freedom at each node: translations in the nodal x, y and z directions and rotations about the x, y and z axes. For the results presented here, the acoustic pressures were lumped at the element nodes during the FE discretisation and applied at the mean radius.

The amplitude of the radial displacement $|\tilde{w}_{r,i}|$ is predicted using both the WFE model and the analytical model of section 6.2.2. The results are presented in figure 6.3 for four different frequencies and three different azimuthal mode numbers. There is no discernable difference between the results obtained using the WFE and analytical methods, so only one curve is plotted for each case.

The peaks in $|\tilde{w}_{r,i}|$ observed in figure 6.3 are caused by several different mechanisms including structural resonances, a peak in the applied radial stress (due to the behaviour of the blocked pressure) and internal fluid resonances. The structural resonances occur because of coincidence between the excitation wavenumbers and those of propagating waves in the cylinder. As an example, we consider the case for which $n=1$ and $\omega=10000\text{rad}/\text{s}$ shown in figure 6.4 (left). The dispersion curves for the *in vacuo* structure are shown in figure 6.4 (right).

The peak at $k_y \approx 33.4 \text{ m}^{-1}$ is caused by a peak in the exterior fluid loading after which the amplitude of the loading and radial displacement decay rapidly with increasing k_y . The three other peaks are observed to coincide with the wavenumbers of the flexural, shear and extensional waves identified in the dispersion analysis. A series of small ‘glitches’ associated with internal fluid resonances are also present, however, these are not readily discernible in the plot as the damping used in this example is sufficiently large to limit their amplitude.

Figure 6.5 shows the time average acoustic potential energy E_p versus ω for the steel cylinder. There is no discernible difference between the results obtained using the WFE method and analytical methods so only one curve is shown. The peak occurs at approximately 5000rad/s, which is close to the ring frequency $\omega_r = \sqrt{E/[\rho R^2(1-\nu^2)]} = 5308\text{rad/s}$ of the cylinder. The other peaks are associated primarily with resonances of the internal fluid (e.g. cut-on of the various internal wave modes), with higher order structural wave modes having a less pronounced effect.

6.3.2 Sound Radiation from a Pipe Excited by a Point Force

Now consider the case of a cylindrical structure excited by an internal point force. The cylinder is a steel pipe (Young’s modulus $2 \times 10^{11} \text{ Pa}$, density 7800 kg/m^3 , Poisson’s ratio 0.3) with thickness 2mm and mean radius 36mm. The fluid inside the cylinder is water with density and speed of sound, $\rho_i = 1000 \text{ kg/m}^3$, $c_i = 1500 \text{ m/s}$ while the fluid exterior to the cylinder is air with density and speed of sound $\rho_o = 1.225 \text{ kg/m}^3$ and $c_o = 340 \text{ m/s}$. A point force of magnitude $F=1 \text{ N}$ acts at $y=0$ and $\phi=0^\circ$ thus the radial component of the applied stress is $F\delta(y)\delta(\phi)/r_i$, and therefore the Fourier transform is $F/(2\pi)^2$.

The sound power radiated from the outer surface is given by

$$\Pi = \frac{1}{2} \text{Re} \left\{ i\omega \int_{-\infty}^{\infty} \int_0^{2\pi} p_o w_{r,o}^* r_o d\phi dy \right\} \quad (6.31)$$

Substituting for p_o and evaluating the integrals yields

$$\Pi = \sum_{n=-\infty}^{\infty} \int_{-k_o}^{k_o} \tilde{\Pi} dk_y, \quad (6.32)$$

where

$$\tilde{\Pi} = 4\pi\rho_o\omega^3 \left| \frac{\tilde{w}_{r,o}(k_y, n)}{k_{r,o} H_n^{(1)}(k_{r,o} r_o)} \right|^2. \quad (6.33)$$

Note that axial wavenumbers for which $|k_y| \geq k_o$, that is, waves which have subsonic axial propagation speeds, do not contribute to the sound power (i.e. they do not radiate to the far-field). All azimuthal modes radiate when $|k_y| \leq k_o$, when the axial propagation speed is supersonic, although modes for which $|n|$ is much larger than $k_{r,o} r_o$ do not radiate efficiently (and this efficiency decreases rapidly with increasing $|n|$). This “radiation efficiency effect” is governed by the behaviour of the Hankel function term in the denominator of the integrand in equation (6.33).

In order to validate the WFE method, a 1D WFE method similar to that presented in [116] is used to determine the dispersion curves for the fluid-filled cylindrical structure (with a vacuum exterior to the cylinder). A small segment of the structure 2mm long was meshed using 64 ANSYS SOLID185 elements and 200 ANSYS FLUID30 elements, which gives 564 nodes (64×3×2 structural DOFs and 209×2 fluid DOFs). The mesh used in the FE model is shown in figure 6.6.

Figure 6.7 shows the real part of the dispersion curves for propagating waves with azimuthal mode numbers $n=0$ and $n=1$. The vertical lines in figure 6.7 denote the locations of the excitation frequencies for the plots shown in figure 6.8 which shows curves of $|\tilde{w}_{r,i}|$ versus k_y for the azimuthal modes $n=0$ and $n=1$ for $\omega=18850\text{rad/s}$ (left plot) and $\omega=50265\text{rad/s}$ (right plot). As expected, the peaks in the curves in figure 6.8 occur at values of k_y close to the wavenumbers of those of the dispersion curves shown in figure 6.7. The azimuthal mode number of the waves identified in the dispersion analysis can be determined by inspection of the nodal displacement in the FE model. For example, the displacement

of the mesh for the $n=0$ and $n=1$ azimuthal modes at $\omega=18850\text{rad/s}$ are shown in figure 6.9. Figure 6.10 shows the time-averaged power radiated from the cylindrical as a function of ω .

6.3.3 Sound Transmission through an Orthotropic Cylinder

In this section, the transmission loss for an orthotropic cylindrical shell with a mean radius of $R=2\text{m}$ and thickness $h=1\text{mm}$ is determined using the WFE method. These predictions are compared with results generated using an analytical model. The analytical model is mainly based on the first-order plate theory developed by Hencky-Mindlin. A plane stress assumption is made for each layer of the laminated shell. The inter-laminar normal stress is neglected for the analytical model. More details are described in Berthelot [60] (see also [70]). The material properties of the structure are taken from table 1 in reference [136]. They are Young's moduli $E_\phi=1.336\times 10^{11}\text{Pa}$, and $E_y=E_r=7.7\times 10^9\text{Pa}$, and shear moduli $G_{yr}=2.6\times 10^9\text{Pa}$, $G_{\phi r}=3.1\times 10^9\text{Pa}$, and $G_{\phi y}=3.1\times 10^9\text{Pa}$, Poisson's ratios $\nu_{\phi y}=\nu_{\phi r}=0.29$, and $\nu_{yr}=0.49$, density $\rho=1550\text{kg/m}^3$, and damping loss factor $\eta=0.01$.

A small curved segment of the structure was discretised using a four-noded, rectangular shell element with dimensions $L_x=L_y=2\text{mm}$. A single integration point is used through the thickness of the element. The WFE model is used to calculate the oblique transmission loss for plane waves with incident angles $\theta=90^\circ, 45^\circ$ and 25° where θ is the angle at which the incident wave propagates relative to the y -axis (with $\theta=0^\circ$ corresponding to a wave propagating along the positive y -axis). The predicted results are shown in figure 6.11 along with those of the analytical model. The agreement between the two models is observed to be excellent, except for small discrepancies at high frequencies which are due to the different assumptions used in the analytic and WFE models, e.g. the analytical model uses first-order shear deformation theory and estimates the shear correction factors using Whitney's model [72] whilst the WFE model is based on improved transverse shear stresses [73, 74] with no need to calculate the shear correction factors.

6.4 Application Examples

The WFE method has been validated in section 6.3 by comparing the predictions with those of analytical methods and it has been demonstrated that the WFE method can produce accurate predictions in a straightforward manner at small computation cost. In this section, the WFE method is applied to complicated structures (e.g. cross-ply sandwich cylinders, laminated cylinders) for which formulating analytical models is difficult.

6.4.1 Laminated Sandwich Cylinder

In order to demonstrate the usefulness of the WFE method, it is now applied to a more complicated structure of total thickness 18 mm and mean radius 1 m. The structure consists of an antisymmetric, cross-ply, sandwich cylinder made up of a lightweight foam core sandwiched between two laminated skins. The outer skin consists of four orthotropic sheets of graphite epoxy with a stacking sequence of $[45^\circ / -45^\circ / -45^\circ / 45^\circ]$ whilst the orthotropic sheets of the inner skin are of the same material but with a layup of $[-45^\circ / 45^\circ / 45^\circ / -45^\circ]$. The total thickness of each composite skin is 4 mm. Each lamina is made of the same materials and has Young's moduli $E_\phi = 1.44 \times 10^{11}$ Pa, and $E_y = E_r = 9.63 \times 10^9$ Pa, and shear moduli $G_{yr} = G_{\phi r} = G_{\phi y} = 4.182 \times 10^9$ Pa, Poisson's ratios $\nu_{\phi y} = \nu_{\phi r} = 0.02$, and $\nu_{yr} = 0.3$, density $\rho = 1386 \text{ kg/m}^3$, and damping loss factor $\eta = 0.04$. The 10-mm thick ROHACELL foam core has Young's modulus of 0.18 GPa, Poisson's ratio 0.286, and density of 110 kg/m^3 . A 1mm square, rectangular segment of the structure was meshed using ANSYS SOLID185 elements in which four elements were used for each skin (one element per lamina) and the foam core was meshed using 10 elements through the thickness.

The dispersion curves for the *in vacuo* structure at low frequencies are shown in figure 6.12 for the $n=0$ and $n=1$ modes. It is observed that the structure supports multiple wave

modes. The dispersion curves are complicated, involving real, pure imaginary and complex-valued wavenumbers, cut-off, cut-on and bifurcations of wave branches. At low frequencies, for $n=0$ there are propagating axial and torsional waves and a ring frequency (where a bending-like mode cuts on) at around 3000 rad/s. For $n=1$ there are propagating and evanescent bending modes, with complicated cut-on and other dispersion effects around 3000 rad/s.

Figure 6.13 (left) plots the amplitude of the radial displacement versus wavenumber component k_y for the $n=0$ breathing mode at frequency $\omega=10000$ rad/s. As was observed in the corresponding plot for the isotropic, homogeneous cylindrical shell, multiple peaks are present. The peaks close to $k_y = 18 \text{ m}^{-1}$ and 27 m^{-1} correspond closely to free waves in the system with the wavenumbers shown in the dispersion curves plotted in figure 6.12 (right). As before, the peak close to $k_y = 33.4 \text{ m}^{-1}$ is caused by a peak in the exterior fluid loading after which the amplitude of the loading and the radial displacement decay rapidly with increasing k_y . Figure 6.14 shows the time average potential power in the cylinder as a function of frequency for the laminated sandwich cylinder. The peaks are associated with resonances (i.e. cut-on of the various wave modes) primarily of the internal fluid.

6.4.2 Orthotropic Cylinder

In this section an infinite orthotropic cylinder made of graphite epoxy is considered. The elastic properties are the same as those of the composite skins given in the example presented in subsection 6.4.1. The mean radius and the radial thickness of the cylindrical shell is 0.036m and 4mm respectively. A small curved segment of the structure is used to develop a WFE model. The segment is meshed through the thickness using 4 ANSYS SOLID185 elements of dimensions $L_x = L_y = 1\text{mm}$. Figure 6.15 shows the predicted time-averaged radiated power. The first peak is associated with the ring frequency.

6.5 Conclusions

An efficient WFE method for analysing the response of an infinitely long cylindrical structure filled and surrounded by fluids has been developed. The formulation is general and can be used to analyse sound radiation or transmission due to arbitrary internal or external excitation. The interior and exterior acoustic loading is modelled analytically. The structure is modelled using only a small curved segment. The segment is discretised using FE to obtain the mass and stiffness matrices. During the FE discretisation, the acoustic pressures on the surfaces of the cylinder are expressed as equivalent nodal forces to be applied to the FE model. Using the periodicity and equilibrium conditions, the mass and stiffness matrices are post-processed together with the equivalent nodal forces to obtain the total spectral dynamic stiffness matrix of the system. By solving the structural responses, the displacements can be found. Once the radial displacements are found, the acoustic pressures can be calculated using the fluid dynamic stiffnesses.

The method was validated by comparison with analytic solutions for three example problems: (1) the internal sound field produced by an acoustic source exterior to a thin-walled cylinder, (2) the radiation from a thin-walled cylinder due to excitation from a point force acting on the inner surface and (3) sound transmission through an orthotropic cylinder. The agreement between the WFE predictions and the analytical results is excellent. In order to demonstrate the usefulness of the method, the WFE method was then used to predict sound transmission through, and radiation from, more complicated cylindrical structures for which establishing the analytical equation of motion is difficult. The WFE method can be seen to be an efficient and straightforward method at a small computational cost.

Figures

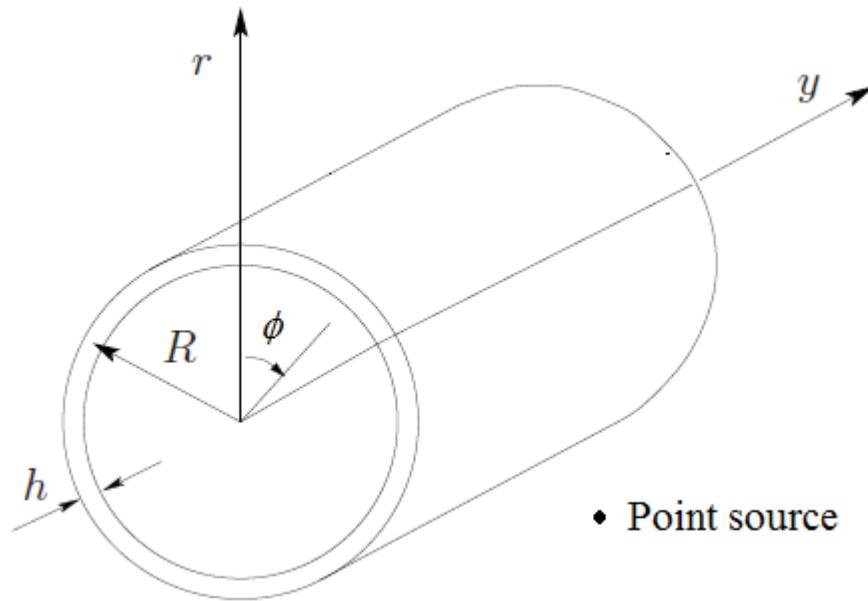


Figure 6.1: Infinite cylinder of thickness h , coordinate system and an exterior acoustic point source.

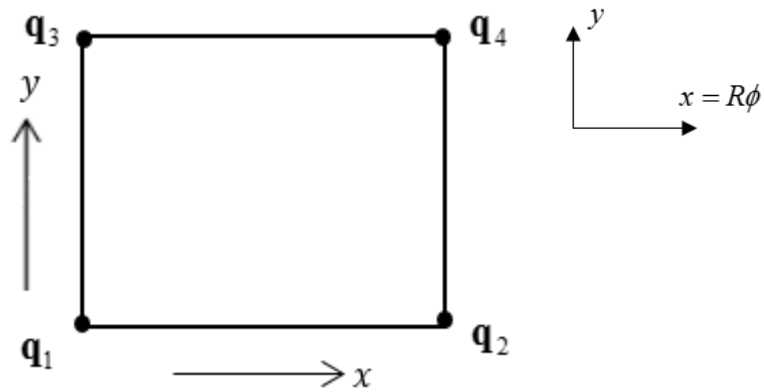


Figure 6.2: A rectangular element, of dimension $L_x \times L_y$ used to model a segment of the cylinder. The four corner nodes are labelled and the alignment of the segment coordinate system is shown.

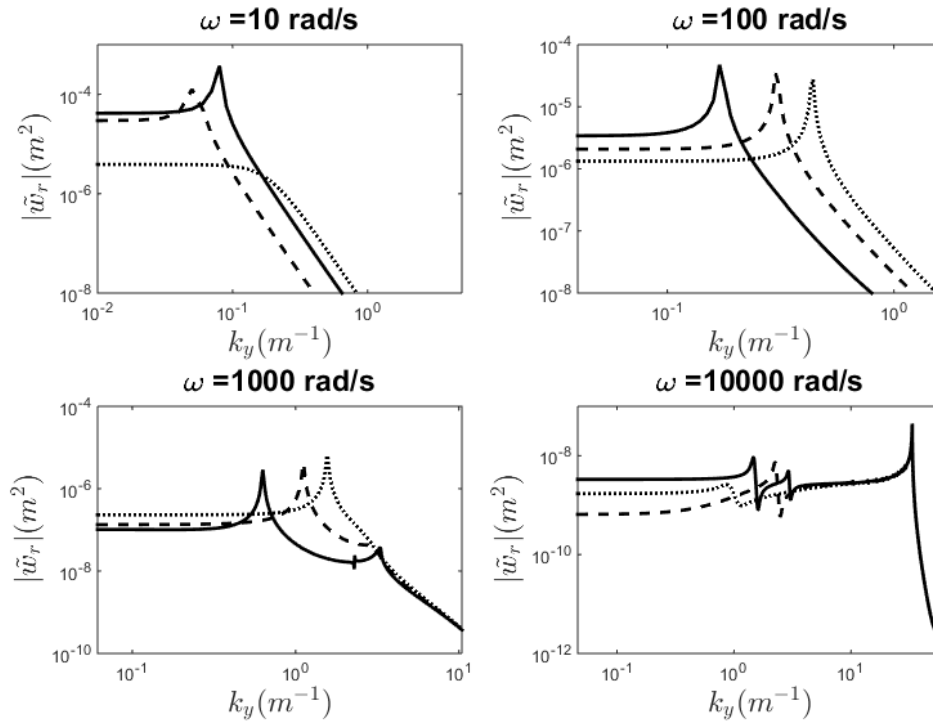


Figure 6.3: Isotropic, thin steel cylinder excited by an exterior monopole source: magnitude of Fourier transform radial displacement $|\tilde{w}_{r,i}|$ vs k_y at cylindrical coordinates $(r, \phi, y) = (1, 0, 0)$ for $n=1$ (solid line), 2 (dash-dotted) and 3 (dotted line) for $\omega = 10 \text{ rad/s}$ (top left); $\omega = 100 \text{ rad/s}$ (top right); $\omega = 1000 \text{ rad/s}$ (bottom left); and $\omega = 10000 \text{ rad/s}$ (bottom right).

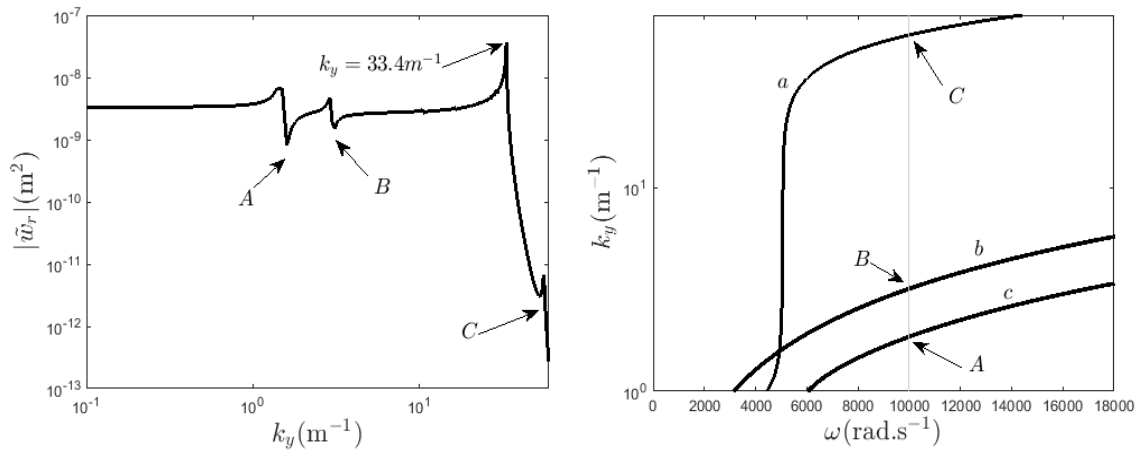


Figure 6.4: Isotropic, thin steel cylinder excited by an exterior monopole source: magnitude of radial displacement $|\tilde{w}_{r,i}|$ vs k_y for $n=1$, $\omega=10000\text{rad/s}$ (left). The three peaks associated with different wave branches are labelled A , B and C whilst the peak at $k_y = 33.4/\text{m}$ is associated with a peak in the exterior fluid loading. Dispersion curves (right): flexural wave (branch a), shear wave (branch b) and extensional wave (branch c). The points at which the dispersion curves cross $\omega = 10000\text{rad/s}$ closely correspond to labelled peaks in the left-hand plot.

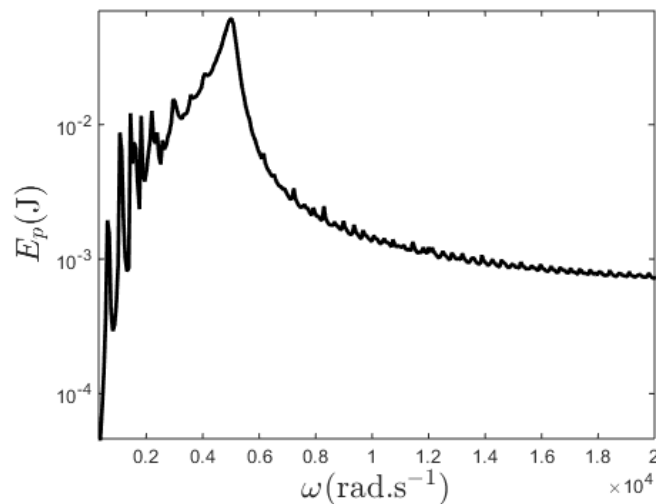


Figure 6.5: Thin, isotropic steel cylinder: time averaged interior potential energy E_p as a function of frequency ω .

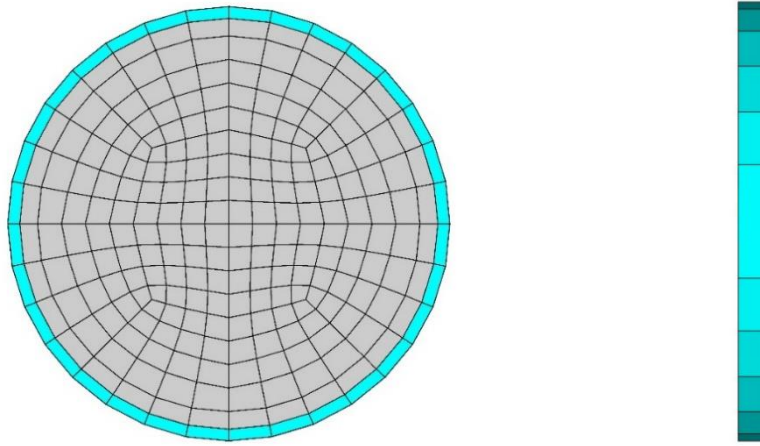


Figure 6.6: FE model mesh for a WFE model of the water-filled steel cylinder viewed looking along the axis (left) and side-on (right). The cylinder elements are shown as blue whereas the interior fluid elements are shown as grey.

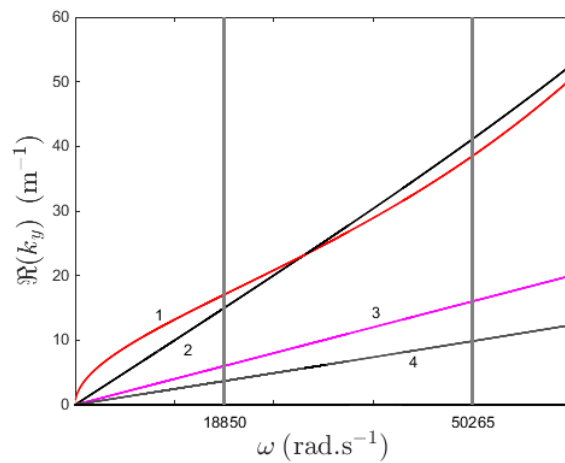


Figure 6.7: Dispersion curves for the water-filled steel cylinder for the $n = 0$ and $n = 1$ modes; branch 1: beam-type wave mode; branch 2: fluid-acoustic mode, branch 3, 4: extensional/torsional wave mode.

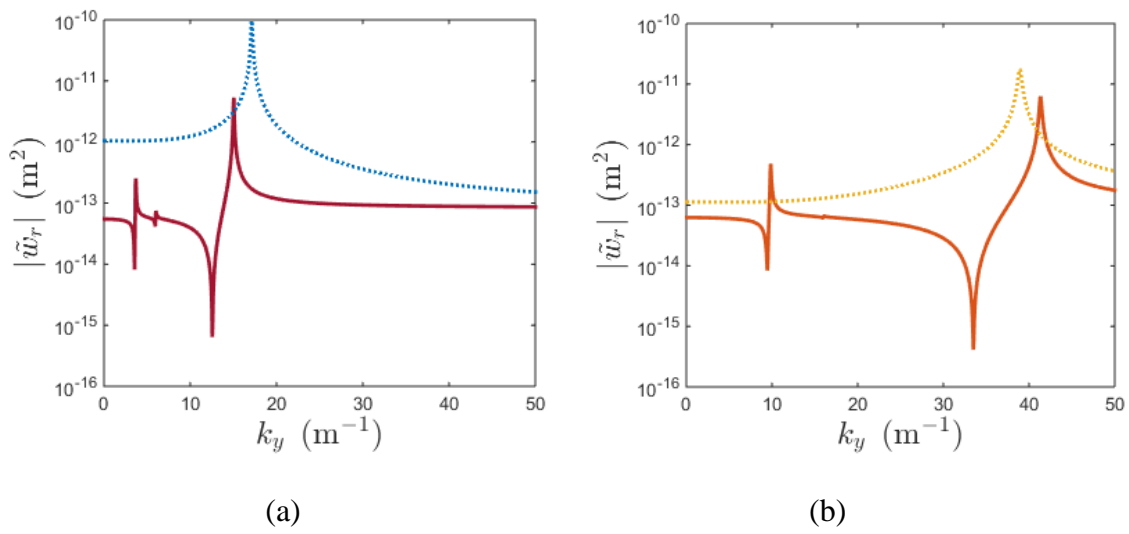


Figure 6.8: Magnitude of radial displacement $|\tilde{w}_{r,i}|$ (at $y = \phi = 0$) as a function of k_y for the water-filled steel cylinder for $n=0$ and $n=1$ for $\omega = 18850 \text{ rad/s}$ (a), $\omega = 50265 \text{ rad/s}$ (b),

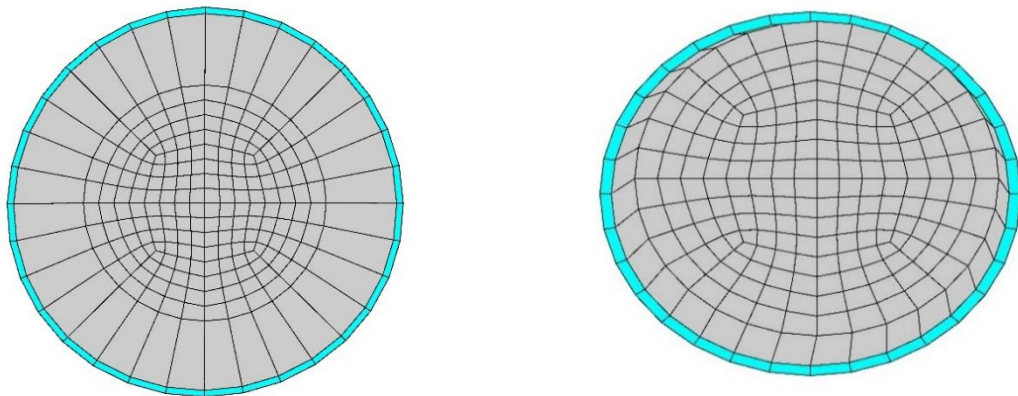


Figure 6.9: Water-filled steel cylinder: nodal displacements for two modes at $\omega = 18850 \text{ rad/s}$, $k_y = 15.05 \text{ rad/s}$, $n=0$ (left); $k_y = 17.1/\text{m}$, $n=1$ (right).

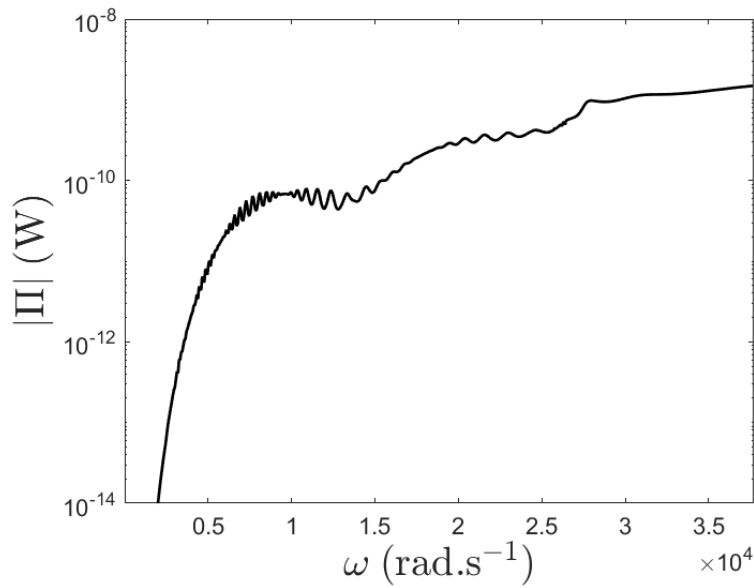


Figure 6.10: Time average power radiated from the water-filled steel cylinder Π as a function of ω .

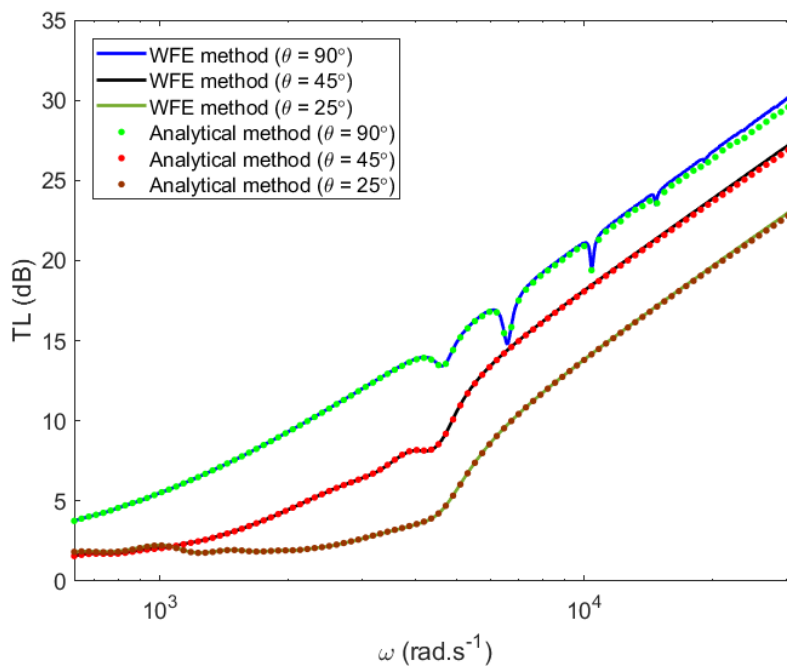


Figure 6.11: Oblique transmission loss (TL) of an orthotropic cylinder: solid lines denote WFE predictions, dots denote results calculated using the analytical model in references [17]; various θ .

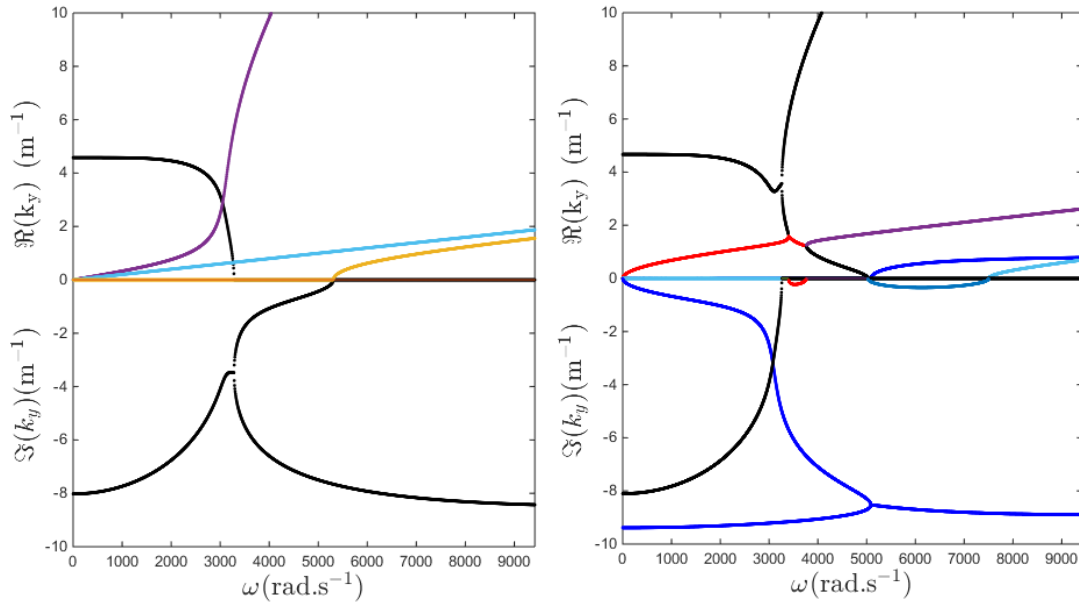


Figure 6.12: Dispersion curves for the *in vacuo* laminated sandwich cylinder at azimuthal mode order $n = 0$ (left); and $n = 1$ (right).

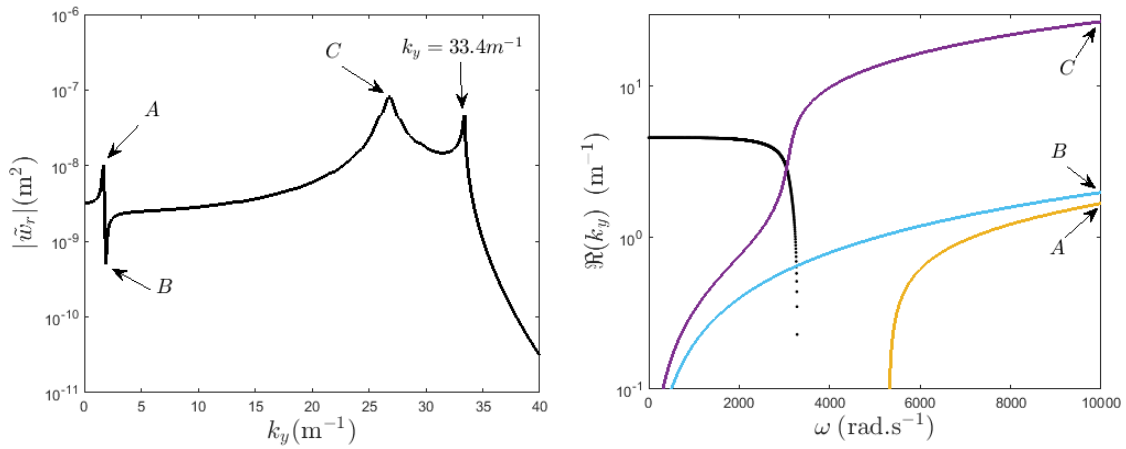


Figure 6.13: Laminated sandwich cylinder $|\tilde{w}_{r,i}|$ vs k_y at $(r, \phi, y) = (1.009, 0, 0)$ for $n = 1$, $\omega = 10000 \text{ rad/s}$ (left). The three peaks associated with different wave branches are labelled A , B and C whilst the peak at $k_y = 33.4/\text{m}$ is associated with a peak in the exterior fluid loading. The real part of the dispersion curves for the *in vacuo* structure (right). The points at which the dispersion curves cross $\omega = 10000 \text{ rad/s}$ closely correspond to the labelled peaks in the left-hand plot.

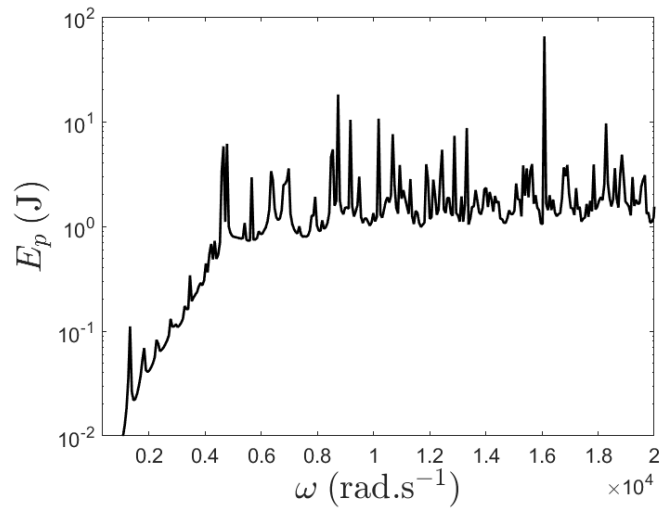


Figure 6.14: Time average potential energy inside the laminated sandwich cylinder.

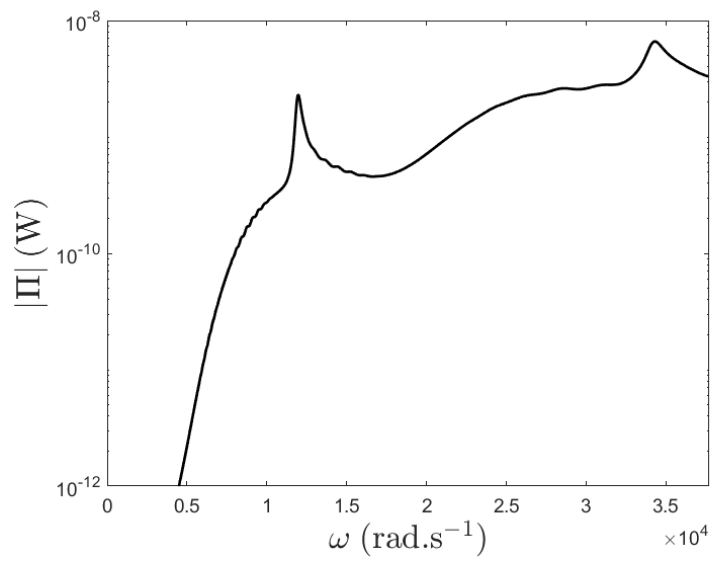


Figure 6.15: Time average radiated power Π as a function of ω for the water-filled orthotropic cylinder.

Chapter 7

Concluding Remarks

This chapter summarises the present work and presents conclusions. Possible further work is suggested.

7.1 Summary of Present Work

In this thesis, the WFE method was extended to model the vibroacoustic performance of panels whose properties are arbitrary through the thickness but otherwise uniform. Sound transmission and sound radiation were analysed.

In chapter 2, the WFE method was extended for estimating sound transmission through, and radiation from infinite flat panels. Using this method, only a small segment of the structure is modelled. A conventional FE method was used to discretise the segment. The fluid spaces were modelled analytically in terms of their spectral dynamic stiffnesses. In the FE discretisation, the sound pressures on the surfaces of the segment were resolved into equivalent external nodal forces. Periodicity theories and equilibrium conditions are used to postprocess the mass and stiffness matrices of the segment together with the nodal forces. A total spectral dynamic stiffness matrix of the system was found and used to calculate the structural response to acoustic or structural excitations. Once the structural displacements were found, sound pressures can be calculated analytically. For general applied forces, a spatial Fourier transform can be used to decompose the loading into an integral of space harmonics. For each harmonic component, the WFE formulation can be applied independently to find the structural response. The WFE model was first validated by considering sound transmission through an Euler

Bernoulli beam and a thin, isotropic plate. The WFE predictions were compared with those of analytical models in section 2.3. The agreement was seen to be excellent. Then, the WFE formulations were applied to laminated panels with various configurations (asymmetric panels and symmetric panels) for which finding analytical solutions is difficult.

Sound transmission through, and radiation from these structures were calculated. The dispersion curves were also plotted. At low frequencies, composite panels behave like a simple plate with typical extensional, shear and bending waves. They may be represented by a homogenised solid plate with equivalent material properties. At high frequencies, the dispersion curves become complicated. For example, higher-order wave branches may cut on. Some original wave branches may veer, resulting in wave modes which can radiate sound effectively. Such complicated wave characteristics can be captured readily using the WFE model.

The WFE model developed in chapter 2 was then extended to finite-sized, rectangular panels in Chapter 3. A multi-layer structure with fluid layers coupled to infinite fluid spaces was considered. In order to reduce computational cost, fluid layers were modelled analytically using a wave approach while solid layers were modelled using the WFE method. Formulations for assembling the spectral dynamic stiffness matrices of various layers were derived to find the structural responses to acoustic excitation. For taking the finite size into account, a spatial windowing technique was applied to the infinite system. The application of the windowing technique introduces a geometrical correction factor for the sound transmission loss of infinite panels. The radiated power was distributed in the wavenumber space instead of concentrated in the particular wavenumber component of the incident wave.

Note that the resonance frequencies due to the finite extent of the structure were neglected by this method. Various numerical examples were presented to illustrate the usefulness of this

method. The WFE predictions were compared with experimental measurements and the agreement was observed to be good.

For non-homogenous, periodic panels, a periodic cell of a structure must be used for the WFE model. In chapter 4 the WFE method was used to predict the vibroacoustic behaviour of such structures with particular emphasis on honeycomb-cored panels. Note that the structural and acoustic wavelengths were assumed to be much larger than the dimensions of the periodic cell such that the infinite acoustic space can be modelled exactly in the same manner as that in chapter 2 and a homogenised model of the system found. Due to the complexity of the core geometry, the discretisation of the periodic cell leads to a large number of DOFs. For reducing computational cost, Guyan reduction was used to reduce the internal DOFs at low frequencies. The boundary DOFs were condensed using periodicity theory. A spectral dynamic stiffness matrix was found for the reduced WFE model for calculating the structural and acoustic responses. The reduced WFE model was a homogenised model which can capture the complexity of the core geometry. The WFE model was used to predict the dispersion curves and sound transmission loss. The predictions were compared with those of approximate models and experimental measurements. The good agreement shows the efficiency and accuracy of the WFE model in predicting sound transmission through composite panels with complex cores.

The WFE method was extended in chapter 5 for predicting the vibroacoustic characteristics of 2-dimensional circular shells. A curved segment of a circular cross-section was modelled using flat elements. For modelling the curvature of the segment, the nodal coordinates of the FE model need to be rotated by the small angle that the segment subtends at the centre of the shell. The sound pressures generated by a line volume source were found using a Fourier transform method. Using the WFE procedures presented in chapter 1, a spectral dynamic stiffness matrix was found for calculating the sound transmission loss. The sound

pressure variations along the radial directions were found using the WFE model and compared with that of an analytical model. The agreement was observed to be excellent.

Finally, the WFE formulations developed in chapter 5 were extended to three-dimensional circular cylindrical shells in Chapter 6. A small curved area of the structure was modelled using a conventional FE method. The acoustic pressures were found analytically for a point source inside or exterior to the shell using a Fourier transform method. Structural excitation was also considered. The pressures on the shell can be represented as a sum of the blocked pressure and the pressure due to the vibration of the shell. The fluid loading effect was described by using a fluid dynamic stiffness. The WFE formulations were first validated by comparing the displacement responses of an isotropic shell predicted by the WFE model and an analytical model. Sound transmission through an orthotropic cylindrical shell was also considered. The agreement was excellent. The WFE model was then applied to predict sound transmission through laminated circular cylindrical shells, and sound radiation from fluid-filled pipes.

7.2 Conclusions

In this thesis, the extended WFE method has been proven to be an efficient and accurate method for predicting sound transmission through, and radiation from structures.

7.3 Suggestions for Further Work

In this section, some possibilities for further research are suggested.

1. For periodic structures, when the structural wavelengths are comparable to the dimensions of the periodic cell, space harmonics higher than the trace wavenumber become important. The structural responses may be written as the sum of harmonic waves with different wavelengths. The WFE formulations developed in this thesis may be extended to such panels.
2. For a large periodic cell or very fine elements, the FE model of a periodic cell may

contain a large number of boundary DOFs. For reducing the computational cost, a new technique for condensing the boundary DOFs is of interest.

3. Due to the finite extent of a practical structure, the structural resonances occurring at low frequencies can lead to large sound transmission, which are not predicted by applying the spatial windowing technique to infinite panels. A hybrid method may be of interest for describing the resonance frequencies.
4. The acoustic fields considered in this thesis were either plane or perfectly diffuse. In reality, the wavefield of the acoustic spaces are uncertain. For considering the uncertainty of the variation of acoustic spaces, a hybrid SEA-WFE method may be worthy of research.
5. This thesis has considered sound radiation from cylindrical shells. It would be very interesting to extend this method to calculate sound radiation from a tyre.

Publication List

Peer-reviewed Journal:

Y. Yang, B.R. Mace, M.J. Kingan, Prediction of sound transmission through, and radiation from, panels using a wave and finite element method, The Journal of the Acoustical Society of America, 141 (2017) 2452-2460.

Y. Yang, B.R. Mace, M.J. Kingan, Wave and finite element method for predicting sound transmission through finite multi-layered structures with fluid layers, Computers & Structures, 204 (2018) 20-30.

M.J. Kingan, Y. Yang, B.R. Mace, Sound transmission through cylindrical structures using a Wave and Finite Element method, Wave Motion,

Peer-reviewed conference papers:

Y. Yang, B.R. Mace, M.J. Kingan, Prediction of noise transmission through infinite panels using a wave and finite element method, Journal of Physics: Conference Series 744 (2016) 012235.

M.J. Kingan, Y. Yang, B.R. Mace, Application of the wave and finite element method to calculate sound transmission through cylindrical structures, Journal of Physics: Conference Series 744 (2016) 012240.

References

- [1] D.H. Bies, C.H. Hansen, R.H. Campbell, Engineering noise control, in, ASA, 1996.
- [2] J.-W. Kim, Sound transmission through lined, composite panel structures: transversely isotropic poro-elastic model, 2005.
- [3] J.N. Reddy, Theory and analysis of elastic plates and shells, CRC press, 2006.
- [4] S.P. Timoshenko, S. Woinowsky-Krieger, Theory of plates and shells, McGraw-hill, 1959.
- [5] R.D. Mindlin, Influence of rotatory inertia and shear on flexural motions of isotropic, elastic plates, J. appl. Mech., 18 (1951) 31-38.
- [6] A.W. Leissa, Vibration of shells, Scientific and Technical Information Office, National Aeronautics and Space Administration Washington, 1973.
- [7] F.J. Fahy, P. Gardonio, Sound and structural vibration: radiation, transmission and response, Elsevier, 2007.
- [8] J.-H. Lee, J. Kim, Study on sound transmission characteristics of a cylindrical shell using analytical and experimental models, Applied acoustics, 64 (2003) 611-632.
- [9] M.C. Junger, D. Feit, Sound, structures, and their interaction, MIT press Cambridge, MA, 1986.
- [10] L.E. Kinsler, A.R. Frey, A.B. Coppens, J.V. Sanders, Fundamentals of acoustics, Fundamentals of Acoustics, 4th Edition, by Lawrence E. Kinsler, Austin R. Frey, Alan B. Coppens, James V. Sanders, pp. 560. ISBN 0-471-84789-5. Wiley-VCH, December 1999., (1999) 560.
- [11] M.E. Goldstein, Aeroacoustics, New York, McGraw-Hill International Book Co., 1976. 305 p., (1976).
- [12] G. Kurtze, B. Watters, New wall design for high transmission loss or high damping, The Journal of the Acoustical Society of America, 31 (1959) 739-748.
- [13] R. Ford, P. Lord, A. Walker, Sound transmission through sandwich constructions, Journal of sound and vibration, 5 (1967) 9-21.
- [14] J. Moore, R. Lyon, Sound transmission loss characteristics of sandwich panel constructions, The Journal of the Acoustical Society of America, 89 (1991) 777-791.
- [15] J.A. Moore, Sound transmission loss characteristics of three layer composite wall constructions, in, Massachusetts Institute of Technology, 1975.
- [16] C.L. Dym, D. Lang, Transmission loss of damped asymmetric sandwich panels with orthotropic cores, Journal of Sound and Vibration, 88 (1983) 299-319.
- [17] S. Ghinet, N. Atalla, H. Osman, The transmission loss of curved laminates and sandwich composite panels, The Journal of the Acoustical Society of America, 118 (2005) 774-790.
- [18] S.E. Makris, C.L. Dym, J.M. Smith, Transmission loss optimization in acoustic sandwich panels, The Journal of the Acoustical Society of America, 79 (1986) 1833-1843.
- [19] C. Smolenski, E. Krokosky, Dilational - mode sound transmission in sandwich panels, The Journal of the Acoustical Society of America, 54 (1973) 1449-1457.
- [20] P. Thamburaj, J. Sun, Optimization of anisotropic sandwich beams for higher sound transmission loss, Journal of Sound and Vibration, 254 (2002) 23-36.
- [21] J. Bolton, N.-M. Shiau, Y. Kang, Sound transmission through multi-panel structures lined with elastic porous materials, Journal of sound and vibration, 191 (1996) 317-347.
- [22] L.J. Gibson, M.F. Ashby, Cellular solids: structure and properties, Cambridge university press, 1999.
- [23] B. Clarkson, M. Ranky, Modal density of honeycomb plates, Journal of Sound and Vibration, 91 (1983) 103-118.
- [24] K. Renji, P. Nair, S. Narayanan, Modal density of composite honeycomb sandwich panels, Journal of Sound and Vibration, 195 (1996) 687-699.

- [25] D. Zenkert, An introduction to sandwich construction, Engineering materials advisory services, 1995.
- [26] E. Nilsson, A. Nilsson, Prediction and measurement of some dynamic properties of sandwich structures with honeycomb and foam cores, *Journal of sound and vibration*, 251 (2002) 409-430.
- [27] Z. Zergoune, M. Ichchou, O. Bareille, B. Harras, R. Benamar, B. Troclet, Assessments of shear core effects on sound transmission loss through sandwich panels using a two-scale approach, *Computers & Structures*, 182 (2017) 227-237.
- [28] B. Tie, B. Tian, D. Aubry, Theoretical and numerical modeling of membrane and bending elastic wave propagation in honeycomb thin layers and sandwiches, *Journal of Sound and Vibration*, 382 (2016) 100-121.
- [29] R. Craig, M. Bampton, Coupling of substructures for dynamic analyses, *AIAA journal*, 6 (1968) 1313-1319.
- [30] J.-M. Mencik, D. Duhamel, A wave-based model reduction technique for the description of the dynamic behavior of periodic structures involving arbitrary-shaped substructures and large-sized finite element models, *Finite Elements in Analysis and Design*, 101 (2015) 1-14.
- [31] J.-M. Mencik, M. Ichchou, A substructuring technique for finite element wave propagation in multi-layered systems, *Computer Methods in Applied Mechanics and Engineering*, 197 (2008) 505-523.
- [32] R.J. Guyan, Reduction of stiffness and mass matrices, *AIAA journal*, 3 (1965) 380-380.
- [33] S.H. Chen, H. Pan, Guyan reduction, *International Journal for Numerical Methods in Biomedical Engineering*, 4 (1988) 549-556.
- [34] B. Downs, Accurate reduction of stiffness and mass matrices for vibration analysis and a rationale for selecting master degrees of freedom, *Journal of Mechanical Design*, 102 (1980) 412-416.
- [35] V. Shah, M. Raymund, Analytical selection of masters for the reduced eigenvalue problem, *International Journal for Numerical Methods in Engineering*, 18 (1982) 89-98.
- [36] N. Bouhaddi, R. Fillod, Substructuring using a linearized dynamic condensation method, *Computers & structures*, 45 (1992) 679-683.
- [37] N. Bouhaddi, R. Fillod, A method for selecting master DOF in dynamic substructuring using the Guyan condensation method, *Computers & Structures*, 45 (1992) 941-946.
- [38] L. Brillouin, *Wave propagation in periodic structures: electric filters and crystal lattices*, Courier Corporation, 2003.
- [39] A.S. Phani, J. Woodhouse, N. Fleck, Wave propagation in two-dimensional periodic lattices, *The Journal of the Acoustical Society of America*, 119 (2006) 1995-2005.
- [40] D. Mead, Wave propagation in continuous periodic structures: research contributions from Southampton, 1964–1995, *Journal of sound and vibration*, 190 (1996) 495-524.
- [41] D. Mead, Wave propagation and natural modes in periodic systems: I. Mono-coupled systems, *Journal of Sound and Vibration*, 40 (1975) 1-18.
- [42] D. Mead, Wave propagation and natural modes in periodic systems: II. Multi-coupled systems, with and without damping, *Journal of Sound and Vibration*, 40 (1975) 19-39.
- [43] D. Mead, A general theory of harmonic wave propagation in linear periodic systems with multiple coupling, *Journal of Sound and Vibration*, 27 (1973) 235-260.
- [44] D.J. Mead, The forced vibration of one-dimensional multi-coupled periodic structures: An application to finite element analysis, *Journal of Sound and Vibration*, 319 (2009) 282-304.
- [45] D.J. Mead, Free wave propagation in periodically supported, infinite beams, *Journal of Sound and Vibration*, 11 (1970) 181-197.
- [46] D. Mead, K. Pujara, Space-harmonic analysis of periodically supported beams: response to convected random loading, *Journal of sound and vibration*, 14 (1971) 525-541.

- [47] D. Mead, S. Parthan, Free wave propagation in two-dimensional periodic plates, *Journal of Sound and Vibration*, 64 (1979) 325-348.
- [48] D.J. Mead, Plates with regular stiffening in acoustic media: vibration and radiation, *The Journal of the Acoustical Society of America*, 88 (1990) 391-401.
- [49] B. Mace, The vibration of plates on two-dimensionally periodic point supports, *Journal of Sound and Vibration*, 192 (1996) 629-643.
- [50] B. Mace, Periodically stiffened fluid-loaded plates, I: Response to convected harmonic pressure and free wave propagation, *Journal of Sound and Vibration*, 73 (1980) 473-486.
- [51] B. Mace, Periodically stiffened fluid-loaded plates, II: response to line and point forces, *Journal of Sound and Vibration*, 73 (1980) 487-504.
- [52] J. Legault, N. Atalla, Numerical and experimental investigation of the effect of structural links on the sound transmission of a lightweight double panel structure, *Journal of sound and vibration*, 324 (2009) 712-732.
- [53] J. Wang, T. Lu, J. Woodhouse, R. Langley, J. Evans, Sound transmission through lightweight double-leaf partitions: theoretical modelling, *Journal of sound and vibration*, 286 (2005) 817-847.
- [54] J.-H. Lee, J. Kim, Analysis of sound transmission through periodically stiffened panels by space-harmonic expansion method, *Journal of Sound and Vibration*, 251 (2002) 349-366.
- [55] F. Xin, T. Lu, Transmission loss of orthogonally rib-stiffened double-panel structures with cavity absorption, *The Journal of the Acoustical Society of America*, 129 (2011) 1919-1934.
- [56] Y. Xiao, J. Wen, X. Wen, Sound transmission loss of metamaterial-based thin plates with multiple subwavelength arrays of attached resonators, *Journal of Sound and Vibration*, 331 (2012) 5408-5423.
- [57] Y. Xiao, J. Wen, X. Wen, Flexural wave band gaps in locally resonant thin plates with periodically attached spring-mass resonators, *Journal of Physics D: Applied Physics*, 45 (2012) 195401.
- [58] Y. Xiao, J. Wen, D. Yu, X. Wen, Flexural wave propagation in beams with periodically attached vibration absorbers: band-gap behavior and band formation mechanisms, *Journal of Sound and Vibration*, 332 (2013) 867-893.
- [59] S. Zouari, J. Brocail, J.-M. Génevaux, Flexural wave band gaps in metamaterial plates: A numerical and experimental study from infinite to finite models, *Journal of Sound and Vibration*, 435 (2018) 246-263.
- [60] J.-M. Berthelot, *Composite materials: mechanical behavior and structural analysis*, Springer Science & Business Media, 2012.
- [61] P. Smith Jr, Sound transmission through thin cylindrical shells, *The Journal of the Acoustical Society of America*, 29 (1957) 721-729.
- [62] L.R. Koval, On sound transmission into an orthotropic shell, *Journal of Sound and Vibration*, 63 (1979) 51-59.
- [63] L.R. Koval, Sound transmission into a laminated composite cylindrical shell, *Journal of Sound and Vibration*, 71 (1980) 523-530.
- [64] C. Bert, J. Baker, D. Egle, Free vibrations of multilayer anisotropic cylindrical shells, *Journal of Composite Materials*, 3 (1969) 480-499.
- [65] A. Blaise, C. Lesueur, Acoustic transmission through a 2-D orthotropic multi-layered infinite cylindrical shell, *Journal of Sound and Vibration*, 155 (1992) 95-109.
- [66] A. Blaise, C. Lesueur, M. Gotteland, M. Barbe, On sound transmission into an orthotropic infinite shell: Comparison with Koval's results and understanding of phenomena, *Journal of Sound and Vibration*, 150 (1991) 233-243.

- [67] A. Blaise, C. Lesueur, Acoustic transmission through a "3-D" orthotropic multi-layered infinite cylindrical shell, part I: Formulation of the problem, *Journal of sound and vibration*, 171 (1994) 651-664.
- [68] A. Blaise, C. Lesueur, Acoustic transmission through a "3-D" orthotropic multi-layered infinite cylindrical shell, part II: validation and numerical exploitation for large structures, *Journal of Sound and Vibration*, 171 (1994) 665-680.
- [69] J.-H. Lee, J. Kim, Sound transmission through periodically stiffened cylindrical shells, *Journal of Sound and Vibration*, 251 (2002) 431-456.
- [70] S. Ghinet, N. Atalla, H. Osman, Diffuse field transmission into infinite sandwich composite and laminate composite cylinders, *Journal of sound and vibration*, 289 (2006) 745-778.
- [71] S. Ghinet, N. Atalla, Vibro-acoustic behaviour of multi-layer orthotropic panels, *Canadian Acoustics*, 30 (2002) 72-73.
- [72] J.M. Whitney, Stress analysis of thick laminated composite and sandwich plates, *Journal of Composite Materials*, 6 (1972) 426-440.
- [73] S. Ahmad, B.M. Irons, O. Zienkiewicz, Analysis of thick and thin shell structures by curved finite elements, *International Journal for Numerical Methods in Engineering*, 2 (1970) 419-451.
- [74] R. Rolfes, K. Rohwer, Improved transverse shear stresses in composite finite elements based on first order shear deformation theory, *International Journal for Numerical Methods in Engineering*, 40 (1997) 51-60.
- [75] C. Fuller, Radiation of sound from an infinite cylindrical elastic shell excited by an internal monopole source, *Journal of sound and vibration*, 109 (1986) 259-275.
- [76] M. Kingan, P. Sureshkumar, Open rotor centrebody scattering, *Journal of Sound and Vibration*, 333 (2014) 418-433.
- [77] J.-D. Jung, S.-Y. Hong, J.-H. Song, H.-W. Kwon, Acoustic insulation performance of a honeycomb panel using a transfer matrix method, *Proceedings of the Institution of Mechanical Engineers, Part M: Journal of Engineering for the Maritime Environment*, (2017) 1475090217703467.
- [78] M. Munjal, Response of a multi-layered infinite plate to an oblique plane wave by means of transfer matrices, *Journal of Sound and Vibration*, 162 (1993) 333-343.
- [79] D. Rhazi, N. Atalla, Transfer matrix modeling of the vibroacoustic response of multi-materials structures under mechanical excitation, *Journal of sound and vibration*, 329 (2010) 2532-2546.
- [80] D. Rhazi, N. Atalla, A simple method to account for size effects in the transfer matrix method, *The journal of the acoustical society of america*, 127 (2010) EL30-EL36.
- [81] K. Mulholland, H. Parbrook, A. Cummings, The transmission loss of double panels, *Journal of Sound and Vibration*, 6 (1967) 324-334.
- [82] M. Villot, C. Guigou, L. Gagliardini, Predicting the acoustical radiation of finite size multi-layered structures by applying spatial windowing on infinite structures, *Journal of sound and vibration*, 245 (2001) 433-455.
- [83] W.H. Press, S.A. Teukolsky, W.T. Vetterling, B.P. Flannery, *Numerical recipes 3rd edition: The art of scientific computing*, Cambridge university press, 2007.
- [84] H.-J. Kang, J.-G. Ih, J.-S. Kim, H.-S. Kim, Prediction of sound transmission loss through multilayered panels by using Gaussian distribution of directional incident energy, *The Journal of the Acoustical Society of America*, 107 (2000) 1413-1420.
- [85] P. Bonfiglio, F. Pompili, R. Lioni, A reduced-order integral formulation to account for the finite size effect of isotropic square panels using the transfer matrix method, *The Journal of the Acoustical Society of America*, 139 (2016) 1773-1783.

- [86] T. Vigran, Predicting the sound reduction index of finite size specimen by a simplified spatial windowing technique, *Journal of sound and Vibration*, 325 (2009) 507-512.
- [87] A. Dijkmans, G. Vermeir, W. Lauriks, Sound transmission through finite lightweight multilayered structures with thin air layers, *The Journal of the Acoustical Society of America*, 128 (2010) 3513-3524.
- [88] J. Brunskog, The influence of finite cavities on the sound insulation of double-plate structures, *The Journal of the Acoustical Society of America*, 117 (2005) 3727-3739.
- [89] R. Buehrie, J. Robinson, F. Grosveld, Vibroacoustic model validation for a curved honeycomb composite panel, in: 19th AIAA Applied Aerodynamics Conference, 2001, pp. 1587.
- [90] C.I.J. Young, M.J. Crocker, Prediction of Transmission Loss by the Finite - Element Method, *The Journal of the Acoustical Society of America*, 54 (1973) 331-331.
- [91] P. Davidsson, J. Brunskog, P.-A. Wernberg, G. Sandberg, P. Hammer, Analysis of sound transmission loss of double-leaf walls in the low-frequency range using the finite element method, *Building Acoustics*, 11 (2004) 239-257.
- [92] Y.J. Kang, J.S. Bolton, A finite element model for sound transmission through foam - lined double - panel structures, *The Journal of the Acoustical Society of America*, 99 (1996) 2755-2765.
- [93] M. Petyt, Introduction to finite element vibration analysis, Cambridge university press, 2010.
- [94] A. Seybert, C. Cheng, Application of the boundary element method to acoustic cavity response and muffler analysis, *Journal of Vibration, Acoustics, Stress, and Reliability in Design*, 109 (1987) 15-21.
- [95] R. Zhou, M.J. Crocker, Boundary element analyses for sound transmission loss of panels, *The Journal of the Acoustical Society of America*, 127 (2010) 829-840.
- [96] A. Mejdji, N. Atalla, S. Ghinet, Wave spectral finite element model for the prediction of sound transmission loss and damping of sandwich panels, *Computers & Structures*, 158 (2015) 251-258.
- [97] R.H. Lyon, Theory and application of statistical energy analysis, Elsevier, 2014.
- [98] V. Cotoni, R. Langley, P. Shorter, A statistical energy analysis subsystem formulation using finite element and periodic structure theory, *Journal of Sound and Vibration*, 318 (2008) 1077-1108.
- [99] D. Chronopoulos, B. Troclet, M. Ichchou, J. Lainé, A unified approach for the broadband vibroacoustic response of composite shells, *Composites Part B: Engineering*, 43 (2012) 1837-1846.
- [100] L.D. Pope, On the transmission of sound through finite closed shells: statistical energy analysis, modal coupling, and nonresonant transmission, *The Journal of the Acoustical Society of America*, 50 (1971) 1004-1018.
- [101] R. Langley, On the modal density and energy flow characteristics of periodic structures, *Journal of Sound and Vibration*, 172 (1994) 491-511.
- [102] R. Langley, The modal density and mode count of thin cylinders and curved panels, *Journal of Sound and Vibration*, 169 (1994) 43-53.
- [103] R. Langley, Numerical evaluation of the acoustic radiation from planar structures with general baffle conditions using wavelets, *The Journal of the Acoustical Society of America*, 121 (2007) 766-777.
- [104] R.S. Langley, J.A. Cordioli, Hybrid deterministic-statistical analysis of vibro-acoustic systems with domain couplings on statistical components, *Journal of Sound and Vibration*, 321 (2009) 893-912.
- [105] P.J. Shorter, R. Langley, Vibro-acoustic analysis of complex systems, *Journal of Sound and Vibration*, 288 (2005) 669-699.

- [106] E. Reynders, R.S. Langley, A. Dijckmans, G. Vermeir, A hybrid finite element–statistical energy analysis approach to robust sound transmission modeling, *Journal of Sound and Vibration*, 333 (2014) 4621-4636.
- [107] C. Decraene, A. Dijckmans, E.B. Reynders, Fast mean and variance computation of the diffuse sound transmission through finite-sized thick and layered wall and floor systems, *Journal of Sound and Vibration*, 422 (2018) 131-145.
- [108] D.J. Mead, Vibration response and wave propagation in periodic structures, *Journal of Engineering for Industry*, 93 (1971) 783-792.
- [109] R.M. Orris, M. Petyt, A finite element study of harmonic wave propagation in periodic structures, *Journal of Sound and Vibration*, 33 (1974) 223-236.
- [110] R.M. Orris, M. Petyt, Random response of periodic structures by a finite element technique, *Journal of Sound and Vibration*, 43 (1975) 1-8.
- [111] B.R. Mace, D. Duhamel, M.J. Brennan, L. Hinke, Finite element prediction of wave motion in structural waveguides, *The Journal of the Acoustical Society of America*, 117 (2005) 2835-2843.
- [112] Y. Waki, B. Mace, M. Brennan, Numerical issues concerning the wave and finite element method for free and forced vibrations of waveguides, *Journal of Sound and Vibration*, 327 (2009) 92-108.
- [113] B.R. Mace, E. Manconi, Modelling wave propagation in two-dimensional structures using finite element analysis, *Journal of Sound and Vibration*, 318 (2008) 884-902.
- [114] E. Manconi, B. Mace, R. Garziera, Wave finite element analysis of fluid-filled pipes, (2009).
- [115] E. Manconi, B.R. Mace, Wave characterization of cylindrical and curved panels using a finite element method, *The Journal of the Acoustical Society of America*, 125 (2009) 154-163.
- [116] M. Maess, N. Wagner, L. Gaul, Dispersion curves of fluid filled elastic pipes by standard FE models and eigenpath analysis, *Journal of Sound and Vibration*, 296 (2006) 264-276.
- [117] B.R. Mace, E. Manconi, Wave motion and dispersion phenomena: Veering, locking and strong coupling effects, *The Journal of the Acoustical Society of America*, 131 (2012) 1015-1028.
- [118] Y. Waki, On the application of finite element analysis to wave motion in one-dimensional waveguides, in, University of Southampton, 2007.
- [119] S. Finnveden, Evaluation of modal density and group velocity by a finite element method, *Journal of Sound and Vibration*, 273 (2004) 51-75.
- [120] J.M. Renno, B.R. Mace, Calculation of reflection and transmission coefficients of joints using a hybrid finite element/wave and finite element approach, *Journal of Sound and Vibration*, 332 (2013) 2149-2164.
- [121] G. Mitrou, N. Ferguson, J. Renno, Wave transmission through two-dimensional structures by the hybrid FE/WFE approach, *Journal of Sound and Vibration*, 389 (2017) 484-501.
- [122] Y. Fan, M. Collet, M. Ichchou, L. Li, O. Bareille, Z. Dimitrijevic, Energy flow prediction in built-up structures through a hybrid finite element/wave and finite element approach, *Mechanical Systems and Signal Processing*, 66 (2016) 137-158.
- [123] Y. Waki, B. Mace, M.J. Brennan, On numerical issues for the wave/finite element method, (2006).
- [124] W. Zhong, F. Williams, On the direct solution of wave propagation for repetitive structures, *Journal of Sound and Vibration*, 181 (1995) 485-501.
- [125] M. Ichchou, S. Akrouf, J.-M. Mencik, Guided waves group and energy velocities via finite elements, *Journal of Sound and Vibration*, 305 (2007) 931-944.
- [126] D. Duhamel, B.R. Mace, M.J. Brennan, Finite element analysis of the vibrations of waveguides and periodic structures, *Journal of sound and vibration*, 294 (2006) 205-220.

- [127] Y. Waki, B. Mace, M. Brennan, Free and forced vibrations of a tyre using a wave/finite element approach, *Journal of Sound and Vibration*, 323 (2009) 737-756.
- [128] J.M. Renno, B.R. Mace, On the forced response of waveguides using the wave and finite element method, *Journal of Sound and Vibration*, 329 (2010) 5474-5488.
- [129] J.M. Renno, B.R. Mace, Calculating the forced response of two-dimensional homogeneous media using the wave and finite element method, *Journal of sound and vibration*, 330 (2011) 5913-5927.
- [130] J.M. Renno, B.R. Mace, Calculating the forced response of cylinders and cylindrical shells using the wave and finite element method, *Journal of Sound and Vibration*, 333 (2014) 5340-5355.
- [131] J.-M. Mencik, A model reduction strategy for computing the forced response of elastic waveguides using the wave finite element method, *Computer Methods in Applied Mechanics and Engineering*, 229 (2012) 68-86.
- [132] J.-M. Mencik, New advances in the forced response computation of periodic structures using the wave finite element (WFE) method, *Computational Mechanics*, 54 (2014) 789-801.
- [133] C. Zhou, J. Lainé, M. Ichchou, A. Zine, Wave finite element method based on reduced model for one-dimensional periodic structures, *International Journal of Applied Mechanics*, 7 (2015) 1550018.
- [134] C. Zhou, J. Lainé, M. Ichchou, A. Zine, Multi-scale modelling for two-dimensional periodic structures using a combined mode/wave based approach, *Computers & Structures*, 154 (2015) 145-162.
- [135] P.B. Silva, J.M. Mencik, J.R. de Franca Arruda, Wave finite element - based superelements for forced response analysis of coupled systems via dynamic substructuring, *International Journal for Numerical Methods in Engineering*, 107 (2016) 453-476.
- [136] C. Droz, Z. Zergoune, R. Boukadia, O. Bareille, M. Ichchou, Vibro-acoustic optimisation of sandwich panels using the wave/finite element method, *Composite Structures*, 156 (2016) 108-114.
- [137] F. Maurin, Bloch theorem with revised boundary conditions applied to glide and screw symmetric, quasi-one-dimensional structures, *Wave Motion*, 61 (2016) 20-39.
- [138] F. Maurin, C. Claeys, L. Van Belle, W. Desmet, Bloch theorem with revised boundary conditions applied to glide, screw and rotational symmetric structures, *Computer Methods in Applied Mechanics and Engineering*, 318 (2017) 497-513.
- [139] Y. Yang, B.R. Mace, M.J. Kingan, Prediction of sound transmission through, and radiation from, panels using a wave and finite element method, *The Journal of the Acoustical Society of America*, 141 (2017) 2452-2460.
- [140] Y. Yang, B.R. Mace, M.J. Kingan, Wave and finite element method for predicting sound transmission through finite multi-layered structures with fluid layers, *Computers & Structures*, 204 (2018) 20-30.
- [141] B.R. Mace, J. Renno, E. Manconi, Waves and finite elements, *Noise and Vibration: Emerging Methods*, (2012).